Microscopic study of various high-spin rotational states by the angular momentum projection method

嶋田, 充宏

https://doi.org/10.15017/1654644

出版情報：九州大学, 2015, 博士（理学）, 課程博士
バージョン：

Microscopic study of various high-spin rotational states by the angular momentum projection method

Mitsuhiro Shimada

Theoretical Nuclear Physics, Department of Physics

Graduate School of Science, Kyushu University

744, Motooka, Nishi-ku, Fukuoka 819-0395, Japan

Abstract

Nuclei have two excitation modes of the motion: the collective motion and the single-particle motion. The competition of these two modes has a large influence on the nuclear properties. Most nuclei have deformed shape, and then the rotational motion occurs to restore the rotational invariance broken by the nuclear deformation. The rotational motion is one of the basic collective motions, and its microscopic understanding is important. The angular momentum projection method is a method to microscopically describe the nuclear rotational motion. The symmetry in nuclei can be generally broken in the mean-field theory (Hartree-Fock-Bogoliubov theory). In the projection method, the rotational motion appears by restoring the broken rotational symmetry. Recent development of accelerators and detectors enables us to explore the high-spin states, and much attention has been paid to them. High-spin states are appropriate for investigating the competition of two modes of the collective and the single-particle motions. Various interesting rotational motions at the high-spin states are predicted by the macroscopic model, and their microscopic understanding is necessary. In this thesis, we study various rotational motions in nuclei from the microscopic viewpoint by the angular momentum projection method.

First, we apply the angular momentum projection method to the low-spin states of the Mg isotopes before studying the high-spin states. The experimental data for the unstable nuclei are gradually accumulating with the advances of the accelerator, and the properties of nuclei in the so-called "island of inversion" have received considerable attention. Nuclei in this region have characteristic features such as the change of the magic numbers, which are not seen in stable nuclei. Some of the Mg isotopes belonging to this region, and recently the experimental data such as the excitation energies and the electromagnetic transition probabilities are observed close to the neutron drip line. In the mean-field calculation, the nucleus ^{32}Mg in the island of inversion is predicted to have the spherical ground state although the experimental data suggest the deformed shape. However, the deformed state for ^{32}Mg is obtained by considering the angular momentum projection. Thus, the angular momentum projection plays an important role. Since the energy difference between the prolate and oblate deformations for the nuclei in this region is not so large, it may be necessary to perform the configuration mixing with respect to the deformation parameters. Therefore, for the low-spin state of Mg isotopes, we investigate the excitation energies, the electromagnetic transition probabilities and the root mean square radii by the angular momentum projection

method with the quadrupole configuration mixing employing the Gogny D1S interaction. Our calculation shows a nice agreement with the experimental data. It is found that the angular momentum projection method is a useful and powerful tool for the microscopic study of the rotational states.

Next, we propose a method to reliably calculate the high-spin states by the angular momentum projection technique. The so-called cranking model has been used for describing the rotational states in the mean-field framework. In the cranking model, the effect of the collective rotation on the wave function is included by considering the uniform rotation with the rotational frequency $\omega_{\rm rot}$. Therefore, the cranked state is used for the intrinsic state of the projection calculation. All the states belonging to a rotational band are obtained by the projection from one cranked state, which produce a lot of resultant spectra depending the frequency $\omega_{\rm rot}$. As a result, it should be considered how to compromise between the angular momentum projection method and the cranking model. In addition, the moment of inertia calculated by the projection from one cranked state is constant (or decrease) as a function of spin, which is inconsistent with the realistic spin-dependence. As a method to solve these two problems, we propose "angular momentum projected multi-cranked configuration mixing". In this method, the rotational states are described by superposing several states obtained by the projection from the cranked states with different frequencies. In this thesis, we apply this method to the ground-state rotational bands of nuclei in the rare-earth region, the superdeformed rotational band and the s-band, and it is found that this method is very useful for the reliable description of the high-spin states.

Finally, we apply the angular momentum projection method to the high-spin state of triaxially deformed nuclei. In this thesis, we investigate the wobbling band and the chiral doublet band. The wobbling rotation is based on the vibrational motion of the rotational axis on the top of the rotation around a principal axis, which produces a phonon-like multiple band structure. For the odd nucleus ^{163}Lu, this phonon-like multiple band structure, which are connected by the strong out-of-band $E2$ transition, appears in our fully microscopic calculation, and the existence of the wobbling rotation are confirmed microscopically. The relation between the triaxial deformation and the wobbling rotation is also investigated. In the odd-odd nuclei with a high-j particle and a high-j hole, the three angular-momentum vectors, those of the core, the high-j particle and the high-j hole, tend to align along the three mutually perpendicular directions. These three angular-momentum vectors give rise to a right- and left-handed chiral geometries, which generate a degenerate pair of bands. This degenerate pair of bands appears in the projection calculation, and the characteristic pattern of $M1$ transition probabilities for the chiral doublet band is also confirmed in our calculation. The angular momentum projection method is the useful and powerful tool for the microscopic study of the high-spin states.

Contents

List of Figures

List of Tables

Chapter 1

Introduction

1.1 Deformation and rotation

The nucleus is a quantum many-body system that consists of nucleons. A nucleon is either proton or neutron, and nuclei are classified by the number of protons and neutrons. The nucleons interact with each other through the nuclear force (and the Coulomb force) and are bound within nuclei. The maximum number of nucleon in nuclei existing in nature is about 300. Therefore the nucleus is a finite quantum system.

Nuclei have two excitation modes: the single-particle and the collective modes. Nuclear properties are largely explained by the independent-particle model like electrons in the atom. Each nucleon in nuclei moves independently in the average potential that is formed by the two-body forces between nucleons. In this picture, the nuclear magic numbers (8, 20, 28, 50, 82 and 126) are explained. Nuclei with these specific numbers of neutrons or protons become more stable. On the other hand, some part of their properties is explained by the liquid drop model, in which nucleons move collectively, e.g., the vibrational and rotational motions. The competition of these two modes of motion affects the properties of nuclei, and it is important to consider these modes of motion uniformly. Since the nuclear collective motions are the coherent motion of nucleons, they should be understood microscopically.

Nuclei exhibit a lot of collective motions, and they have been studied both theoretically and experimentally. In particular, the rotational motion, which is one of the basic collective motions, is one of the most interesting topics in nuclear physics. In the framework of mean-field (Hartree-Fock-Bogoliubov, HFB) theory, the symmetries in nuclei can be broken spontaneously due to the nonlinearity of the equation. Especially, in the case where the rotational symmetry is broken, the deformed state is more favorable energetically than the spherical state, and nuclei can deform spontaneously. While most of nuclei with magic numbers have the spherical ground states, nuclei with nucleon number far from the magic number have quadrupole deformed shapes. As a result, the rotational motion occurs to restore the rotational symmetry broken by the deformation. The existence of this rotational motion is confirmed experimentally by the appearance of the characteristic band structure of the energy spectrum, i.e., the

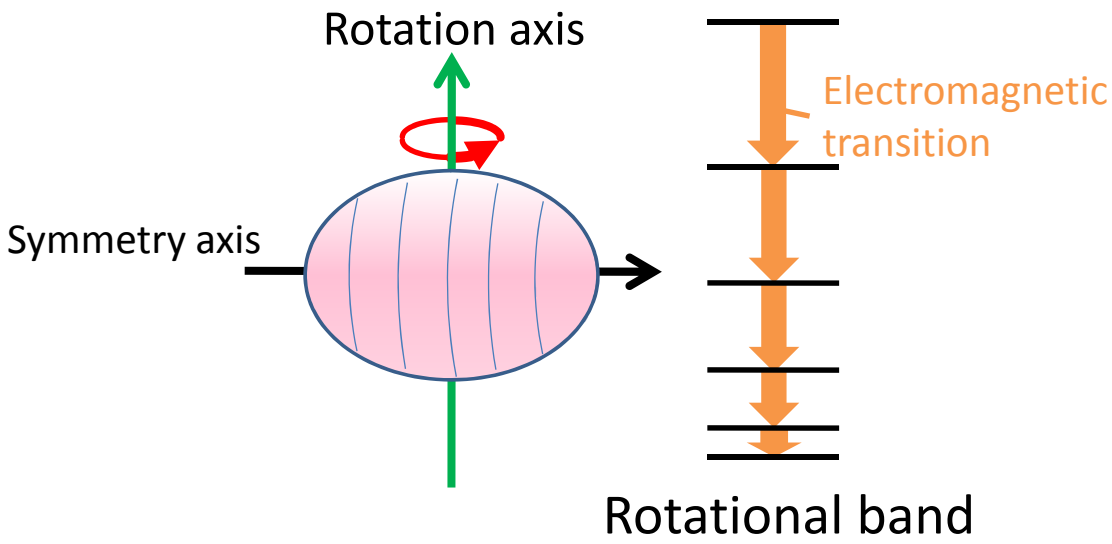

Figure 1.1: Schematic picture of nuclear rotational motion. The nuclear collective rotational motion occurs to restore the rotational symmetry.

rotational band. In the case of the axially symmetric deformation, the nucleus rotates around one vertical axis to the symmetric axis. In fact a nice rotational spectrum with $I^\pi = 0^+, 2^+, 4^+, 6^+, \cdots$ is observed for the ground state band of axially symmetric even-even nuclei. The typical picture of nuclear rotational motion is shown in Fig. 1.1.

1.2 Projection method

Rotational motions have been studied by using the macroscopic models. There are many adjustable parameters in such models. However, nuclear rotational motion is a coherent motion of constituent particles, and to comprehend the nuclear rotational states their microscopic understanding is necessary. Recently an efficient method to perform the angular momentum projection is developed [1], which is a fully microscopic approach to the nuclear rotational motion starting from the symmetry broken mean-field state. In this approach, the rotational symmetry is restored by superposing many rotated states. Moreover, very recently it became possible to perform the angular momentum projection employing the Gogny effective interaction [2]. With this approach, we study microscopically the various nuclear rotational motions.

In the projection calculation, the rotational states are obtained from the symmetry broken intrinsic state, which is calculated by diagonalizing the mean-field Hamiltonian. In the standard HFB framework, we can obtain only the energy-minimum with respect to all the permitted freedoms like the deformation parameters. In order to understand the deformation properties, it is necessary to see the energy as a function of the deformation parameters, which is calculated by constraining the deformation parameters in the HFB calculation. Then, it is important to consider the effects of the collective

rotation on the mean-field parameters like the deformations and the pairing gaps. In the cranking model, these effects can be taken into account by considering the Hamiltonian transformed into the uniformly rotating frame with cranking frequency $\omega_{\rm rot}$. Thus, the cranked HFB states are used for the intrinsic states of the projection calculation. Since the cranking term breaks the time reversal symmetry, we can include the time-odd components into the wave function by the cranking model.

It is important to obtain the correct deformation for describing the rotational motion. The angular momentum projection plays an important role for determining the deformation parameter. The energy gain associated with restoration of the rotational symmetry increases as a function of the deformation parameter, which can cause the appearance (or large change) of deformation. In fact, for the nucleus ^{32}Mg, while in the mean-field calculation the spherical ground state is predicted, the deformed ground state, which is consistent with the experimental suggestions [3, 4, 5, 6], is found by performing the angular momentum projection. The correct deformations for the Mg isotopes are obtained by the angular momentum projection method. For nuclear rotational states, not only the correlation of the symmetry restoration but also the effect of the fluctuation of deformation may play a role. It is important to consider the effect of the configuration mixing of deformed states in these cases. With this in mind, we performed angular momentum projection calculations with the configuration mixing with respect to the quadrupole deformation for low-spin states of Mg isotopes.

1.3 High-spin state

Recent developments of the accelerators and the detectors enable us to explore various states of nuclei under extreme conditions such as the high-spin states, in which nucleus has large angular momentum, and nuclei around drip line, in which the difference between the proton and the neutron numbers is large. In particular, the study of the high-spin states is one of the interesting topics in nuclear physics. As mentioned in the previous section, the competition of the collective rotational motion and the independent-particle motion affect the nuclear properties, and the study of high-spin states is suitable to investigate this competition. High-spin states are relatively easily generated by bringing the large angular momentum using the heavy-ion nuclear reaction, and identified by analyzing a lot of gamma rays emitted through its reaction. At high-spin states, a large deformation is favored and nuclei can have much more largely deformed shape than in ground states. For example, a number of nuclei at high spin states have the superdeformed shape with approximately 2:1 ratio of the long and short axes [7, 8]. Furthermore, the existence of the hyperdeformed nuclei is predicted, which have a prolate shape with 3:1 ratio of axes. At high-spin states, the collective rotation has a large influence on the single-particle states. The single-particle angular momentum vectors tend to align along the rotation axis. This effect causes the alignment of the lowest two quasineutrons at high-spin. In fact, the crossings between the ground-state band (g-band) and Stockholm band (s-band), where the alignment of the

lowest two quasineutrons occurs, are observed for nuclei in the rare-earth region. At high-spin states, there are many interesting rotational bands, and it has been intensively studied both experimentally and theoretically.

Although the angular momentum projection method is a standard microscopic approach to the nuclear rotational motion, the simple projection from only one cranked state is not satisfactory for the description of the high-spin states. In Chap. 4, we propose "angular momentum projected multi-cranked configuration mixing", which is a method to reliably calculate the high-spin states by the angular momentum projection technique. In this method, rotational states are obtained by superposing the multiple cranked states with different cranking frequencies. A lot of ground-state rotational bands, the s-band and the superdeformed band are studied by the method.

1.4 Triaxial deformation

Although the well-known deformation in nuclei is the axially symmetric ellipsoidal deformation, the possible existence of triaxial deformation is suggested theoretically and experimentally. Since the collective rotational motion occurs to restore the rotational invariance, in the case of axially symmetric deformed nuclei, the rotational motion around the symmetry axis does not occur, and only the rotational states around one axis perpendicular to the symmetry axis are generated. On the other hand, in the case of triaxial deformed nuclei the three-dimensional collective rotations are possible, which provide us various interesting rotational bands.

At high-spin states of the triaxially deformed nuclei, there are many interesting rotational bands such as the wobbling band and the chiral doublet band. The wobbling rotational band was first predicted by the triaxial rotor model [9], and is composed of the phonon-like multiple rotational sequences. The wobbling band was first discovered in the odd nucleus ^{163}Lu [10]. The chiral doublet band is predicted to appear in the triaxially deformed odd-odd nuclei with a high-j particle and a high-j hole, and a degenerate pair of bands appears like in the case of the parity doublet. The chiral doublet bands are investigated and identified in the $A \sim 100$ and 130 regions [11, 12, 13]. The identification of these rotational bands is regarded as the proof of the triaxial deformation, and the electromagnetic transition probabilities as well as the spectra are a key for their identification.

Since these rotational bands are studied mainly by the macroscopic model, which has many adjustable parameters, their microscopic understanding is necessary. Therefore, we study the wobbling band for the odd nucleus ^{163}Lu and the chiral doublet band for the odd-odd nuclei ^{128}Cs and ^{104}Rh by the angular momentum projection method in Chap. 5.

1.5 Purpose of the present thesis

A lot of studies of high-spin states are based on the macroscopic models. At high-spin states, various rotational motions are predicted by the macroscopic models, but they have many adjustable parameters. It is necessary to understand these rotational motions microscopically. In this thesis, we investigate various high-spin rotational bands microscopically by the angular momentum projection method.

In Chap. 2, theoretical framework of the Hartree-Fock-Bogoliubov theory, the angular momentum projection method and the generator coordinate method are briefly explained. In Chap. 3, before studying the high-spin rotational bands, we apply the angular momentum projection method to the low-spin states of Mg isotopes. For these isotopes, since it is important to consider the effects of the fluctuation of the quadrupole deformation, we apply the angular momentum projection method with the quadrupole configuration mixing. The effect of the rotational symmetry restoration on the deformation parameters is discussed. We investigate the effect of the quadrupole configuration mixing and of the time-odd components induced by the cranking model on excitation energies, $B(E2)$ transition probabilities and nuclear radii. It is found that the projection calculation is useful for the microscopic study of the nuclear rotational states.

In Chap. 4, we propose the "angular momentum projected multi-cranked configuration mixing" as a method to calculate high-spin states more reliably. By applying this method to the ground state band of ^{164}Er, the ground state band of ^{40}Mg and the superdeformed band of ^{152}Dy, it is found that the accurate rotational bands can be efficiently calculated by this method. We systematically investigate the ground state bands of nuclei in the rare-earth region and also apply to the s-band of ^{164}Er. This chapter is based on the following paper:

- **"Angular momentum projected multi-cranked configuration mixing for reliable calculation of high-spin rotational bands"**
  M. Shimada, S. Tagami, and Y. R. Shimizu,
  Prog. Theor. Exp. Phys., **2015**, 063D02 (2015).

In Chap. 5, we study the wobbling band and chiral doublet band by the projection calculation. As for the wobbling band, results for odd nucleus ^{163}Lu are presented, and its dependence for the sign of the triaxial deformation parameter γ is investigated. As for the chiral doublet band, the energy spectra for the odd-odd nuclei ^{128}Cs and ^{104}Rh are presented. The characteristic pattern of $B(M1)$ transition probabilities are also discussed. Finally, Chap. 6 is devoted to the summary.

Chapter 2

Theoretical framework

In this chapter, we explain the Hartree-Fock-Bogoliubov (HFB) approximation, the angular momentum projection method and the generator coordinate method briefly. (in detail, see Ref. [14])

2.1 HFB theory

2.1.1 Bogoliubov transformation

The HFB theory is a method to obtain the many-body eigenstate in the mean-field approximation. With the Bogoliubov transformation the quasiparticle creation and annihilation operators $(\hat{\beta}_k^\dagger, \hat{\beta}_k)$ are defined as

$$\beta_k^\dagger = \sum_l \left[U_{lk}\hat{c}_l^\dagger + V_{lk}\hat{c}_l \right], \quad \beta_k = \sum_l \left[V_{lk}^*\hat{c}_l^\dagger + U_{lk}^*\hat{c}_l \right], \tag{2.1}$$

where $(\hat{c}_l^\dagger, \hat{c}_l)$ are the single-particle creation and annihilation operators. We introduce the matrix $\mathcal{W}$,

$$\mathcal{W} \equiv \begin{pmatrix} U & V^* \\ V & U^* \end{pmatrix}. \tag{2.2}$$

With this matrix, the quasiparticle operators $(\hat{\beta}^\dagger, \hat{\beta})$ are represented as

$$\begin{pmatrix} \hat{\beta}^\dagger \\ \hat{\beta} \end{pmatrix} = \begin{pmatrix} U^\dagger & V^\dagger \\ V^T & U^T \end{pmatrix} \begin{pmatrix} \hat{c}^\dagger \\ \hat{c} \end{pmatrix} = \mathcal{W}^\dagger \begin{pmatrix} \hat{c}^\dagger \\ \hat{c} \end{pmatrix}. \tag{2.3}$$

Since the quasiparticle is fermion, the relations between the coefficients U and V,

$$\mathcal{W}\mathcal{W}^\dagger = \mathcal{W}^\dagger\mathcal{W} = 1, \tag{2.4}$$

hold. The transformation from the quasiparticle operator to the single-particle operator is given by

$$\begin{pmatrix} \hat{c}^\dagger \\ \hat{c} \end{pmatrix} = \mathcal{W} \begin{pmatrix} \hat{\beta}^\dagger \\ \hat{\beta} \end{pmatrix}. \tag{2.5}$$

The HFB ground state of the many-body system, $|\Phi\rangle$, is the vacuum with respect to quasiparticles:

$$\hat{\beta}_k |\Phi\rangle = 0. \tag{2.6}$$

For this wave function $|\Phi\rangle$, the density matrix ρ and the pairing tensor κ are defined as

$$\rho_{ll'} \equiv \frac{\langle\Phi| \hat{c}^\dagger_{l'}\hat{c}_l |\Phi\rangle}{\langle\Phi|\Phi\rangle}, \quad \kappa_{ll'} \equiv \frac{\langle\Phi| \hat{c}_{l'}\hat{c}_l |\Phi\rangle}{\langle\Phi|\Phi\rangle}. \tag{2.7}$$

With the equations (2.4) and (2.5), the matrices ρ and κ are given by

$$\rho = V^*V^T = 1 - UU^\dagger, \quad \kappa = V^*U^T = -UV^\dagger. \tag{2.8}$$

We introduce the generalized density matrix,

$$\mathcal{R} \equiv \begin{pmatrix} \rho & \kappa \\ -\kappa^* & 1-\rho^* \end{pmatrix}. \tag{2.9}$$

The hermitian matrix $\mathcal{R}$ satisfies the relations,

$$\mathcal{R} = \begin{pmatrix} V^*V^T & V^*U^T \\ U^*V^T & U^*U^T \end{pmatrix} = \mathcal{W} \begin{pmatrix} 0 & 0 \\ 0 & 1 \end{pmatrix} \mathcal{W}^\dagger, \tag{2.10}$$

$$\mathcal{R}^2 = \mathcal{R}. \tag{2.11}$$

2.1.2 HFB equation

The density matrix ρ and the pairing tensor κ are determined to minimize the ground state energy from the variational principle. The many-body Hamiltonian has the form

$$\hat{H} = \sum_{l_1 l_2} t_{l_1 l_2} \hat{c}^\dagger_{l_1} \hat{c}_{l_2} + \frac{1}{4} \sum_{l_1 l_2 l_3 l_4} \bar{v}_{l_1 l_2 l_3 l_4} \hat{c}^\dagger_{l_1} \hat{c}^\dagger_{l_2} \hat{c}_{l_4} \hat{c}_{l_3}, \tag{2.12}$$

$$\bar{v}_{l_1 l_2 l_3 l_4} = -\bar{v}_{l_2 l_1 l_3 l_4} = -\bar{v}_{l_1 l_2 l_4 l_3} = \bar{v}^*_{l_3 l_4 l_1 l_2}, \tag{2.13}$$

where $t_{l_1 l_2}$ is the one-body kinetic energy operator and $\bar{v}_{l_1 l_2 l_3 l_4}$ is the antisymmetric two-body interaction matrix elements. Because in the HFB framework the particle number is not conserved, the variation is done with conserving it on average, i.e. the expectation value of the operator, $\hat{H}' = \hat{H} - \lambda_N \hat{N}$, is minimized, where $\hat{N}$ is the particle number operator. According to the Thouless theorem, if the arbitrary HFB-type wave function $|\Phi'\rangle$ is not orthogonal to $|\Phi\rangle$, it is represented by

$$|\Phi'\rangle = \exp\left(\sum_{kk'} Z_{kk'} \beta^\dagger_k \beta^\dagger_{k'} \right) |\Phi\rangle. \tag{2.14}$$

With the variation with respect to the coefficient $Z^*_{kk'}$ the minimum state satisfies the condition,

$$\left[\frac{\partial}{\partial Z^*_{kk'}} \frac{\langle\Phi'|\hat{H}'|\Phi'\rangle}{\langle\Phi'|\Phi'\rangle} \right]_{Z=0} = H^{(20)}_{kk'} = 0. \tag{2.15}$$

where

$$H^{(11)}_{kk'} \equiv \langle\Phi|\{[\hat{\beta}_k, \hat{H}], \hat{\beta}^\dagger_{k'}\}|\Phi\rangle, H^{(20)}_{kk'} \equiv \langle\Phi|\{[\hat{\beta}_k, \hat{H}], \hat{\beta}_{k'}\}|\Phi\rangle. \tag{2.16}$$

We obtain

$$\begin{pmatrix} H^{(11)} & H^{(20)} \\ -H^{(20)*} & -H^{(11)*} \end{pmatrix} = \begin{pmatrix} U & V^* \\ V & U^* \end{pmatrix}^\dagger \begin{pmatrix} h & \Delta \\ -\Delta^* & -h^* \end{pmatrix} \begin{pmatrix} U & V^* \\ V & U^* \end{pmatrix}, \tag{2.17}$$

where $h = t + \Gamma$ is the mean-field Hamiltonian and Δ is the pairing potential,

$$\Gamma_{kl} \equiv \sum_{k'l'} \bar{v}_{kk'll'}\rho_{l'k'}, \ \Delta_{kl} \equiv \frac{1}{2}\sum_{k'l'} \bar{v}_{klk'l'}\kappa_{k'l'}. \tag{2.18}$$

By using the condition $H^{(20)} = 0$, we can diagonalize $H^{(11)}$ in Eq.(2.16) by the equation

$$\begin{pmatrix} U & V^* \\ V & U^* \end{pmatrix}^\dagger \begin{pmatrix} h & \Delta \\ -\Delta^* & -h^* \end{pmatrix} \begin{pmatrix} U & V^* \\ V & U^* \end{pmatrix} = \begin{pmatrix} \ddots & & & & & \\ & E_k & & & 0 & \\ & & \ddots & & & \\ & & & \ddots & & \\ & 0 & & & -E_k & \\ & & & & & \ddots \end{pmatrix}. \tag{2.19}$$

As a result, the eigenvalue equation,

$$\begin{pmatrix} h & \Delta \\ -\Delta^* & -h^* \end{pmatrix} \begin{pmatrix} U_k \\ V_k \end{pmatrix} = E_k \begin{pmatrix} U_k \\ V_k \end{pmatrix}, \tag{2.20}$$

is obtained. This eigenvalue equation is called a HFB equation. In this equation, the mean-field Hamiltonian h and pairing potential Δ are given from the density matrices ρ and pairing tensor κ, and the matrices ρ and κ are given from coefficients U and V, which are obtained by solving the HFB equation. Therefore, the HFB equation is non-linear selfconsistent equation, which can be solved by the iterative procedure.

In this thesis, the standard method of the harmonic-oscillator basis expansion is used for the HFB as well as the projection calculations. As for the oscillator basis expansion the frequency $\hbar\omega = 41/A^{1/3}$ MeV is employed and all the basis states with the oscillator quantum numbers (n_x, n_y, n_z) satisfying $n_x+n_y+n_z \leq N^{\max}_{\rm osc}$ are retained.

Using the Wick theorem, the energy, $E = \langle\Phi|\hat{H}|\Phi\rangle / \langle\Phi|\Phi\rangle$, is given by

$$E = E_{\rm kin} + E_{\rm int}, \tag{2.21}$$

$$E_{\rm kin} = \sum_{l_1 l_2} t_{l_1 l_2}\rho_{l_2 l_1} = {\rm Tr}\left[t\rho\right], \tag{2.22}$$

$$\begin{aligned} E_{\rm int} &= \frac{1}{2}\sum_{l_1 l_2 l_3 l_4} \bar{v}_{l_1 l_2 l_3 l_4}\rho_{l_3 l_1}\rho_{l_4 l_2} + \frac{1}{4}\sum_{l_1 l_2 l_3 l_4} \bar{v}_{l_1 l_2 l_3 l_4}\kappa^*_{l_1 l_2}\kappa_{l_3 l_4} \\ &= {\rm Tr}\left[\frac{1}{2}\rho\Gamma + \frac{1}{2}\kappa^\dagger\Delta\right], \end{aligned} \tag{2.23}$$

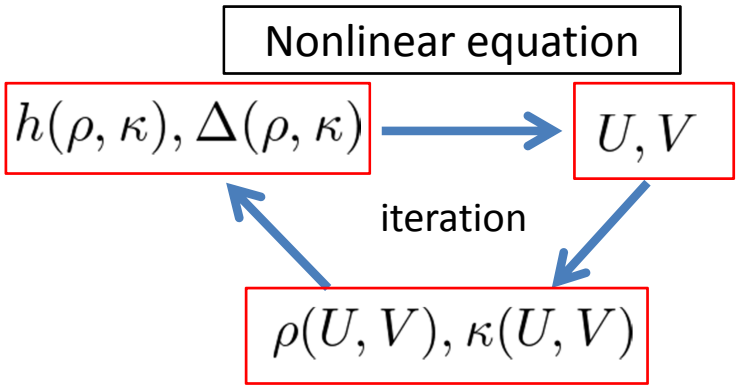

Figure 2.1: Schematic picture of the nonlinearity of the HFB equation. The matrices h and Δ, which is necessary to solve the HFB equation, are dependent on the solutions of its equation, U and V.

where the terms $E_{\rm kin}$ and $E_{\rm int}$ represent the kinetic and interaction energies, respectively. When the density-dependent term is included in the two-body interaction v such as the Skyrme force and Gogny force, the matrices h and Δ are represented as

$$\begin{aligned} h_{l_1 l_2} &\equiv \frac{\delta}{\delta \rho_{l_2 l_1}} \left[\frac{\langle \Phi | \hat{H}' | \Phi \rangle}{\langle \Phi | \Phi \rangle} \right] \\ &= t_{l_1 l_2} - \lambda N_{l_1 l_2} + \sum_{k'l'} \bar{v}_{l_1 l_3 l_2 l_4} \rho_{l_4 l_2} + \frac{1}{2} \sum_{l_3 l_4 l_5 l_6} \frac{\delta \bar{v}_{l_3 l_4 l_5 l_6}}{\delta \rho_{l_2 l_1}} \rho_{l_5 l_3} \rho_{l_6 l_4} \\ &\equiv t_{l_1 l_2} - \lambda N_{l_1 l_2} + \sum_{k'l'} \bar{v}_{l_1 l_3 l_2 l_4} \rho_{l_4 l_2} + h^{(\rm rea)}_{l_1 l_2}, \end{aligned} \tag{2.24}$$

$$\Delta_{l_1 l_2} \equiv 2 \frac{\delta}{\delta \kappa^*_{l_1 l_2}} \left[\frac{\langle \Phi | \hat{H}' | \Phi \rangle}{\langle \Phi | \Phi \rangle} \right] = \frac{1}{2} \sum_{l_3 l_4} \bar{v}_{l_1 l_2 l_3 l_4} \kappa_{l_3 l_4}, \tag{2.25}$$

where $N_{l_1 l_2}$ is the norm matrix, which is $N_{l_1 l_2} = \delta_{l_1 l_2}$ for the harmonic oscillator basis. The correction term $h^{(\rm rea)}$, which is called the rearrangement term, is necessary due to the density-dependence of the interaction.

2.1.3 Constraned-HFB (CHFB) method

In the standard HFB framework, we can obtain only the minimum of the HFB energy with respect to the all permitted degrees of freedom. The constrained Hartree-Fock-Bogoliubov (CHFB) method is used to obtain the potential energy surface (PES) corresponding to the HFB energies as a function of the quadrupole moment. The PES offers a valuable starting point to understand nuclear deformation properties. To satisfy constraints, two approaches are well known, which are the linear constraint method and quadratic constraint method.

In the constrained HFB framework, under the constraint condition for the one-body operator $\hat{Q}$,

$$q = \langle \Phi | \hat{Q} | \Phi \rangle \equiv \langle \hat{Q} \rangle, \tag{2.26}$$

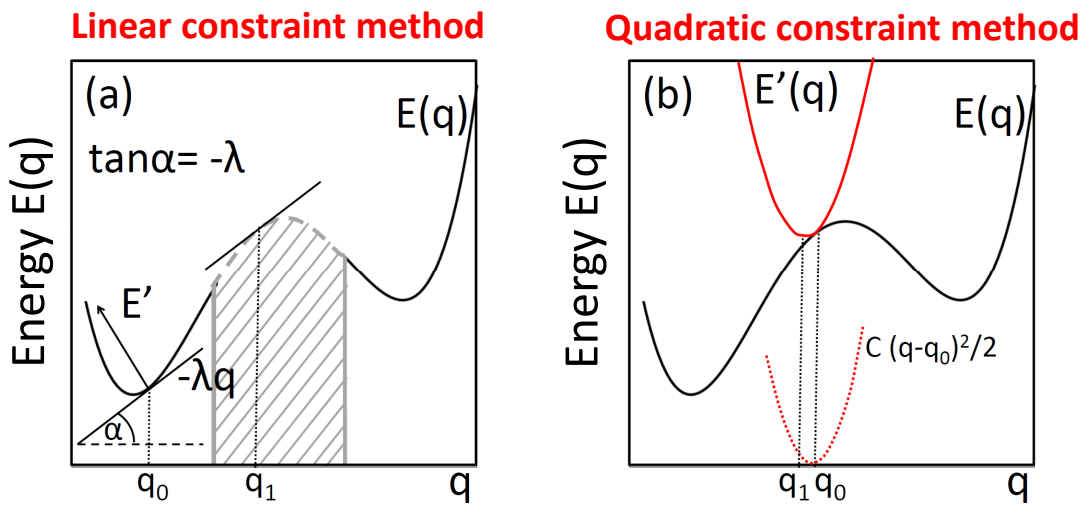

Figure 2.2: Geometric interpretation of constrained HFB with (a) the liner constraint method and (b) the quadratic constraint method. Within the linear constraint method the shaded region in the panel (a) cannot be obtained.

the energy is minimized according to the variational principle. If we want to constrain the deformation parameter, the operator $\hat{Q}$ is chosen to be the multipole-moment operator,

$$\hat{Q}_{\lambda\mu} = r^{\lambda} Y_{\lambda\mu}(\Omega), \tag{2.27}$$

where the function $Y_{\lambda\mu}(\Omega)$ is the spherical harmonics. In the linear constraint method, the function

$$E' = \langle \hat{H}' \rangle = \langle \Phi(q) | (\hat{H} - \lambda \hat{Q}) | \Phi(q) \rangle \tag{2.28}$$

is minimized instead of the energy $E = \langle \hat{H} \rangle$. The Lagrange multiplier λ is determined from the condition (2.26). In the HFB framework, the particle number is not conserved and it is necessary to constrain its expectation value. The minimization of the expectation value of the Hamiltonian $\hat{H}' = \hat{H} - \lambda_N \hat{N}$ corresponds to the linear constrain method. The Lagrange multiplier λ is given by

$$\lambda = \frac{dE}{dq}. \tag{2.29}$$

In the case of the particle number constrained calculation, the Lagrange multiplier λ_N corresponds the Fermi energy. Fig. 2.2(a) shows the geometric interpretation of the linear constraint method. The constrained point q_0 corresponds to the minimum point in the new coordinate system rotated by the angle α. Within this method, when there are two solutions that have the same multiplier λ, the higher energy solution is not stable from the variational principle. Therefore, the linear constraint method cannot be applied for the regions of $E(q)$ that are concave, which is the shaded region in Fig2.2(a).

The standard method to solve this problem is the quadratic constraint method. In this method,

$$E' = \langle \hat{H}' \rangle = \langle \Phi(q) | \hat{H} | \Phi(q) \rangle + \frac{1}{2} C (\langle \Phi(q) | \hat{Q} | \Phi(q) \rangle - q_0)^2, \tag{2.30}$$

is minimized instead of the energy $E = \langle \hat{H} \rangle$. The solution around $q = q_0$ is obtained by properly choosing the coefficient $C > |d^2E/dq^2|$. When the value of C is too small, the solution has the constraint value quite far away from the requested value q_0 and when the value of C is too large, the constrained calculation often fails to converge. Therefore, in this method it is important to determine the proper coefficient C. The geometric interpretation of the quadratic constraint method is shown in Fig. 2.2(b). The constrained point q_1 corresponds to the minimum point of the function E', plotted with the red line in Fig2.2(b). Recently, the so-called augmented Lagrangian method (ALM) has been developed for the constraint-HFB calculation [15]. The ALM is considered as a combination of the linear constrained method and the quadratic constrained method, which yields the requested constrained value accurately in all region. In this method, the function

$$E' = \langle \hat{H}' \rangle = \langle \Phi(q)|\hat{H}|\Phi(q)\rangle + \lambda(q - q_0) + \frac{1}{2}C(\langle \Phi(q)|\hat{Q}|\Phi(q)\rangle - q_0)^2, \tag{2.31}$$

is minimized, where the Lagrange multiplier is determined iteratively by

$$\lambda^{k+1} = \lambda^k + \frac{1}{2}C(q - q_0). \tag{2.32}$$

The iterative procedure starts from the initial value $\lambda^0 = 0$, and the Lagrange multiplier λ is updated in the minimization process. We use this ALM if necessary.

2.1.4 Cranked HFB method

The cranking model is often used for the description of the rotational states within the mean-field framework. The Hamiltonian transformed into the uniformly rotating frame (the so-called Routhian),

$$\hat{H}' = \hat{H} - \omega_{\rm rot}\hat{J}_y, \tag{2.33}$$

is considered instead of the original Hamiltonian $\hat{H}$. Here the quantity $\omega_{\rm rot}$ is the rotational (or cranking) frequency and $\hat{J}_y$ is the angular momentum operator around the rotation-axis (here chosen to be the y-axis). The effects of the Coriolis and centrifugal forces are included by the term $-\omega_{\rm rot}\hat{J}_y$, the so-called cranking term, which breaks the time reversal symmetry of the wave function. It was first introduced by Inglis for calculating the moment of inertia of the ground-state rotational band [16] by treating the cranking term $-\omega_{\rm rot}\hat{J}_y$ as a lowest order perturbation, i.e., at the $\omega_{\rm rot} \to 0$ limit. It was extended to the finite rotational frequency to understand various phenomena at high-spin states as the selfconsistent cranking model [17] or the cranked shell model [18], see e.g. Refs. [19, 20, 21]. The HFB approximation combined with the cranking model is called the cranked HFB approximation. The cranked HFB calculation is one of the constrained HFB calculations with the linear constraint method employing the angular momentum operator, where the Lagrange multiplier is the rotational frequency. The cranking method and its three-dimensional version,

so-called tilted axis cranking method, have been successfully applied to the rotational bands at the high-spin states. Therefore, the cranked wave function is suitable as the intrinsic wave function of the angular momentum projection calculation, especially for the high-spin states. In this way we can take into account the effects of the collective rotation on the mean-field parameters like the deformations and the pairing gaps.

2.2 Angular momentum projection method

2.2.1 Restoration of rotational symmetry

Because of the nonlinearity of the HFB equation, the mean-field state generally breaks various symmetries, and it is necessary to restore the symmetries broken in it. The angular momentum projection method is the fully microscopic approach to the nuclear rotational states. Its concept follows the idea that the rotational invariance is restored by superposing the rotated states with the same energy.

The rotation operator is defined as

$$\hat{R}(\omega) = e^{i\alpha\hat{J}_z} e^{i\beta\hat{J}_y} e^{i\gamma\hat{J}_z}, \tag{2.34}$$

where $\omega = (\alpha, \beta, \gamma)$ stands for the Euler angles. Since the Hamiltonian $\hat{H}$ has the rotational invariance, it commutes with rotation operator,

$$\langle\Phi|\hat{H}|\Phi\rangle = \langle\Phi|\hat{R}^\dagger(\omega)\hat{H}\hat{R}(\omega)|\Phi\rangle. \tag{2.35}$$

This indicates that an infinite number of the rotated states $\hat{R}(\omega)|\phi\rangle$ are degenerate energetically. To restore the rotational symmetry, we introduce the ansatz

$$|\Psi^I_M\rangle = \int d\omega f^I_M(\omega)\hat{R}(\omega)|\Phi\rangle, \tag{2.36}$$

which superposes the rotated states $\hat{R}(\omega)|\phi\rangle$ with the weight function $f^I_M(\omega)$. Since the Wigner functions are a complete set of orthogonal functions of the Euler angles, $f^I_M(\omega)$ can be expanded as

$$f^I_M(\omega) = \sum_K g^I_K \frac{2I+1}{8\pi^2} {D^I_{MK}}^*(\omega). \tag{2.37}$$

We define the angular momentum projector $\hat{P}^I_{MK}$,

$$\hat{P}^I_{MK} = \frac{2I+1}{8\pi^2} \int d\omega {D^I_{MK}}^*(\omega)\hat{R}(\omega). \tag{2.38}$$

The equation (2.36) is written as

$$|\Psi^I_M\rangle = \frac{2I+1}{8\pi^2} \sum_K \int d\omega g^I_K {D^I_{MK}}^*(\omega)\hat{R}(\omega)|\phi\rangle = \sum_K g^I_K \hat{P}^I_{MK}|\Phi\rangle. \tag{2.39}$$

The projector $\hat{P}^I_{MK}$ satisfies the relations

$$\hat{P}^I_{MK}{}^\dagger = \hat{P}^I_{KM}, \tag{2.40}$$

$$\hat{P}^I_{KM}\hat{P}^{I'}_{M'K'} = \delta_{II'}\delta MM'\hat{P}^I_{KK'}. \tag{2.41}$$

Because of the rotational invariance of the Hamiltonian $\hat{H}$, the projector $\hat{P}^I_{MK}$ commutes with $\hat{H}$,

$$[\hat{H}, \hat{P}^I_{MK}] = 0. \tag{2.42}$$

Acting the projector $\hat{P}^I_{MK}$ is equivalent to restoring the rotational symmetry of the mean-field states. By using the cranked wave function, where the time reversal symmetry is broken, as a intrinsic state, the rotational states $|\Psi^I_M\rangle$ can include the components with odd K quantum numbers, i.e., time-odd components.

To obtain the rotational states, it is necessary to determine the coefficients g^I_K. It is determined to minimize the projected energy $E^I(g)$,

$$E^I(g) = \frac{\sum_{KK'} g^I_K{}^* \mathcal{H}^I_{KK'} g^I_{K'}}{\sum_{KK'} g^I_K{}^* \mathcal{N}^I_{KK'} g^I_{K'}} \tag{2.43}$$

where the Hamiltonian kernel $\mathcal{H}^I_{KK'}$ and the norm kernel $\mathcal{N}^I_{KK'}$ are defined as

$$\left\{ \begin{array}{c} \mathcal{H}^I_{K,K'} \\ \mathcal{N}^I_{K,K'} \end{array} \right\} = \langle\Phi| \left\{ \begin{array}{c} \hat{H} \\ 1 \end{array} \right\} \hat{P}^I_{KK'}|\Phi\rangle. \tag{2.44}$$

From the variational principle for the energy $E^I(g)$, the Hill-Wheeler equation,

$$\sum_{K'} \mathcal{H}^I_{K,K'}\ g^I_{K'} = E^I \sum_{K'} \mathcal{N}^I_{K,K'}\ g^I_{K'}, \tag{2.45}$$

is derived. By solving this generalized eigenvalue equation, we determine the coefficients g^I_K and obtain the final nuclear rotational states $|\Psi^I_M\rangle$.

2.2.2 Electromagnetic transition probabilities

To understand the nuclear rotational motion, the electromagnetic transition probability is one of the important quantities, since the states in the rotational band are connected by the low-multipole electromagnetic (E2, M1) transitions. For example, for the wobbling band and chiral band, which are very interesting and will be explained in more detail in the following chapter, the characteristic transition probabilities are a key to identify them. The $B(E2)$ and $B(M1)$ transition probabilities are given by

$$B(E2; I_i \to I_f) = \frac{1}{2I_i+1}|\langle\Phi^{I_f}_{M_f}\|\hat{Q}_2\|\Phi^{I_i}_{M_i}\rangle|^2, \tag{2.46}$$

$$B(M1; I_i \to I_f) = \frac{1}{2I_i+1}|\langle\Phi^{I_f}_{M_f}\|\hat{M}_1\|\Phi^{I_i}_{M_i}\rangle|^2, \tag{2.47}$$

where $|\Phi^{I_i}_{M_i}\rangle$ and $|\Phi^{I_f}_{M_f}\rangle$ are a initial and final states, respectively. The transition operators $\hat{Q}_{\lambda\mu}$ and $\hat{M}_{\lambda\mu}$ are defined as

$$\hat{Q}_{\lambda\mu} = er^{\lambda}Y_{\lambda\mu}(\theta,\phi), \tag{2.48}$$

$$\hat{M}_{\lambda\mu} = \mu_N(\nabla r^{\lambda}Y_{\lambda\mu}(\theta,\phi))\cdot(g_s\boldsymbol{s} + \frac{2g_l}{\lambda+1}\boldsymbol{l}). \tag{2.49}$$

For the angular momentum projected state in Eq. (2.39), the reduced matrix elements in Eq.(2.46) and (2.47) are written as

$$\langle\Phi^{I_f}_{M_f}||\hat{T}_{\lambda}||\Phi^{I_i}_{M_i}\rangle = (2I+1)(-)^{I-K}\sum_{\bar{\mu}\bar{K}}\begin{pmatrix} I & \lambda & I' \\ -K & \bar{\mu} & \bar{K}\end{pmatrix} \tag{2.50}$$

$$\times\frac{2I'+1}{8\pi^2}\int d\omega D^{I'}_{\bar{K}K'}{}^{*}(\omega)\langle\Phi|\hat{T}_{\lambda\bar{\mu}}\hat{R}(\omega)|\Phi\rangle, \tag{2.51}$$

where the $\hat{T}_{\lambda\mu}$ represents the transition operator $\hat{Q}_{2\mu}$ or $\hat{M}_{1\mu}$.

The B(E2) transition probabilities within a rotational band provide us the information of the nuclear shape. The relation between the B(E2) value and the quadrupole moment Q_{20}, which is obtained in the framework of the rotor model, is given by

$$B(\mathrm{E2}; I+2\to I) = \frac{3}{2}\frac{(I+1)(I+2)}{(2I+3)(2I+5)}Q^2_{20}. \tag{2.52}$$

This equation is usually used to determine the experimental quadrupole moment from the observed B(E2) value.

2.3 Generator coordinate method (GCM)

For the microscopic description of the nuclear collective motions, the wave functions should include as many correlations as possible. We introduce the following GCM ansatz,

$$|\Psi\rangle = \int dq|\Phi(q)\rangle g(q), \tag{2.53}$$

which is a continuous superposition of generating functions $|\Phi(q)\rangle$, which is labeled by a generating coordinate q, with the weight function $g(q)$. The weight function $g(q)$ is determined from the variational principle. The energy of the GCM is given by

$$E(g(q)) = \frac{\langle\Psi|\hat{H}|\Psi\rangle}{\langle\Psi|\Psi\rangle} = \frac{\int dqdq'g^*(q)\mathcal{H}(q,q')g(q')}{\int dqdq'g^*(q)\mathcal{N}(q,q')g(q')}, \tag{2.54}$$

with overlaps $\mathcal{H}^I_{KK'}$ and $\mathcal{N}^I_{KK'}$ defined by

$$\left\{\begin{array}{c}\mathcal{H}(q,q')\\ \mathcal{N}(q,q')\end{array}\right\} = \langle\Phi(q)|\left\{\begin{array}{c}\hat{H}\\ 1\end{array}\right\}|\Phi(q')\rangle. \tag{2.55}$$

From the variation with respect to $g(q)$, we obtain the Hill-Wheeler equation,

$$\int dq\,(\mathcal{H}(q,q') - E\mathcal{N}(q,q'))\,g(q) = 0. \tag{2.56}$$

In numerical calculations, the discretized version of the GCM is used. The wave function and the Hill-Wheeler equation become the following:

$$|\Psi\rangle = \sum_n |\Phi(q_n)\rangle g(q_n), \tag{2.57}$$

$$\sum_{n'} (\mathcal{H}(q_n,q_{n'}) - E\mathcal{N}(q_n,q_{n'}))\,g(q_{n'}) = 0. \tag{2.58}$$

When solving the Hill-Wheeler equation, the states with norm eigenvalues that are smaller than a certain value, the so-called norm cut-off, are excluded. The proper value should be chosen for the norm cut-off; it should be small enough not to miss important contributions, while it should not be too small in order to avoid the numerical difficulty in the GCM related to the vanishing norm states [14].

Since the generating functions $|\Phi(q_n)\rangle$ are not orthogonal, the weight function $g(q_n)$ cannot be considered as amplitudes for the probability. Instead of it, we introduce the normalized amplitude [14],

$$f(q_n) = \sum_{n'} (\sqrt{\mathcal{N}})(q_n,q_{n'})g(q_{n'}), \tag{2.59}$$

and its modulus square $|f(q_n)|^2$ is interpreted as the probability of the n-th state $|\Phi(q_n)\rangle$. Here, the matrix $\sqrt{\mathcal{N}}$ is the square root of the norm kernel $\mathcal{N}$.

We should choose an appropriate set of generating coordinate depending on the nuclear collective motion. The angular momentum projection method is a special case of the GCM, where the Euler angles are chosen to be the generating coordinates. For nuclear rotational states, not only the correlation related to symmetry restoration but also the effect of the fluctuation of the quadrupole deformation may play a role. Therefore, we introduce the following angular momentum projected configuration mixing with respect to the quadrupole deformation,

$$|\Psi^I_M\rangle = \sum_{Kn} g^I_{Kn} \hat{P}^I_{MK} |\Phi(Q^{(n)}_{20})\rangle, \tag{2.60}$$

which is the superposition of the projected states $\hat{P}^I_{MK}|\Phi(Q^{(n)}_{20})\rangle$. Here, the quadrupole moment Q_{20} is given by

$$Q_{20} = \langle\Phi|\hat{Q}_{20}|\Phi\rangle = \langle\Phi|r^2 Y_{20}|\Phi\rangle. \tag{2.61}$$

By the constrained HFB calculations, a set of the mean-field states with various quadrupole moments $|\Phi(Q^{(n)}_{20})\rangle$ are obtained. The coefficients g^I_{Kn} are determined by solving the following Hill-Wheeler equation,

$$\sum_{K'n'} \mathcal{H}^I_{Kn,K'n'}\; g^I_{K'n'} = E^I \sum_{K'n'} \mathcal{N}^I_{Kn,K'n'}\; g^I_{K'n'}, \tag{2.62}$$

where

$$\left\{ \begin{array}{c} \mathcal{H}^I_{Kn,K'n'} \\ \mathcal{N}^I_{Kn,K'n'} \end{array} \right\} = \langle \Phi(Q_{20}^{(n)})| \left\{ \begin{array}{c} \hat{H} \\ 1 \end{array} \right\} \hat{P}^I_{KK'} |\Phi(Q_{20}^{(n')})\rangle. \tag{2.63}$$

The probability of n-th projected states $\hat{P}^I_{MK}|\Phi(Q_{20}^{(n)})\rangle$ is given by

$$p^I(Q_{20}^{(n)}) = \sum_K |f^I_{Kn}|^2, \tag{2.64}$$

with

$$f^I_{Kn} = \sum_{n'K'} (\sqrt{\mathcal{N}})^I_{Kn,K'n'} g^I_{K'n'}. \tag{2.65}$$

2.4 Gogny interaction

Since the bare nucleon-nucleon force shows the strong repulsion at the short distance and cannot be treated in the mean-field framework, the effective two-body interaction is generally used. The zero-range Skyrme [22] and the finite-range Gogny [23] forces are well known as the phenomenological effective two-body interactions in the nuclear structure calculations, which have the density-dependent term. The pairing part of the Gogny interaction is not arbitrary, which is different from the Skyrme interaction.

The Gogny interaction consists of three terms; the central v_{12}^{C}, the spin-orbit v_{12}^{LS} and the density-dependent forces v_{12}^{DD},

$$v_{12} = v_{12}^{\mathrm{C}} + v_{12}^{\mathrm{LS}} + v_{12}^{\mathrm{DD}}, \tag{2.66}$$

$$v_{12}^{\mathrm{C}} = \sum_{i=1,2} (W_i + B_i P_\sigma - H_i P_\tau - M_i P_\sigma P_\tau) \exp\left(-\frac{r^2}{\mu_i^2}\right), \tag{2.67}$$

$$v_{12}^{\mathrm{LS}} = iW_{LS}(\sigma_1 + \sigma_2) \cdot \boldsymbol{k}' \times \delta(\boldsymbol{r}_1 - \boldsymbol{r}_2)\boldsymbol{k}, \tag{2.68}$$

$$v_{12}^{\mathrm{DD}} = t_3(1 + x_3 P_\sigma)\rho^\alpha \left(\frac{\boldsymbol{r}_1 + \boldsymbol{r}_2}{2}\right) \delta(\boldsymbol{r}_1 - \boldsymbol{r}_2), \tag{2.69}$$

where P_σ and P_τ are the operators that exchange the spin and isospin coordinates, respectively,

$$P_\sigma = \frac{1 + \sigma_1 \cdot \sigma_2}{2}, \ P_\tau = \frac{1 + \tau_1 \cdot \tau_2}{2}, \tag{2.70}$$

and the operators $\boldsymbol{k}$ and $\boldsymbol{k}'$ act the right- and left-handed states, respectively,

$$\boldsymbol{k} = \frac{\nabla_1 - \nabla_2}{2i}, \ \boldsymbol{k}' = \frac{\nabla_1 - \nabla_2}{2i}, \ r = |\boldsymbol{r}_1 - \boldsymbol{r}_2|. \tag{2.71}$$

The part of the central force is expanded by two-range Gaussian functions and the spin-orbit and density-dependent force are assumed to be the zero-range force. The term of the tensor force is not included. The Coulomb interaction is taken into account by

$$v_{12}^{\mathrm{coul}} = \frac{e^2}{r}. \tag{2.72}$$

There are various parameter sets for the Gogny interaction; D1, D1S, D1N parameter set, etc. In the present work, we employ the Gogny-D1S parameter set [24], which well reproduces the properties of various nuclei in the whole nuclear chart. The parameters were also adjusted to reproduce the properties of the nuclear matter, and are given in Table 2.1.

i	W_i	B_i	H_i	M_i	μ_i
1	1720.3	1300	1813.53	1397.6	0.7
2	103.64	163.48	162.81	-223.93	1.2

x_3	α	t_3	W_{LS}
1	$\frac{1}{3}$	1390.6	130

Table 2.1: Gogny-D1S parameter set.

Chapter 3

Application to low-spin states of Mg isotopes

3.1 Introduction

Recent development of accelerators provides us a lot of experimental data for the neutron-rich nuclei, and nuclear properties in the so-called island of inversion have been intensively studied both experimentally and theoretically. The island of inversion is the region where the neutron number N is around 20 and the proton number Z is from 10 (Ne) to 12 (Mg), and shows the interesting properties like the change of the magic number and the large deformation, which are not predicted from the study of the stable nuclei. Recently, the experimental data for Mg isotopes close to the neutron drip line are obtained; the excitation energies $E(2^+)$ and $E(4^+)$, the $B(\mathrm{E2})$ transition probabilities and the reaction cross sections.

By the mean-field calculations, the ground state of the nucleus ^{32}Mg with $N = 20$ is predicted to have a spherical shape. However, the experimental values of the $B(\mathrm{E2}; 0^+ \to 2^+)$ transition probability [3, 4, 5], the excitation energy of the 2^+ state $E(2^+)$ and the ratio $E(4^+)/E(2^+)$ [6] in ^{32}Mg indicate a large deformation. On the other hand, in the beyond mean-field framework like the projection method, the nucleus ^{32}Mg is predicted to have a deformed ground state. In the case of nuclei around $N = 28$, not only beyond mean-field but also mean-field calculations predict the deformed ground states, which indicates that the $N = 28$ shell closure is more fragile than the $N = 20$ one.

For nuclei in this region, the effect of restoring the rotational invariance on the deformation is important, and especially in the case that the energy difference at the prolate and oblate minimums is small, the large change of the deformation parameters appears; the effect of the fluctuation of the quadrupole deformation also should be taken into account. Rotational states except for the 0^+ state are described by the superposition of the states with different K quantum numbers, and time-odd components induced by the cranking model may play an important role for the 2^+ and 4^+ states. For the low-spin states of even-even Mg isotopes, we perform the angular

momentum projection method with the quadrupole configuration mixing employing the Gogny D1S effective interaction, and investigate the effects of the configuration mixing and of the time-odd components. In this calculation, we use the harmonic oscillator basis with $N_{\rm osc}^{\rm max} = 8$.

3.2 Energy surface

Since the quadrupole moment Q_{20} depends on the nuclear size, it is not so convenient for considering the nuclear shape. Instead of it, we define the deformation parameter β_2 in our Gogny-HFB calculations,

$$\beta_2 = \frac{4\pi}{5}\frac{\langle r^2 Y_{20}\rangle}{\langle r^2\rangle}. \tag{3.1}$$

The potential energy curve, which is the energy as a function of the deformation parameter β_2, is a starting point to consider the nuclear deformation. It clearly indicates the occurrence of the deformation as well as the stability of the deformation. In the projection calculation from one intrinsic state $|\Phi(\beta_2)\rangle$, the projected states $|\Psi_M^I(\beta_2)\rangle$ are obtained depending on the quadrupole deformation parameter β_2. In present calculations, the deformation parameter β_2 is determined to minimize the energy from the potential energy curve of the projection calculation.

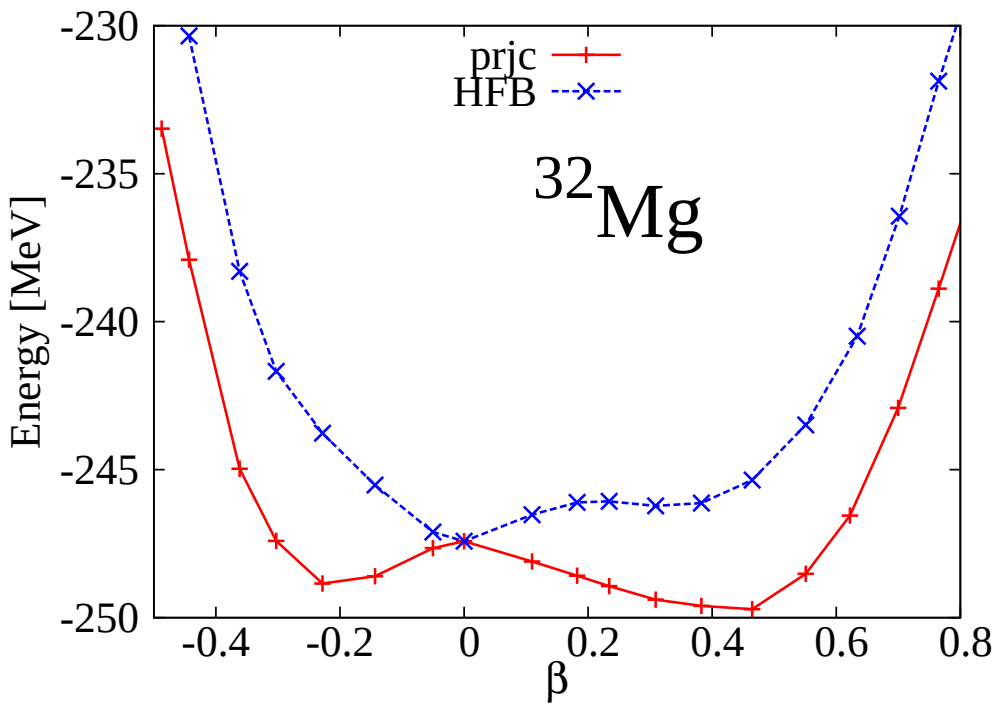

Figure 3.1: Potential energy curves of the HFB ("HFB") and projection ("prjc") calculation for ^{32}Mg with the Gogny-D1S interaction. In the projection calculations, the ground-state ($I^\pi = 0^+$) energies are plotted.

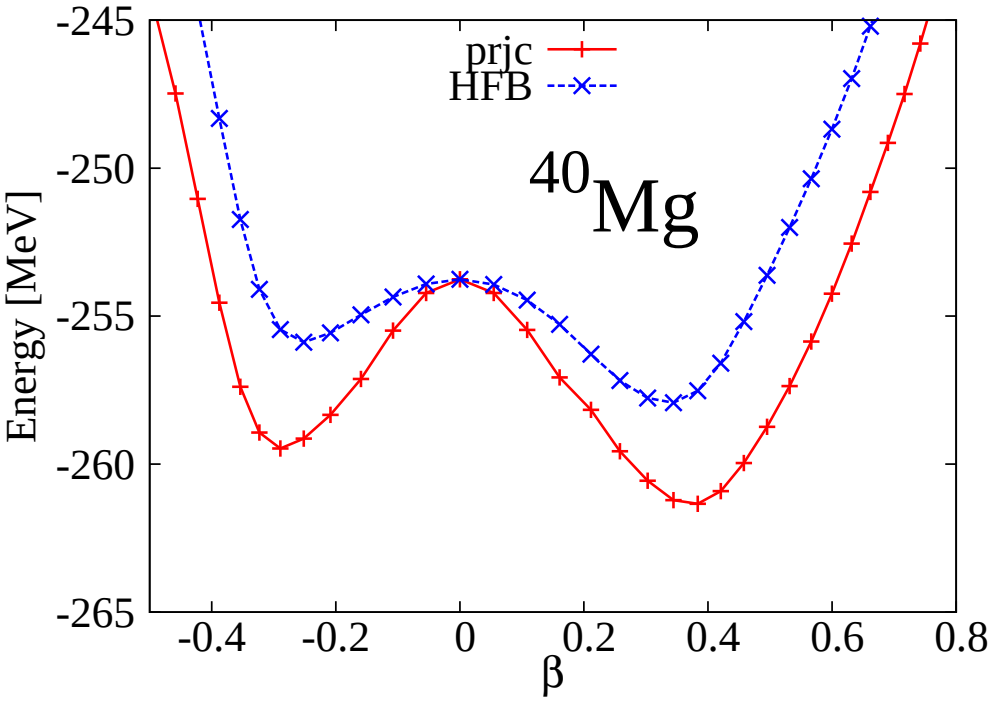

Figure 3.2: Potential energy curves of the HFB ("HFB") and projection ("prjc") calculation for ^{40}Mg with the Gogny-D1S interaction. In the projection calculations, the ground-state ($I^\pi = 0^+$) energies are plotted.

The ground-state potential energy curves of the HFB (dashed line) and angular momentum projection (solid line) calculations are shown for the nucleus ^{32}Mg in Fig. 3.1. Large energy gains are obtained for the deformed states by the angular momentum projection, while there is no energy gain for the spherical case. For the nucleus ^{32}Mg, the spherical minimum is found in the HFB calculation. On the other hand, in the projection calculation the considerably large prolate deformation ($\beta_2 \approx 0.42$) is favored, which is consistent with the suggestion by the experiment [3, 4, 5, 6]. To obtain the correct nuclear deformation, it is important to perform the angular momentum projection. The spherical barrier, corresponding to the energy difference between the prolate and spherical states, is not so large ($\Delta E \approx 2.3$ MeV). The oblate minimum is found at $\beta_2 \approx -0.23$, and the energy difference between the prolate and oblate states is $\Delta E \approx 870$ keV. These results indicate that the effect of the quadrupole configuration mixing on the rotational states should be taken into account. The ground-state potential energy curves for the nucleus ^{40}Mg are shown in Fig. 3.2. For the nucleus ^{40}Mg, the prolate deformed state is favored in both the HFB and the projection calculations, and in contrast to the case of ^{32}Mg, the considerably deep prolate minimum is obtained. The spherical barrier is large ($\Delta E \approx 5.7$ MeV). The oblate minimum is found at $\beta_2 \approx -0.38$, and the energy difference between the prolate and oblate states is $\Delta E \approx 1.8$ MeV. Thus, for ^{40}Mg, the effect of the quadrupole configuration mixing may be small.

Fig. 3.3 shows the deformation parameters at the HFB (open square) and projected

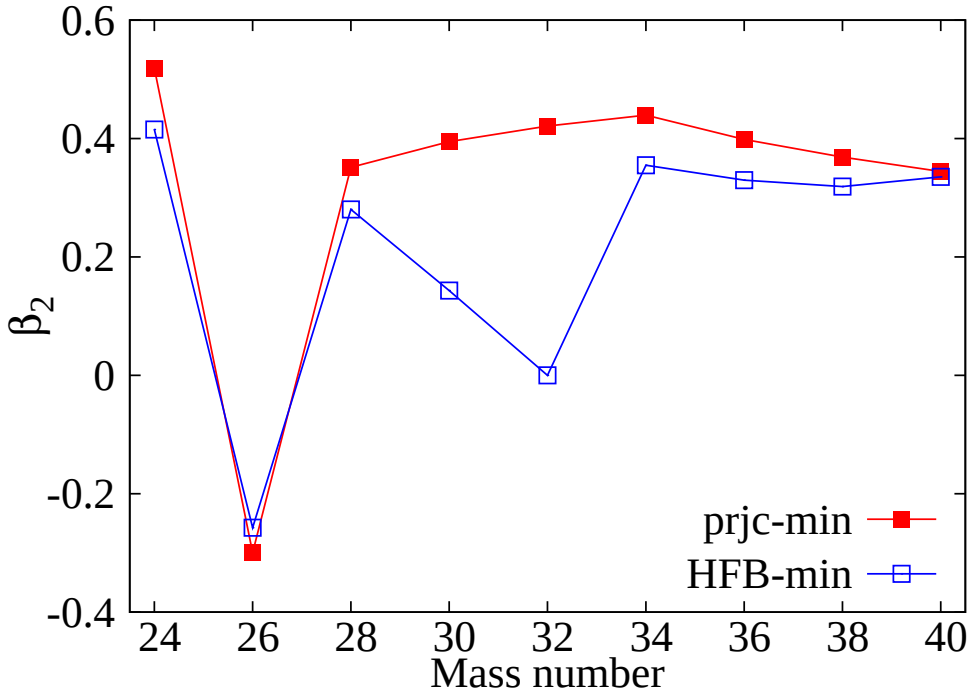

Figure 3.3: Deformation parameters β_2 for the Mg isotopes at the HFB ("HFB-min") and projected ("prjc-min") minima of the potential energy curves.

(closed square) minima for the Mg isotopes. Deformation parameters for ^{30,32}Mg are very different in these two calculations. The states with the deformation parameter at the projected minimum are adopted for the projection calculation from one intrinsic state. The effect of restoring the rotational invariance strongly contributes to the nuclear deformation.

3.3 Results

In this section, the excitation energies $E(2^+)$ and $E(4^+)$, the ratios $E(4^+)/E(2^+)$, the root mean square (rms) radii and the $B(E2)$ transition probabilities are presented, comparing the results of three calculations; the angular momentum projection calculation with both time-odd components induced by the cranking model and the β_2-configuration mixing, the calculation with time-odd components but without the β_2-configuration mixing, and the calculation without time-odd components but with the β_2-configuration mixing. In the configuration mixing calculations, 10 states whose deformation parameters are in the range $-0.5 \lesssim \beta_2 \lesssim 0.8$ (more precisely shown in Table. 3.1) are used, and in the calculations with the time-odd components the cranking frequency $\omega_{\rm rot} = 0.01$ MeV is used. The values of the norm cut-off are taken to be 10^{-7} in calculations for the nuclei ^{24,26}Mg with the β_2-configuration mixing and time-odd components and are taken to be 10^{-10} in other calculations.

The 2^+ and 4^+ excitation energies $E(2^+)$ and $E(4^+)$ are plotted in Fig. 3.4. The

nuclide	$\beta_2^{(n)}; n = 1:10$									
^{24}Mg	−0.45	−0.32	−0.15	0.04	0.23	0.41	0.55	0.66	0.75	0.83
^{26}Mg	−0.50	−0.40	−0.26	0.07	0.12	0.30	0.45	0.58	0.69	0.78
^{28}Mg	−0.49	−0.37	−0.21	0.02	0.19	0.37	0.52	0.65	0.75	0.83
^{30}Mg	−0.52	−0.41	−0.27	0.09	0.11	0.30	0.47	0.60	0.71	0.80
^{32}Mg	−0.49	−0.37	−0.23	0.05	0.13	0.31	0.46	0.60	0.70	0.79
^{34}Mg	−0.49	−0.38	−0.23	0.05	0.14	0.32	0.48	0.60	0.72	0.82
^{36}Mg	−0.50	−0.38	−0.23	0.04	0.15	0.33	0.48	0.61	0.73	0.82
^{38}Mg	−0.50	−0.39	−0.24	0.06	0.13	0.31	0.46	0.59	0.70	0.79
^{40}Mg	−0.50	−0.38	−0.24	0.05	0.14	0.32	0.46	0.60	0.70	0.79

Table 3.1: Sets of the quadrupole deformation parameters for the configuration mixing ($\beta_2^{(n)}; n = 1:10$).

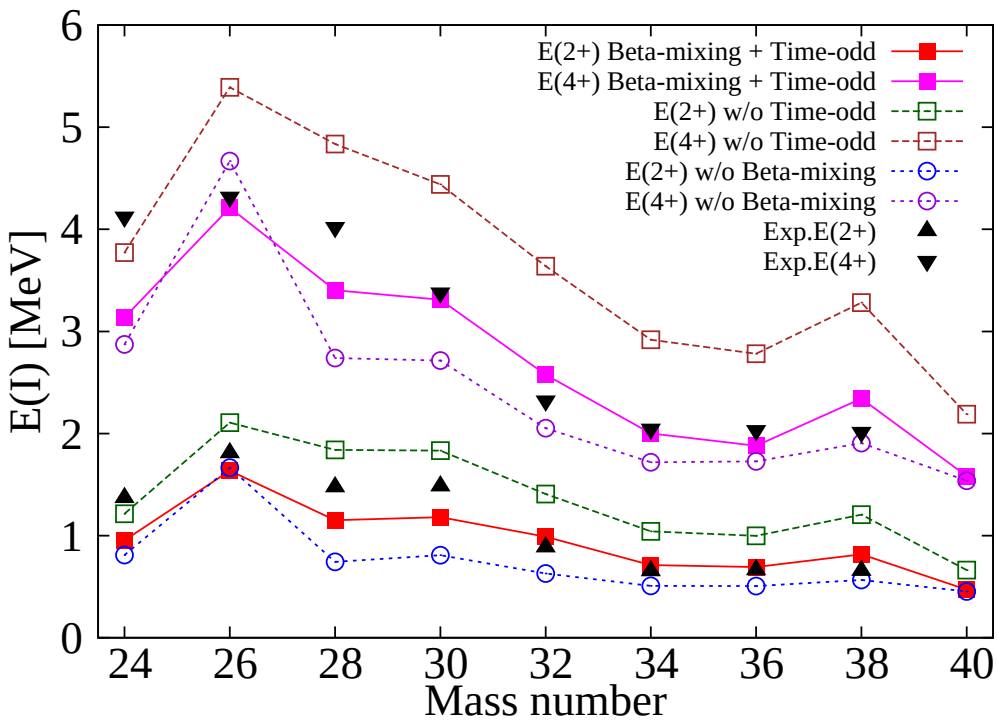

Figure 3.4: Excitation energies $E(2^+)$ and $E(4^+)$ for Mg isotopes. The calculations by three methods, the angular momentum projection method with both time-odd components and β_2-mixing ("beta-mixing + time-odd"), with time-odd components but without β_2-mixing ("w/o beta-mixing"), and without time-odd components and but β_2-mixing ("w/o time-odd'), are compared. Experimental data ("Exp.") are are taken from Ref. [6, 25] and references therein.

excitation energies with both the β_2-configuration mixing and time-odd components induced by the cranking model (solid line) agree well with the experimental data systematically. However, the results for the nucleus ^{24}Mg underestimate the experimental values. It is due to the fact that in the Gogny-D1S calculation, the pairing gaps vanish around the projected minimum. The excitation energies without the β_2-configuration mixing (dotted line) are systematically lower than experimental data. The β_2-configuration mixing considerably increase the excitation energies of the 2^+ and 4^+ states. On the other hand, the results without the time-odd components (dashed line) overestimate the experimental data very much. This is due to the fact that the effects of the time-odd components induced by the cranking model do not contribute the 0^+ states. As a result, they reduce the excitation energies. Therefore, for the Mg isotopes, both the effects of the β_2-configuration mixing and the time-odd components are important to reproduce the excitation energies for the 2^+ and 4^+ states.

Fig. 3.5 and 3.6 show the probability distributions of the $0^+, 2^+$ and 4^+ states by calculations with the β_2-configuration mixing. For nuclei ^{24,34,40}Mg, the distributions of the 0^+, 2^+ and 4^+ states are well located in the prolate deformation side. The distributions of excited states except for ^{26}Mg are also located in the prolate side. However, the distribution of the ground state has the spread in both the oblate and prolate sides. In particular, almost uniform distribution is seen in the wide range around the spherical shape for the 0^+ state in ^{30}Mg. This indicates that both the prolate and oblate configurations contribute the ground-state wave function. For the nucleus ^{26}Mg, an interesting transition of the distribution from the oblate to prolate side occurs; for the ground state the major part of mixing probabilities is in the oblate side, while for the 4^+ state it is in the prolate side. Comparing the distributions with and without time-odd components induced by the cranking model (Fig. 3.5 and 3.6), they are not so different. For the nuclei $^{26-30}$Mg, a slight change of 2^+ and 4^+ distributions are seen. Since the time-odd components induced by the cranking model do not contribute the 0^+ state, which consists of only $K = 0$ states, there is no effect on the 0^+ distributions.

The ratios $E(4^+)/E(2^+)$ are shown in Fig. 3.7. The results of calculations with the β_2-configuration mixing agree well with the experimental values. Calculations without the β_2-configuration mixing show the values around the ideal rotational ratio of 3.3. Inclusion of the effects of β_2-fluctuations reduces the ratio. It clearly indicates that the effects of the β_2-fluctuation included by the β_2-configuration mixing are very important to describe the deviation from the ideal rotational behavior. The ideal ratio of the vibrational motion is $E(4^+)/E(2^+) = 2$. On the other hand, comparing the results with and without time-odd components induced by the cranking model, only a small influence on the ratio is observed. This may be because of the fact that there are no drastic changes of the mixing probability distributions for calculations with the time-odd components. The effect of time-odd components reduces the excitation energies keeping the ratio constant; namely it only increases the moment of inertia without changing the property of the rotational motion. Therefore, only the β_2-configuration

mixing has the large influence on the ratio $E(4^+)/E(2^+)$.

Fig. 3.8 shows the root mean square (rms) radii. Our three calculations by angular momentum projection method show a very good agreement with the experimental data. The effects of the β_2-configuration mixing are rather small influence on the nuclear radius. Since the rms radii in Fig. 3.8 are calculated for the 0^+ state, the time-odd components have no effect on them. On the other hand, comparing with the result of the deformed HFB, the angular momentum projection gives non-negligible effects on the rms radius. This is due to the fact that the equilibrium deformation parameters are changed by the angular momentum projection calculation. The difference between the results of the projection and spherical HFB indicates the effect of nuclear deformation. It is apparent that the nuclear deformation plays an important role for the nuclear radius. Therefore, for the rms radius it is important to determine the correct deformation parameter. The radius $R_0 = 1.2A^{1/3}$ is widely used as a nuclear radius, and the corresponding rms radius $1.2A^{1/3}(3/5)^{1/2}$ is also plotted. It is found that the densities of Mg isotopes are much more extended than the typical nuclear density with $R_0 = 1.2A^{1/3}$.

Finally the $B(\mathrm{E2};0^+ \to 2^+)$ transition probabilities are plotted in Fig. 3.9. No effective charge is used in our calculations of the transition probabilities. For the $B(E2)$ values, both the β_2-configuration mixing and time-odd components have the influence on the $B(E2)$ by about 10%. The agreement with the available experimental data is rather satisfactory considering the fact that our calculations have no adjustable parameters.

3.4 Short summary

Before the angular momentum projection method is applied to the high-spin state, we have shown the result of its application to the low-spin state in this section. We studied the low-spin rotational states for Mg isotopes by the angular momentum projection method with the quadrupole configuration mixing. The Gogny-D1S interaction is employed as a effective interaction and there are no adjustable parameters in this calculation.

Our calculations show the systematic agreement with the experimental data for the excitation energies $E(2^+)$ and $E(4^+)$, the ratios $E(4^+)/E(2^+)$, the rms radii and the $B(E2)$ transition probabilities. The effects of the quadrupole mixing and the time-odd components induced by the cranking model on these quantities are investigated. Both effects play an important role for the excitation energies, and have a considerable influence on the $B(E2)$ values. For the ratio $E(4^+)/E(2^+)$, it is important to include the effect of the quadrupole mixing. On the other hand, both effects have small influence on the nuclear radius. For the rms radius, however, it is important to obtain the correct nuclear deformation parameter, which is obtained by applying the angular momentum projection method. Thus, the angular momentum projection method is useful tool for the microscopic study of the nuclear rotational states.

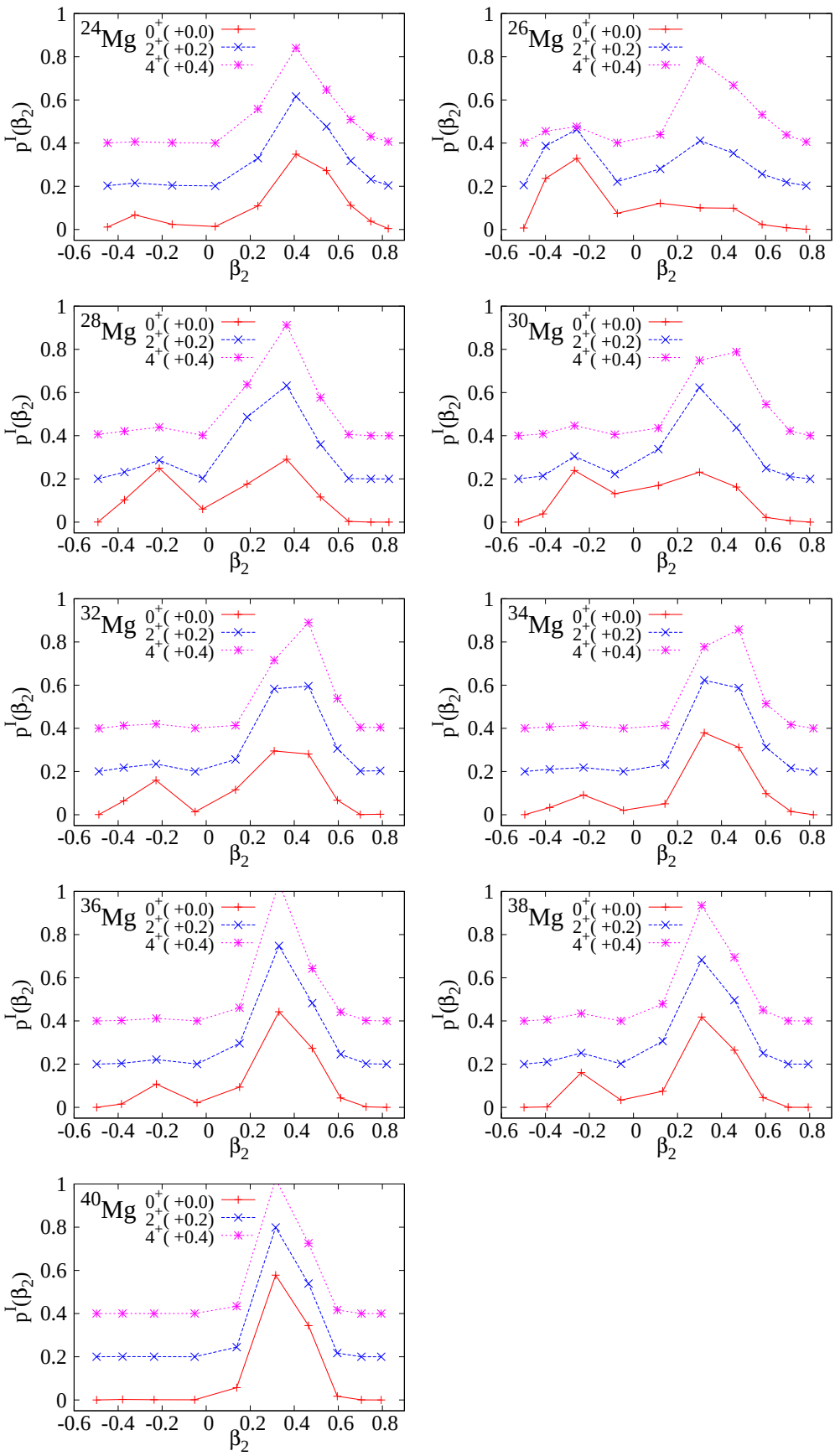

Figure 3.5: Probability distributions by the calculations with time-odd components for Mg isotopes. The result of the $0^+, 2^+$ and 4^+ states are plotted. The corresponding distributions are shifted +0.2 and +0.4 for the 2^+ and 4^+ states, respectively.

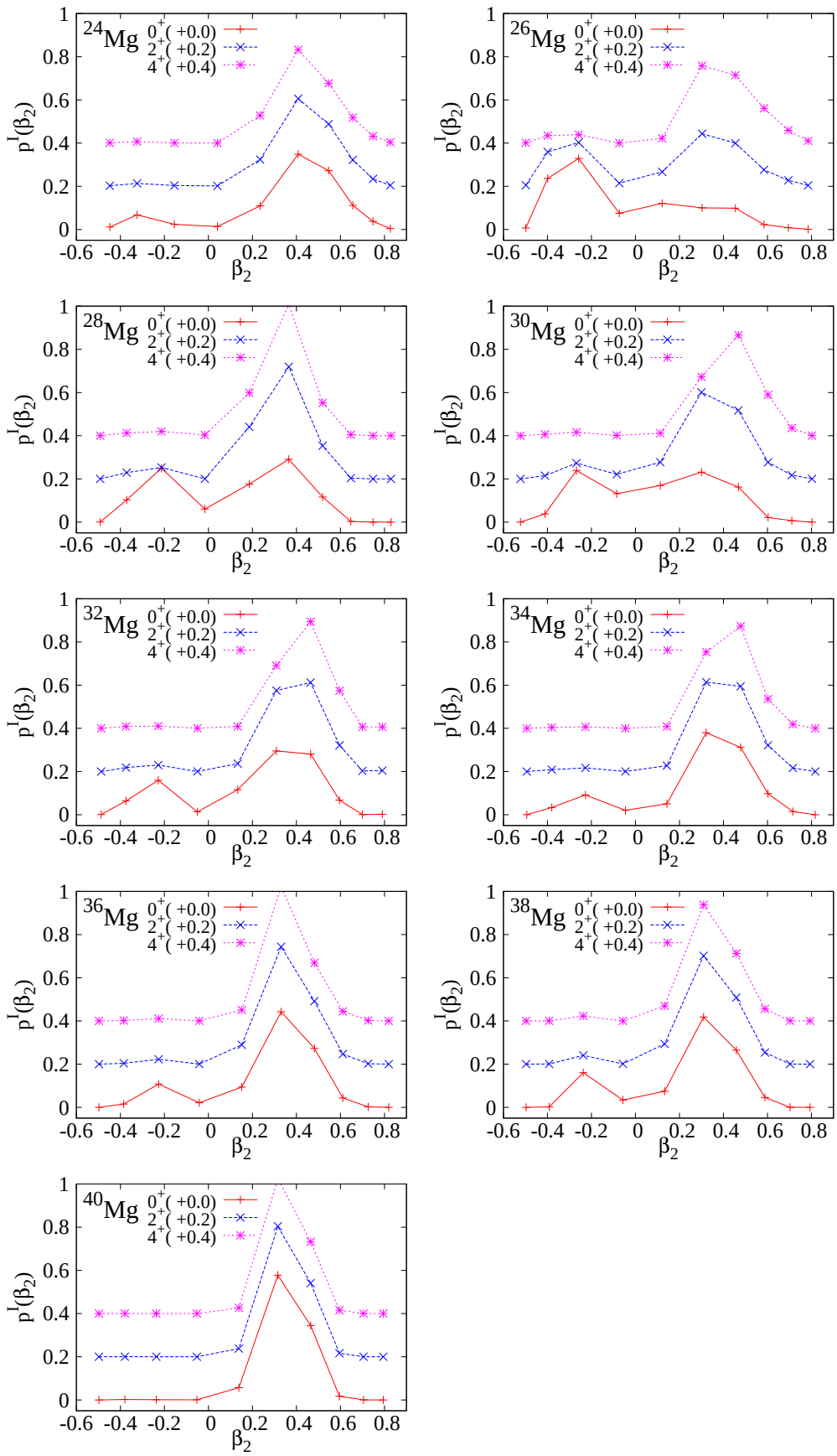

Figure 3.6: Probability distributions (Eq. (2.64)) of the calculations without time-odd components for Mg isotopes. The result of the $0^+, 2^+$ and 4^+ states are plotted. The corresponding distributions are shifted +0.2 and +0.4 for the 2^+ and 4^+ states, respectively.

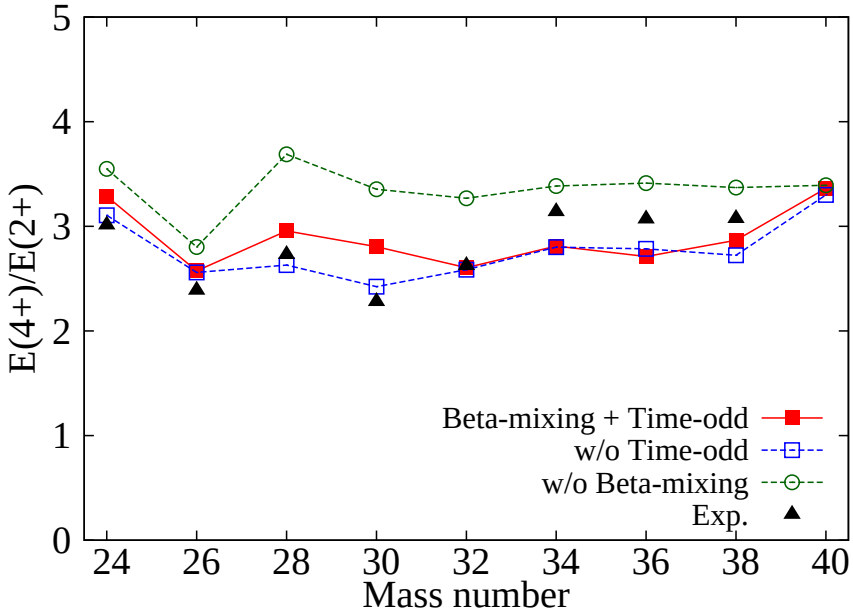

Figure 3.7: Ratios $E(4^+)/E(2^+)$ for Mg isotopes. The result of three calculations, the angular momentum projection method with time-odd components and β_2-mixing ("beta-mixing + time-odd"), with time-odd components but without β_2-mixing ("w/o beta-mixing"), and without time-odd components but with β_2-mixing ("w/o time-odd'), are compared.

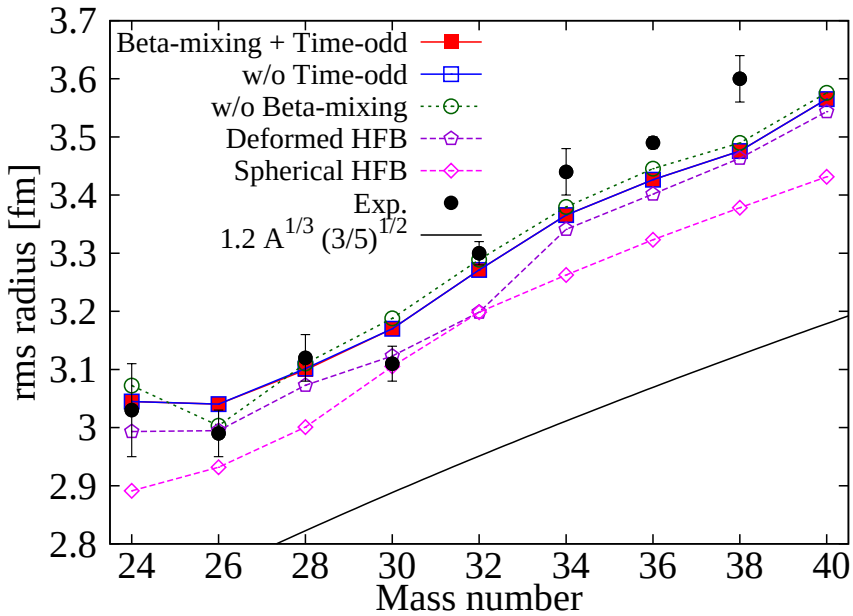

Figure 3.8: Root mean square radii for Mg isotopes. The three calculations, the angular momentum projection with both time-odd components and β_2-mixing ("beta-mixing + time-odd"), with time-odd components but without β_2-mixing ("w/o beta-mixing"), and without time-odd components but with β_2-mixing ("w/o time-odd'), are compared. For comparison, deformed and spherical HFB results are also included. Experimental data ("Exp.") are taken from Ref. [26], and they are calculated from the data of reaction cross sections.

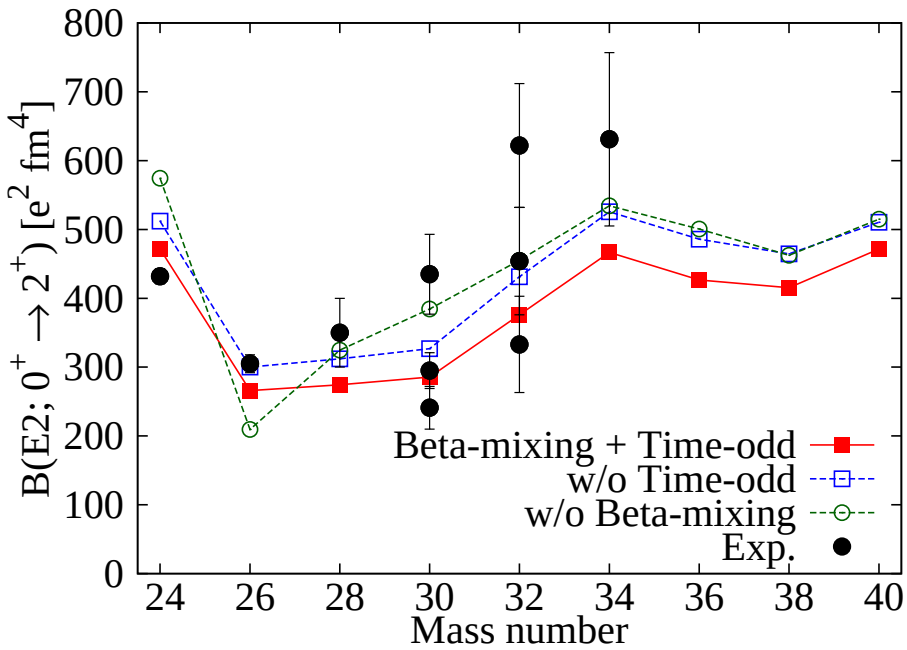

Figure 3.9: $B(E2)$ transition probabilities for Mg isotopes. The three calculations by the angular momentum projection method with both time-odd components and β_2-mixing ("beta-mixing + time-odd"), with time-odd components but without β_2-mixing ("w/o beta-mixing"), and without time-odd components but with β_2-mixing ("w/o time-odd'), are compared. Experimental data ("Exp.") are taken from Ref. [3, 4, 5, 27, 28, 29].

Chapter 4

Reliable calculation of high-spin rotational bands

4.1 Introduction

Although the angular momentum projection method is a microscopic approach to the nuclear rotational state, its technique has not been used very much for the description of the high-spin states, except for the work by using the projected shell model approach [30]. In this chapter, we propose a method to reliably calculate the high-spin states by the angular momentum projection technique using several cranked states.

As mentioned in Sec. 2.1.4, the cranked state is suitable as the intrinsic state of the angular momentum projection calculation since the effect of the collective rotation on the mean-field parameters can be efficiently included. However, there are some problems when calculating the high-spin states by the simple angular momentum projection from one intrinsic state. Although all the states belonging to a rotational band can be calculated by the angular momentum projection from one intrinsic state, the resultant spectrum is not very accurate, especially at the high spin; e.g., the calculated moment of inertia is almost constant or decreases with increasing spin while the most of the experimental inertias increase as a function of spin, which is mainly due to the Coriolis anti-pairing effect. The single-particle angular momentum vectors tend to align along the rotation axis due to the cranking term $-\omega_{\rm rot}J_y$, which causes the reduction of the pairing gap with increasing spin. In the projection from one intrinsic state, this effect cannot be taken into account since only one mean-field state, in which the pairing gap takes a definite value, is used as an intrinsic state. In addition, we are faced with the problem that how the projection method and the cranking model should be compromised. Since in the cranking model various cranked states are obtained depending their cranking frequencies, in the projection calculation we obtain a lot of different rotational bands depending various cranking frequencies. Therefore, it is a problem how to obtain a unique rotational band from these different bands with various frequencies. A possible way is to adopt for each spin the lowest-energy state among the different bands obtained by the projection with various

frequencies; it is based on the idea of the variation after projection. However, it has been shown that this approach does not necessarily work [31]; if only the cranking frequency is treaded as a variational parameter, it happens that the resultant rotational spectrum is not regular. In Ref. [31], it is recommended that the state calculated by the projection from one cranked state $|\Phi_{\rm cr}\rangle$ with the cranking frequency that satisfies $\langle\Phi_{\rm cr}|\hat{J}_y|\Phi_{\rm cr}\rangle = I\hbar$ is chosen as the spin I state. However, this approach is not efficient since we should repeat the angular momentum projection to obtain each spin state, and a lot of projection calculations are necessary to obtain the whole rotational band over a wide spin range.

Thus, we propose a different approach to compromise the angular momentum projection method and the cranking model. In this approach, the rotational states are obtained by superposing the multiple states calculated by the angular momentum projection from several cranked states with different cranking frequencies. We call this method "angular momentum projected multi-cranked configuration mixing". This idea is originally suggested by Peierls-Thouless as an analogy to the case of the translational motion [32]. In the translational motion, the superposition with respect to not only the position but also the velocity (the so-called "double projection") is necessary to obtain the correct inertial mass, i.e., the nucleon mass times the mass number. By applying to the three examples in Sec. 4.3, it is found that this method is very reliable for calculating the high-spin states: The resultant spectrum is essentially independent of the chosen set of the cranking frequencies, and its necessary number is rather small, something like four or five. We systematically apply this method to the ground-state bands of nuclei in the rare-earth region in Sec. 4.4.1 and investigate the Stockholm band (s-band) of the nucleus ^{164}Er in Sec. 4.4.2.

4.2 Angular momentum projected multi-cranked configuration mixing

The angular momentum projected multi-cranked configuration mixing starts from the following ansatz: The rotational state $|\Psi^I_{M,\alpha}\rangle$ is given by

$$|\Psi^I_{M,\alpha}\rangle = \sum_{Kn} g^I_{Kn,\alpha}\, \hat{P}^I_{MK}|\Phi(\omega^{(n)}_{\rm rot})\rangle, \tag{4.1}$$

which is a superposition of the projected states with different cranking frequencies, $\hat{P}^I_{MK}|\Phi(\omega^{(n)}_{\rm rot})\rangle$, with the amplitudes $g^I_{Kn,\alpha}$. The operator $\hat{P}^I_{MK}$ is the angular momentum projector, and the amplitude $g^I_{Kn,\alpha}$ is determined by solving the so-called Hill-Wheeler equation,

$$\sum_{K'n'} \mathcal{H}^I_{Kn,K'n'}\; g^I_{K'n',\alpha} = E^I_\alpha \sum_{K'n'} \mathcal{N}^I_{Kn,K'n'}\; g^I_{K'n',\alpha}, \tag{4.2}$$

where the Hamiltonian and norm kernels are defined as

$$\left\{ \begin{array}{c} \mathcal{H}^I_{Kn,K'n'} \\ \mathcal{N}^I_{Kn,K'n'} \end{array} \right\} = \langle \Phi(\omega^{(n)}_{\rm rot})| \left\{ \begin{array}{c} H \\ 1 \end{array} \right\} \hat{P}^I_{KK'} |\Phi(\omega^{(n')}_{\rm rot})\rangle. \tag{4.3}$$

In this method, the excited states ($\alpha = 1, 2, 3, \cdots$) as well as the ground state ($\alpha = 0$) are obtained for each spin I by the Hill-Wheeler equation. The set of intrinsic states with different cranking frequencies, $(\Phi(\omega^{(n)}_{\rm rot}); n = 1, 2, 3, \cdots, n_{\rm max})$ is generated by the cranked HFB calculations. Then the state in Eq. (4.1) is nothing else but the discretized version of

$$|\Psi^I_{M,\alpha}\rangle = \int d\omega_{\rm rot} \sum_K g^I_{K,\alpha}(\omega_{\rm rot})\, \hat{P}^I_{MK} |\Phi_{\rm cr}(\omega_{\rm rot})\rangle, \tag{4.4}$$

which was originally proposed by Peierls-Thouless [32].

As mentioned in Sec. 2.3, the probability of the n-th HFB state in the eigenstate $|\Psi^I_{M,\alpha}\rangle$ is given by

$$p^I_\alpha(\omega_{\rm rot}) = \sum_K |f^I_{K,\alpha}(\omega_{\rm rot})|^2. \tag{4.5}$$

with the properly normalized amplitude [14],

$$f^I_{Kn,\alpha} = \sum_{K'n'} \left(\sqrt{\mathcal{N}^I}\right)_{Kn,K'n'} g^I_{K'n',\alpha} \ . \tag{4.6}$$

In this calculation, we employ the Gogny-D1S effective interaction, and the Coulomb exchange contribution is treated in the Slater approximation although we are able to perform the exact calculation. In fact, the Coulomb interaction is exactly treated in Chap. 3. This is because the proton pairing correlation quite often vanishes (or becomes very small) in the HFB calculation with the Gogny-D1S interaction for the normal deformed nuclei in the rare-earth region. The Coulomb antipairing effect is too strong in the exact treatment [33]. However, the proton pairing correlation is important for the nuclear rotational motion. Although the proton pairing correlation may be recovered by applying the particle number projection [34], it is much more time consuming. Thus, we apply the Slater approximation since it is the simplest way to obtain the reasonable proton pairing correlation.

4.3 Three typical examples

In this section, we apply the multi-cranked configuration mixing to three examples; the ground-state band of the rare-earth nucleus ^{164}Er, the ground-state band of the unstable nucleus ^{40}Mg and the superdeformed band of the nucleus ^{152}Dy. We mainly show the results calculated by using the set of the almost equidistant cranking frequencies with $N^{\rm osc}_{\rm max} = 12$. To investigate the dependence of the chosen set of the cranking frequencies, calculations using the randomly chosen set of the cranking frequencies are

also performed. In these calculations, we use $N_{\rm max}^{\rm osc} = 8$ or 10 since the configuration mixing calculations require heavy numerical effort.

The λ-pole deformation parameter of the calculated mean-field is given by

$$\beta_\lambda \equiv \frac{4\pi}{3} \frac{\left\langle \sum_{i=1}^{A} (r^\lambda Y_{\lambda 0})_i \right\rangle}{A\,\bar{R}^\lambda}, \qquad \text{with} \quad \bar{R} = \sqrt{\frac{5}{3A}\left\langle \sum_{i=1}^{A} r_i^2 \right\rangle}, \tag{4.7}$$

and the average pairing gap is defined as [35]

$$\bar{\Delta} \equiv \frac{-\sum_{a>b} \Delta_{ab}\kappa_{ab}^*}{\sum_{a>b} \kappa_{ab}^*}, \qquad \text{with} \quad \Delta_{ab} = \sum_{c>d} \bar{v}_{ab,cd}\,\kappa_{cd}, \tag{4.8}$$

where the quantity κ_{ab} is the abnormal density matrix (the pairing tensor) and Δ_{ab} is the matrix element of the pairing potential with the anti-symmetrized matrix element $\bar{v}_{ab,cd}$ of the two-body interaction in Sec. 2.1.

4.3.1 Ground-state band of ^{164}Er

First example is the ground-state band of the nucleus ^{164}Er, where the high-spin states up to $I^\pi = 22^+$ are measured [36]. We use the oscillator basis with $N_{\rm osc}^{\rm max} = 12$. The calculated mean-field parameters by the non-cranked ($\omega_{\rm rot} = 0$) HFB are $\beta_2 = 0.311$ for the quadrupole deformation, which roughly agrees with the experimentally deduced value [37], and $\bar{\Delta} = 0.874$ and 0.906 MeV for the average neutron and proton pairing gaps, respectively, which are about 10%–13% smaller than the even-odd mass differences.

Fig. 4.1 shows the energy spectra calculated by the angular momentum projection from the non-cranked state and cranked state with $\hbar\omega_{\rm rot} = 0.01$ MeV in comparison with the experimental data. The value of the norm cut-off is taken to be 10^{-11}. The energy gain of the 0^+ ground state by the projection from the HFB state is 2.97 MeV. The excitation energies by the projection from the non-cranked HFB state systematically overestimate the experimental data. On the other hand, in the projection calculation from the cranked HFB state with the small cranking frequency much better agreement with the experimental data is obtained; the moment of inertia become larger by a factor of about two by including the time-odd components coming from the small cranking frequency. This result clearly shows the importance of the time-odd components for the angular momentum projection calculation, as also shown in Chap. 3. The calculated rotational states from the cranked state with $\hbar\omega_{\rm rot} = 0.01$ MeV considerably overestimate the experimental data at higher spin, $I \geq 16$ although they slightly underestimate the experimental data at lower spin, $I \leq 12$. This indicates that the calculated inertia does not reproduce the behavior of experimental inertia, which increases as a function of spin. The projection calculation from one

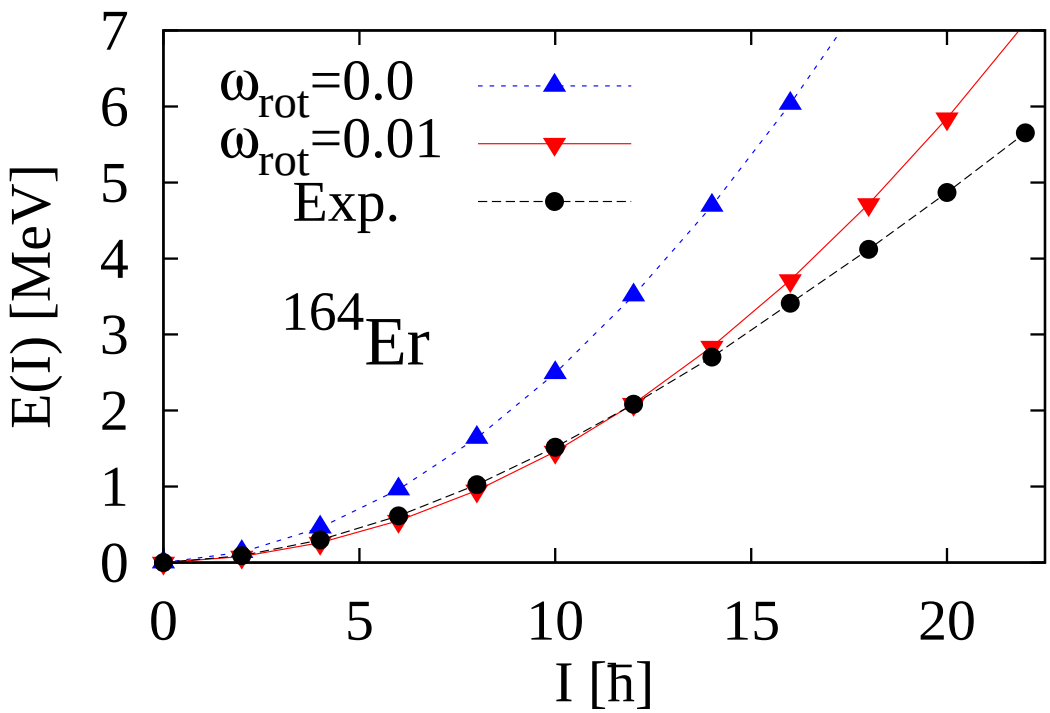

Figure 4.1: Energy spectra of the ground-state band of ^{164}Er calculated by the projections from the non-cranked HFB state ("$\omega_{\rm rot} = 0.0$") and from the cranked HFB state with $\hbar\omega_{\rm rot} = 0.01$ MeV ("$\omega_{\rm rot} = 0.01$"). Experimental data ("Exp.") are also included. The energy of the 0^+ state is taken as the energy origin in each spectrum.

intrinsic state is not satisfactory for describing the spectrum from the low-spin states up to the high-spin states. Thus, in order to obtain the reliable results for high-spin states, the improvement by the multi-cranked configuration mixing is necessary.

The calculated energy spectra by the projected multi-cranked configuration mixing and by the projection from one cranked state with $\hbar\omega_{\rm rot} = 0.01$ MeV are shown in Fig. 4.2 in comparison with the experimental data. The reference rotational energy $I(I+1)\hbar^2/(2\mathcal{J})$ with $\mathcal{J} = 40$ [$\hbar^2$/MeV] is subtracted in order to compare with the experimental data in detail. A set of five almost equidistant cranking frequencies, $(\hbar\omega_{\rm rot}^{(n)},\ n = 1:5) = (0.01,\ 0.05,\ 0.10,\ 0.15,\ 0.20)$ MeV, is adopted for the configuration mixing calculation. The calculated excitation energies by the projected multi-cranked configuration mixing well correspond the behavior of the experimental data although the calculated values slightly underestimate the experimental data. The energy difference is less than less than 130 keV in the whole spin range, $0 \leq I \leq 22$. Comparing the result of the projection calculation from one cranked state, the agreement with the experimental data is much better at higher spin, $I \geq 14$.

In order to display the effect of the configuration mixing, the five energy spectra calculated by the projection from one cranked state with the five different cranking frequencies are shown in Fig. 4.3. The result with configuration mixing is also included. The reference rotational energy is subtracted, as in the same way as in Fig. 4.2. The

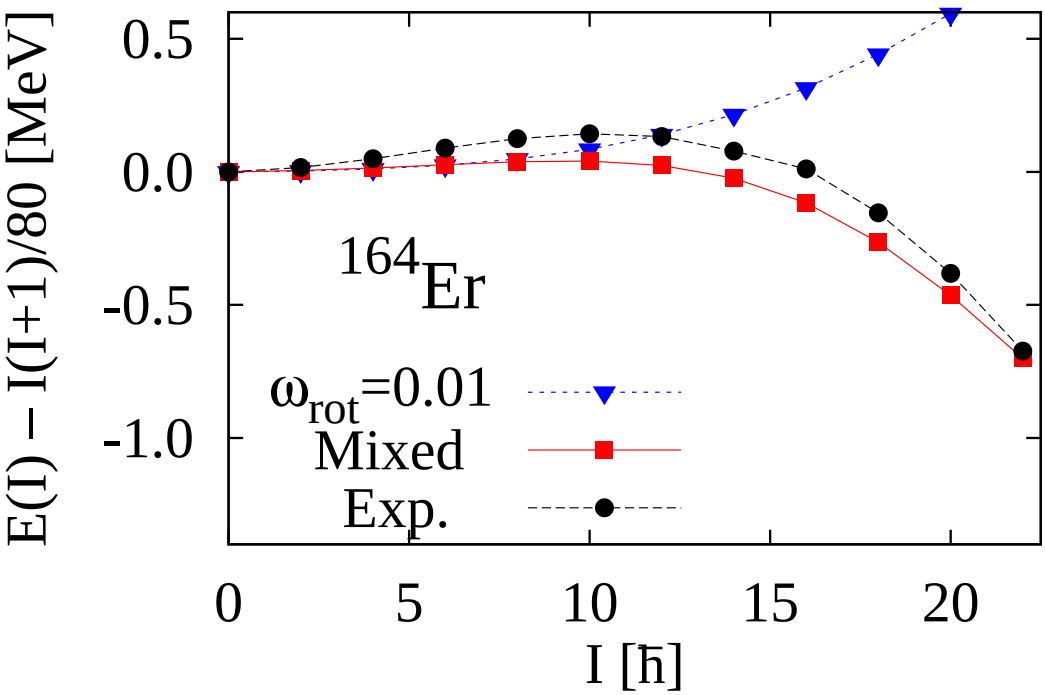

Figure 4.2: Energy spectra subtracting the reference rotational energy, $I(I+1)/80$ MeV, for ^{164}Er. The excitation energies calculated by the projected multi-cranked configuration mixing ("Mixed") and by the simple projection from one cranked state with $\hbar\omega_{\rm rot} = 0.01$ MeV are plotted. Experimental data are also included. The energy of the 0^+ state is taken as the energy origin in each spectrum.

energy origin refers to the 0^+ energy obtained by the configuration mixing calculation. The energy gain of the 0^+ state by the projected configuration mixing from the result with the non-cranked HFB state is about 0.83 MeV and the total energy gain by the projected configuration mixing from the HFB energy is 3.81 MeV. The absolute energies calculated by projected configuration mixing are smaller than the values by the projection from one cranked state in all the spin range. As long as only one intrinsic state is used for the projection calculation, the energy spectra are rather similar although the absolute 0^+ energy decreases with increasing the cranking frequency. While in the projection from only one intrinsic state only one $K^\pi = 0^+$ band is obtained, in the configuration mixing calculation not only the ground $K^\pi = 0^+$ band but also the excited $K^\pi = 0^+$ bands of the Hill-Wheeler equation are obtained. In this calculation, it is about 6 MeV higher than the ground-state energy. This is consistent to the fact that there is only one rotational band associated with the ground state.

The probabilities defined in Eq. (4.5) of the five configurations with $\hbar\omega_{\rm rot} = 0.01$, 0.05, 0.10, 0.15, 0.20 MeV are shown in Fig. 4.4. The probability distributions spread over five configurations for all the spin values, and the middle ($\hbar\omega_{\rm rot} = 0.10$ MeV) configuration always has the lowest value. The main difference for each spin is the probabilities of the first ($\hbar\omega_{\rm rot} = 0.01$ MeV) and final ($\hbar\omega_{\rm rot} = 0.20$ MeV) configurations. Thus, this probability distribution does not shows the expected behavior that

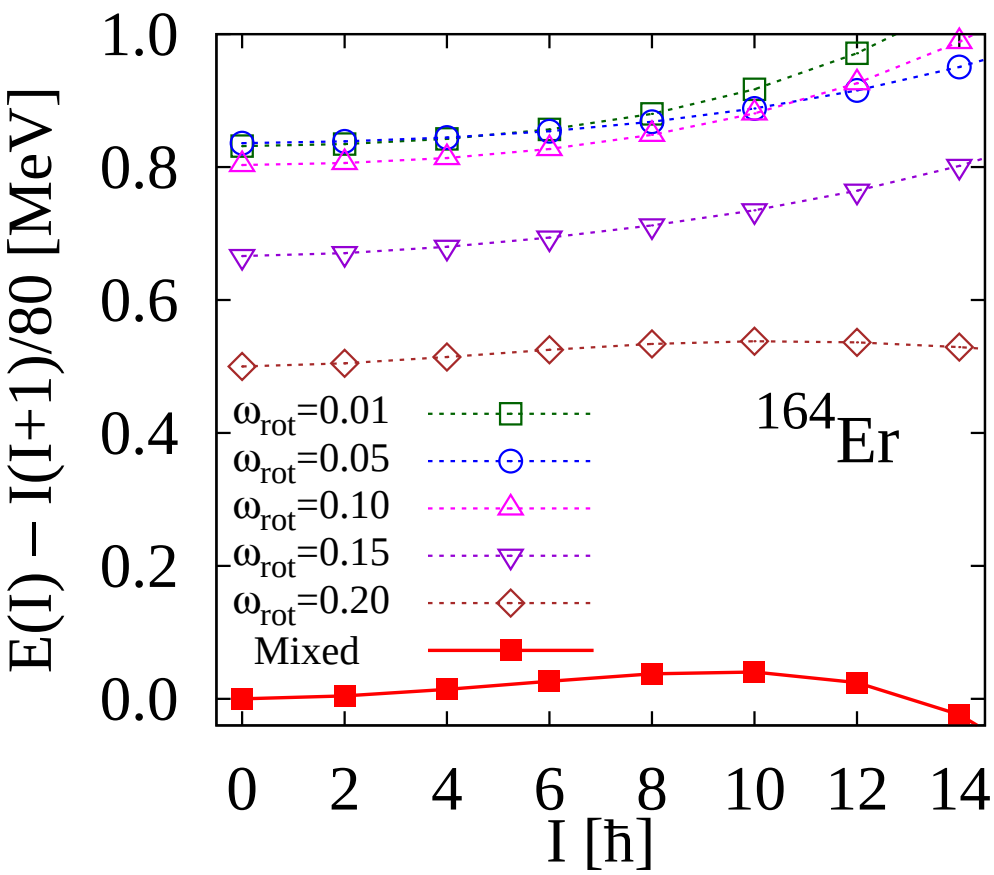

Figure 4.3: Energy spectra for ^{164}Er obtained by the simple projection calculations from one intrinsic HFB state with five different cranking frequencies. The reference rotational energy $I(I+1)/80$ is subtracted from the excitation energies. The result of the projected configuration mixing is also included. The absolute energy of the 0^+ state of the configuration mixing calculation is taken as the energy origin.

the distribution has the peak at $\langle\Phi_{\rm cr}|J_y|\Phi_{\rm cr}\rangle \approx I\hbar$, although the probability of the last (first) configuration increases (decreases) with increasing the spin. This indicates that the resultant state cannot be understood by simply increasing the cranking frequency for higher spin states. Since the absolute energies calculated by the projection from the last configuration are lower than those from other configurations, see Fig. 4.3, its probabilities are relatively large for all the spin $I = 0$, 4, 8, 12. Thus, it may be not satisfactory for this example to calculate the spin I state by the projection from one cranked state with the frequency $\omega_{\rm rot}$ that gives $\langle\Phi_{\rm cr}(\omega_{\rm rot})|J_y|\Phi_{\rm cr}(\omega_{\rm rot})\rangle \approx I\hbar$.

Fig. 4.5 shows the angular momenta as functions of the cranking frequency for various calculations in comparison with the experimental data. For the cranked HFB calculation the angular momentum is calculated by $I(\omega_{\rm rot})\,\hbar \equiv \langle\Phi_{\rm cr}(\omega_{\rm rot})|J_y|\Phi_{\rm cr}(\omega_{\rm rot})\rangle - \frac{1}{2}\hbar$ as a function of the cranking frequency $\omega_{\rm rot}$, where the subtraction of $\frac{1}{2}\hbar$ is the semi-classical correction, see e.g. Ref. [18]. For the projection calculations and the experimental data the rotational frequency is calculated by $\hbar\omega_{\rm rot}(I) \equiv (E(I+1)-E(I-1))/2$, where $E(I)$ is the energy at spin I. The slopes are different for each calculation, and

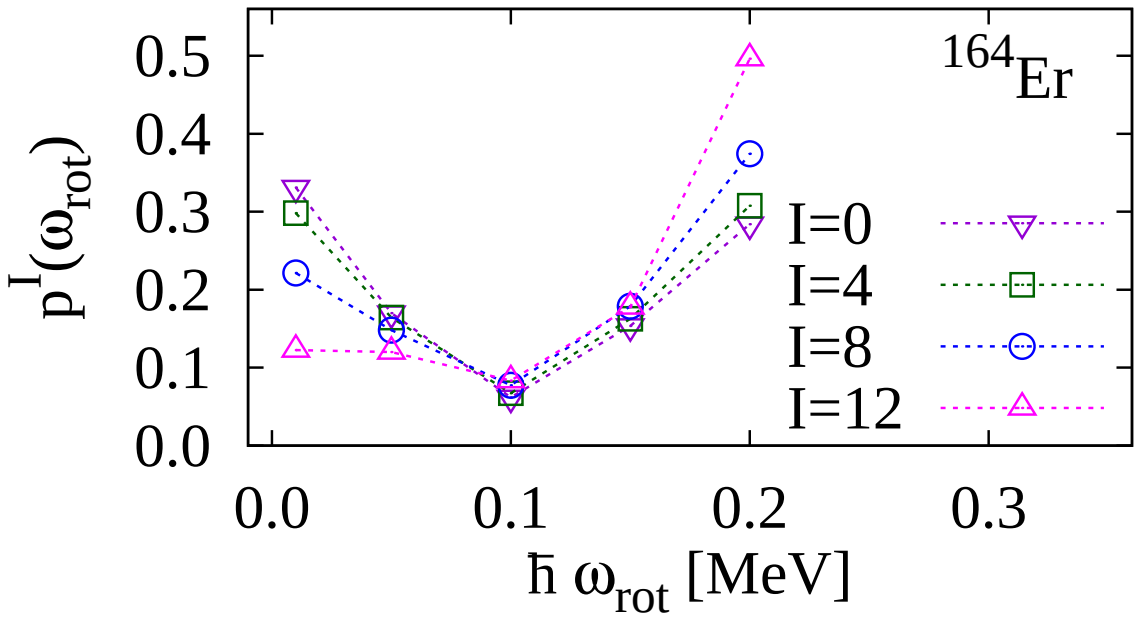

Figure 4.4: Probability distributions over the five HFB configurations with different frequencies for the spin I state of ^{164}Er obtained by the projected configuration mixing.

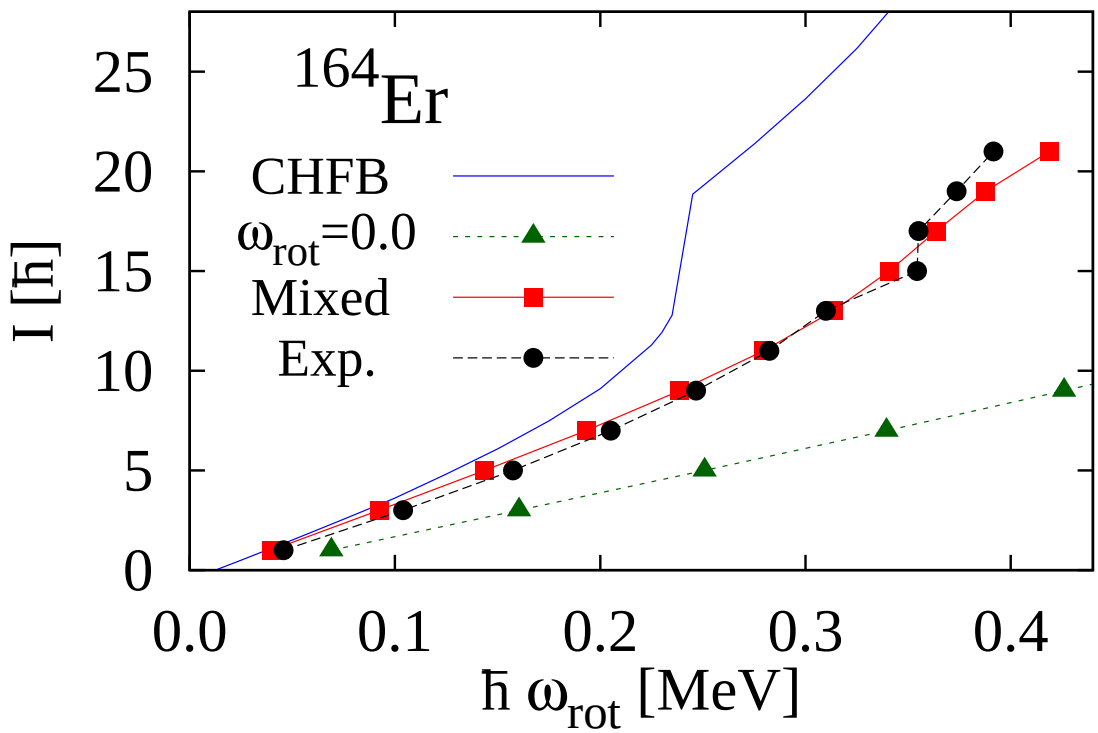

Figure 4.5: Angular momentum versus rotational frequency for ^{164}Er. The results of the cranked HFB ("CHFB"), of the projection from the non-cranked HFB state ("$\omega_{\rm rot} = 0.0$"), and of the projected configuration mixing ("Mixed") are plotted. The experimental data ("Exp.") are also included.

the result with the configuration mixing agrees well with the experimental data. The slope by the projection from the non-cranked ($\hbar\omega_{\rm rot} = 0.0$) HFB state is smaller than the experimental slope, and that of the cranked HFB is larger. In the cranked HFB calculation, the upbend of the angular momentum at $\hbar\omega_{\rm rot} \approx 0.25$ MeV is observed. This behavior is caused by the alignment of the lowest two quasi-neutron angular momentum vectors, which is experimentally observed in the crossing of the ground-state band (g-band) and the so-called Stockholm band (s-band). The effect of this band crossing on the g-band appears in the experimental data at $I = 15$ in Fig. 4.5 as an irregularity of the rotational band. Thus, the cranked HFB state with $\hbar\omega_{\rm rot} \lesssim 0.25$ MeV corresponds the intrinsic state of the g-band, and therefore the cranked states with $\hbar\omega_{\rm rot} \leq 0.20$ MeV is used for this projected configuration mixing calculation. Since, in our projection calculation the effect of the band crossing is not included, the calculated slopes are smooth. On the other hand, the cranked state with $\hbar\omega_{\rm rot} \gtrsim 0.25$ MeV corresponds to the intrinsic state of the s-band. The s-band calculated by the projected configuration mixing using these configurations will be discussed in Sec. 4.4.2. It is noticed that although the cranked HFB state with $\hbar\omega_{\rm rot} = 0.2$ MeV corresponds to the $I \approx 10$ state, the result of the configuration mixing well reproduces the experimental data up to $I = 22$.

In the cranked HFB calculation, the mean-field parameters like the deformation parameters and the pairing gaps change as functions of the cranking frequency. For example, the quadrupole deformation parameter β_2 slightly increases up to $\hbar\omega_{\rm rot} \approx 0.2$ MeV and starts to decreases, although the total amount of change is less than 10% in the range of frequency shown in Fig. 4.5. Although the non-cranked HFB calculation gives the axially symmetric deformation, the triaxial deformation become slightly larger up to $\hbar\omega_{\rm rot} \approx 0.24$ MeV in the cranked HFB calculation. The average pairing gaps for both neutrons and protons gradually decrease due to the Coriolis anti-pairing effect, and the neutron pairing gap suddenly drops after the g-s band crossing because of the blocking effect.

Figs. 4.6 and 4.7 show the so-called first (or kinematic) moment of inertia $\mathcal{J}^{(1)}$ for various calculations and the experimental data. It is defined for the cranked HFB calculations by $\mathcal{J}^{(1)}(\omega_{\rm rot}) \equiv \langle\Phi_{\rm cr}(\omega_{\rm rot})|J_y|\Phi_{\rm cr}(\omega_{\rm rot})\rangle/\omega_{\rm rot}$, which is plotted as a function of $I\,\hbar = \langle\Phi_{\rm cr}(\omega_{\rm rot})|J_y|\Phi_{\rm cr}(\omega_{\rm rot})\rangle - \frac{1}{2}\hbar$, and for the projection calculations and the experimental data by $\mathcal{J}^{(1)}(I) \equiv (2I+1)\hbar^2/(E(I+1) - E(I-1))$. The calculated inertia by the simple projection from the non-cranked HFB state in Fig. 4.6 is almost constant as a function of spin and considerably underestimates the experimental data due to the fact that it does not include the time-odd components induced by the cranking model. The result of the cranked HFB overestimates the experimental inertia in the whole spin region although it increases as a function of spin, which corresponds to the experimental behavior. The increase of the calculated inertia by the cranked HFB method is mainly caused by the gradual reduction of the pairing gaps. The calculated inertia by the projected configuration mixing is slightly larger than the experimental value at the lowest spin, which may be due to the fact that the average

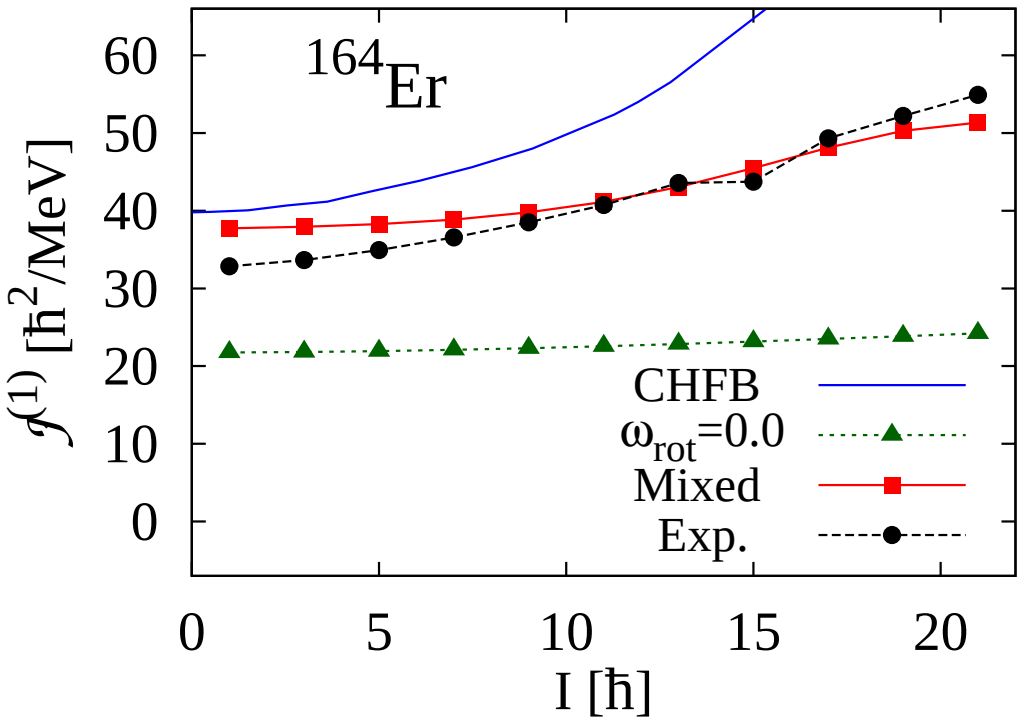

Figure 4.6: Moments of inertia versus spin value for ^{164}Er obtained by various calculations in comparison with the experimental data. The results of the projected configuration mixing ("Mixed"), of the simple projection from the non-cranked HFB state ("$\omega_{\rm rot} = 0.0$") and of the cranked HFB ("CHFB") are included.

pairing gaps both for neutrons and protons are about 10% smaller than the experimental even-odd mass-differences. Comparing with the result of the cranked HFB, the calculated inertia by the projected configuration mixing is in better agreement with the experimental data. Comparing the results of five simple projection calculations from one cranked state with the finite frequencies $\hbar\omega_{\rm rot} = 0.01, 0.15, 0.10, 0.15, 0.20$ MeV in Fig 4.7, rather similar inertias are obtained at lower spin region $I \leq 7$, and at lowest spin the calculated inertia by the projected configuration mixing is slightly smaller. All the calculated inertias by the simple projection from one cranked state are almost constant as functions of spin, and for the case of $\hbar\omega_{\rm rot} = 0.01, 0.15, 0.10, 0.15$, they even decrease. However, if the configuration mixing is performed, the moment of inertia increases as a function of spin, which corresponds to the experimental trend. Although all the results of the simple projection calculations from one cranked HFB state with different frequencies are similar and take a small value, $\mathcal{J}^{(1)} \approx 40$ [$\hbar^2$/MeV] at higher spin, that of the projected configuration mixing takes rather large value, $\mathcal{J}^{(1)} \approx 50$ at $I \approx 20$. Thus, the configuration mixing is important in order to obtain the increase of the moment of inertia for the projected result although the amount of increase of inertia is not enough compared with the experimental data. It is noted that in this calculations the Gogny interaction is employed and there are no adjustable parameters.

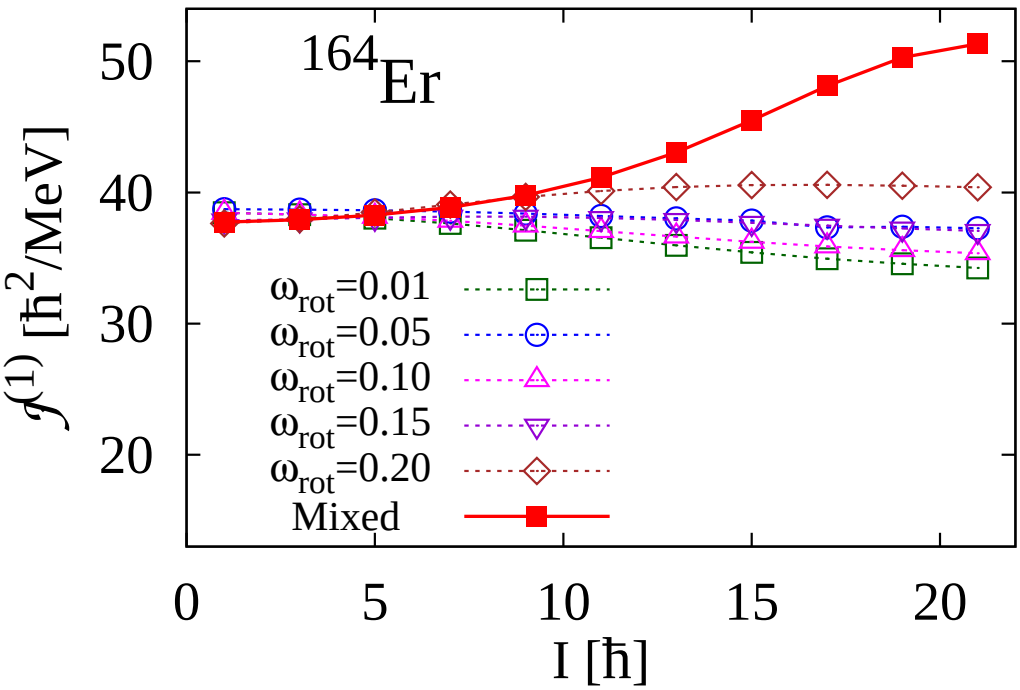

Figure 4.7: Moments of inertia versus spin value for ^{164}Er obtained by the simple projection calculations from one cranked state with five different cranking frequencies. The result of the projected configuration mixing is also included.

We have shown the results with a set of almost equidistant cranking frequencies for the configuration mixing. However, we can choose other sets of the cranking frequencies. Therefore, in order to see the dependence of the result of the configuration mixing on the set of the cranking frequencies, the results with the randomly chosen sets of the cranking frequencies are shown in Fig. 4.8. In this calculations the smaller model space with $N_{\rm osc}^{\rm max} = 10$ is used to reduce the numerical task. Various randomly chosen sets of cranking frequencies are generated with the conditions that the frequency satisfies, $0 < \hbar\omega_{\rm rot} < 0.20$ MeV, to avoid the effect of the g-s band crossing, and the difference of two nearest frequencies satisfies, $\hbar\Delta\omega_{\rm rot} > 0.02$ MeV, to avoid too large overlap between the two associated HFB states, which may cause the vanishing norm problem of the GCM procedure [14]. The values of norm cut-off are adjusted in the range $10^{-8} - 10^{-10}$. The results with three, four, and five configurations for randomly chosen frequencies are shown in the first, second, and third rows, respectively, in Fig. 4.8. We have performed eight trial calculations in each case. The left panels show the average values and the standard deviations of the calculated moments of inertia for the eight trials, which are represented by points and error bars, respectively. All the inertias calculated with each randomly chosen set of the cranking frequencies are plotted in the middle panels. The randomly chosen sets of the cranking frequencies applied in each trial are displayed in the right panels. As clearly seen in the left panels of Fig. 4.8, the standard deviations become small with increase of the number of configuration used in the configuration mixing, even though

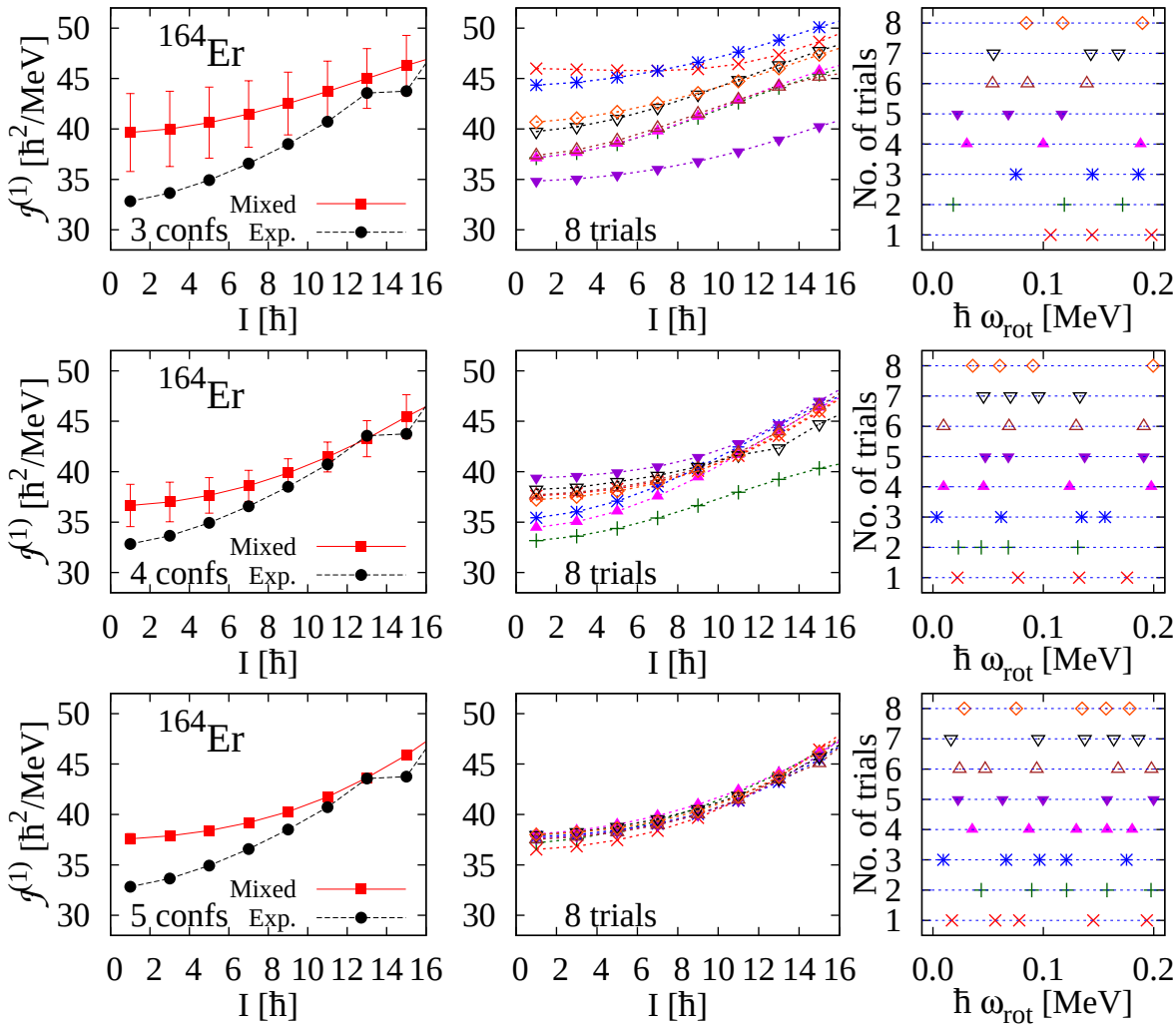

Figure 4.8: Moments of inertia for ^{164}Er calculated by the projected configuration mixing with randomly chosen sets of the cranking frequencies. The top, middle and bottom panels represent the results with three, four, and five configurations for the projected configuration mixing, respectively. In the left panels, the average values and standard deviation of the calculated inertia for the eight trials are plotted, which are represented by points and error bars, respectively. All the inertias calculated with each randomly chosen set of the cranking frequencies are plotted in the middle panels. The randomly chosen sets of cranking frequencies applied in each trial are displayed in the right panels. The smaller model space $N_{\rm osc}^{\rm max} = 10$ is used in this calculations.

the generated sets of the cranking frequencies are rather different. In fact, if we use the set of five configurations, the standard deviations are within the size of symbols. When the number of configurations is three, not only the standard deviations are large but also the average values are considerably different with the value calculated with larger numbers of configurations. Comparing the calculated inertias in each case of three configurations, not only the absolute values but also the spin-dependence are rather difference; e.g., at $I \leq 9$, calculated inertia with the first set of the configura-

tions (red dotted line) is almost constant as a function of spin. In the case of four configurations, although at higher spin similar absolute values are obtained except for the forth case (green dotted line), at low spin the large difference remains. Thus, the result of multi-cranked configuration mixing with the equidistant set of five cranking frequencies gives the almost unique result. The inertia calculated by the projected multi-cranked configuration mixing does not essentially depend on the chosen set of the cranking frequencies if the number of configurations is sufficient. The difference between the converged result of mixing calculation with five configurations in the left-bottom panel of Fig. 4.8 and the equidistant result in Fig. 4.6 is small, which is coming from the difference of model space $N_{\rm osc}^{\rm max} = 10$ and 12. Therefore, in Sec. 4.4.1 we systematically investigate the ground-state rotational bands in rare-earth region with smaller model space, $N_{\rm osc}^{\rm max} = 10$.

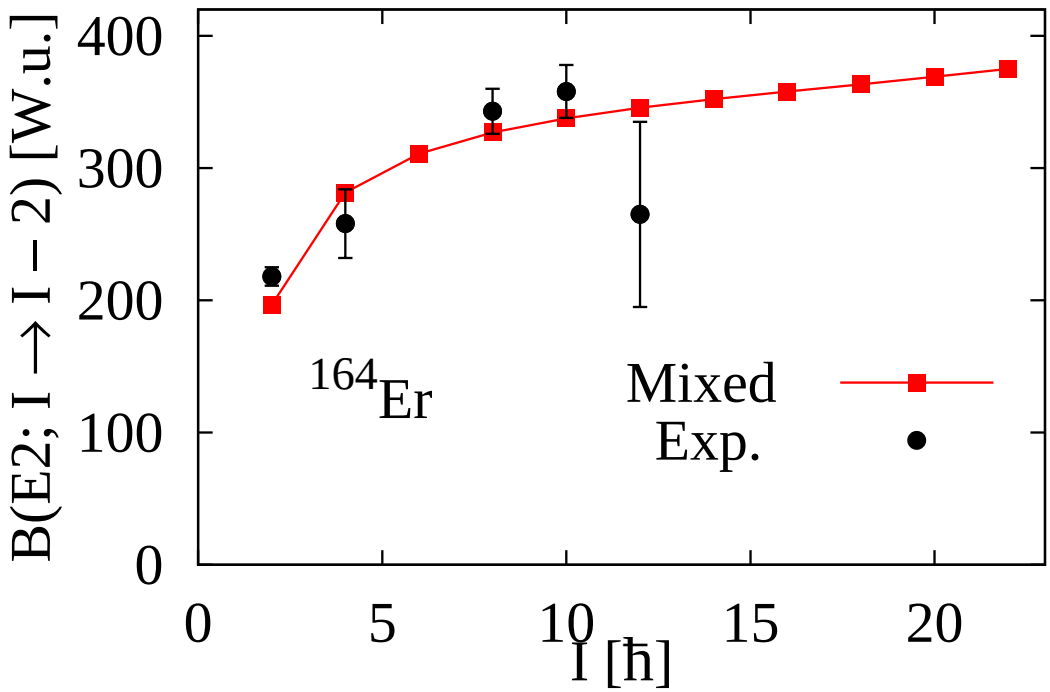

Figure 4.9: In-band $B(E2; I \to I-2)$ values in Weisskopf units (W.u.) for ^{164}Er calculated by the projected configuration mixing. The experimental data are taken from Ref. [38].

The so-called Weisskopf units $B_{\rm W}$ are often used as units for the electromagnetic transition probabilities. They represent the contribution of one particle to electromagnetic transition probabilities, and for the electric λ-pole case, $B(E\lambda)$, they are given by

$$B_{\rm W} = \frac{(1.2)^{2\lambda}}{4\pi}\left(\frac{3}{\lambda+3}\right)^2 A^{2\lambda/3}[e^2{\rm fm}^{2\lambda}]. \tag{4.9}$$

The calculated in-band $B(E2)$ transition probabilities by the projected configuration mixing in comparison with the experimental data are shown in Fig. 4.9. The calculated $B(E2)$ values well reproduce the experimental data. The quadrupole moment is most

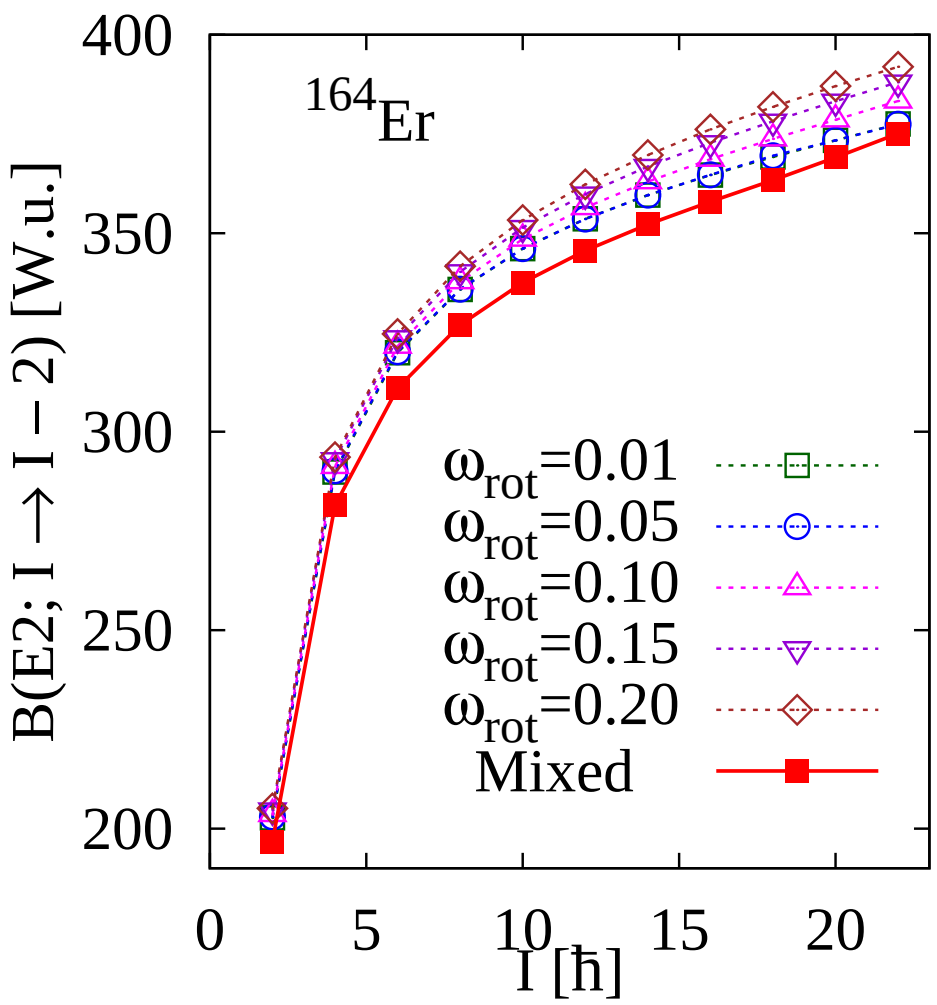

Figure 4.10: In-band $B(E2; I \to I-2)$ values in Weisskopf units (W.u.) for ^{164}Er calculated by the simple projection from one cranked state with five different cranking frequencies. The result of configuration mixing is also included for comparison.

important to obtain the correct $B(E2)$ values. In fact, the experimental quadrupole moment is usually extracted from the observed $B(E2)$ values by assuming the rotor model, see Eq. (2.52). Therefore, the nice agreement with the experimental data is natural since the calculated quadrupole deformation parameter by the non-cranked HFB method roughly corresponds to the experimentally deduced value. The calculated $B(E2)$ values by the simple projection from one cranked state with five different frequencies in comparison with the result of the configuration mixing are shown in Fig. 4.10. The $B(E2)$ values become larger when increasing the cranking frequency $\omega_{\rm rot}$, which well reflects the change of the quadrupole deformation parameter as a function of the cranking frequency. In fact, as mentioned before, the quadrupole deformation parameter β_2 slightly increase up to $\hbar\omega_{\rm rot} \approx 0.20$ MeV in our cranked HFB calculation. However, the calculated $B(E2)$ values by the projected configuration mixing are smaller than those of the projection calculation from one cranked state. This seems to be due to the fact that the probabilities in Fig 4.4 spread over five

configurations, which causes the reduction of the expectation values of $E2$ operator by decoherence.

4.3.2 Ground-state band of ^{40}Mg

We apply the projected configuration mixing to a nucleus ^{40}Mg as an example of the unstable nuclei. It has been predicted that this nucleus has the deformed shape even though the neutron number $N = 28$ is a magic number [39]. As shown in Chap. 3, also in our mean-field calculation the deformed ground state has been found for the nucleus ^{40}Mg. Its deformed minimum is relatively deep, and the effect of the configuration mixing with respect to the quadrupole deformation is small. This nucleus is also predicted to be the drip-line nucleus in Ref. [39]. We use the oscillator basis with $N_{\rm osc}^{\rm max} = 12$, which is larger than the model space used in Chap. 3 ($N_{\rm osc}^{\rm max} = 8$). The calculated quadrupole deformation parameter by the non-cranked ($\omega_{\rm rot} = 0$) HFB is $\beta_2 = 0.334$, and both of the neutron and proton pairing correlations vanish.

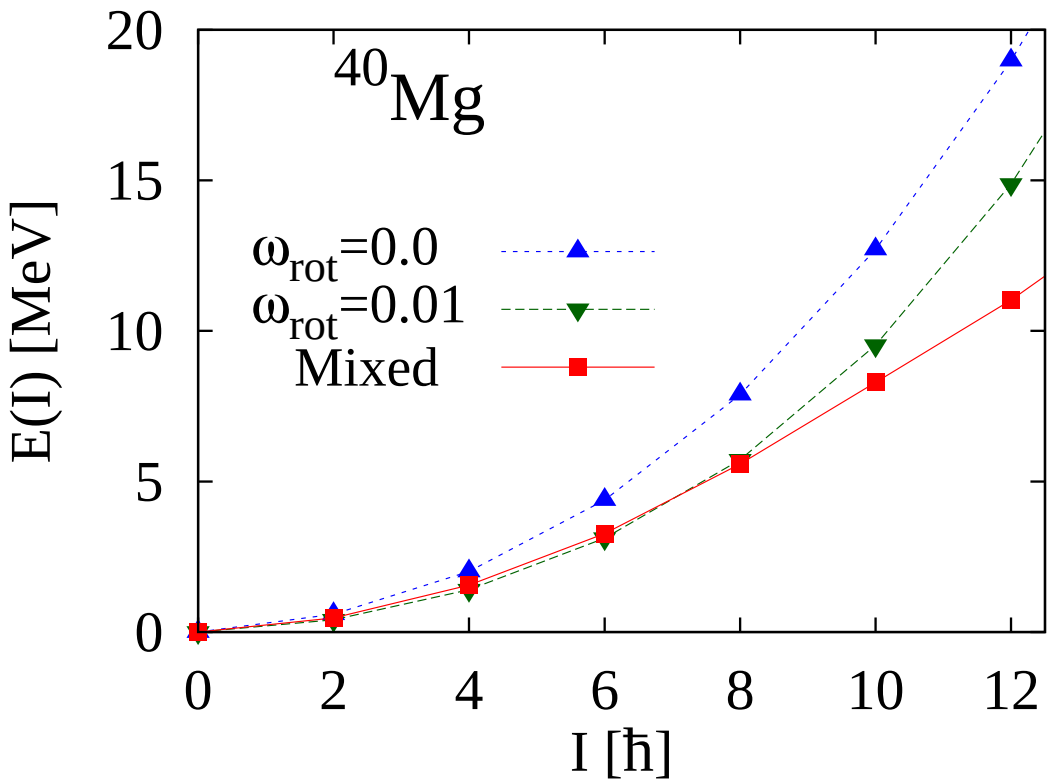

Figure 4.11: Energy spectra of the ground-state band of ^{40}Mg. The three results of the projections from the non-cranked HFB state ("$\omega_{\rm rot} = 0.0$") and from the cranked HFB state with $\hbar\omega_{\rm rot} = 0.01$ MeV ("$\omega_{\rm rot} = 0.01$") and of the projected configuration mixing ("Mixed") are included.

The calculated energy spectra by the simple projection from the non-cranked HFB state and from the cranked HFB state with $\hbar\omega_{\rm rot} = 0.01$ and by the projected configuration mixing are shown in Fig. 4.11. There is no experimental data available yet

for this nucleus. A set of four equidistant cranking frequencies, ($\hbar\omega_{\rm rot}^{(n)}$, $n = 1:4$) =(0.01, 0.34, 0.67, 1.00) MeV, is adopted for the projected multi-cranked configuration mixing calculation. The value of norm cut-off is taken to be 10^{-8}. The energy gain of the 0^+ ground state by the configuration mixing is 3.47 MeV. The excitation energies by the projection from the non-cranked HFB state are systematically larger than that of the projection from the cranked HFB state with $\hbar\omega_{\rm rot} = 0.01$ MeV, which is due to the fact that the time-odd components induced by the cranking method with the small cranking frequency are included into the wave functions. The large difference between the energy spectra calculated by the projected configuration mixing and by the projection from one cranked state with $\hbar\omega_{\rm rot} = 0.01$ MeV is seen at higher spin, $I \geq 10$.

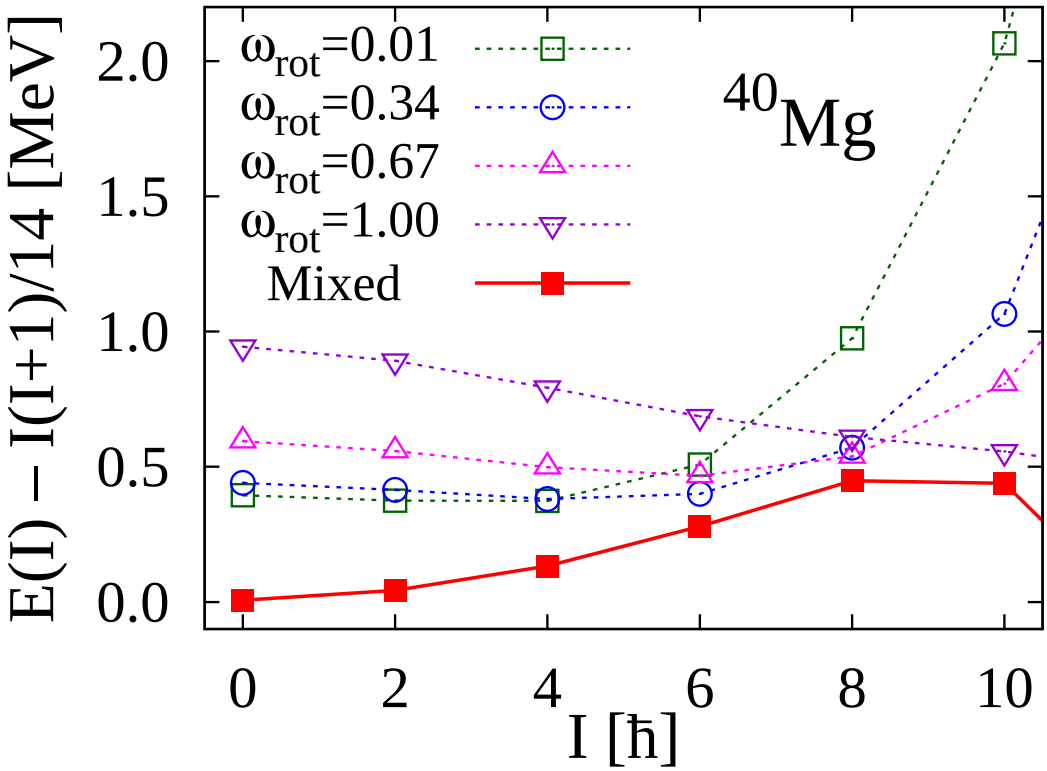

Figure 4.12: Energy spectra for ^{40}Mg obtained by the simple projection calculations from one intrinsic HFB state with four different cranking frequencies. The reference rotational energy $I(I+1)/14$ is subtracted from the excitation energies. The result of the projected configuration mixing is also included. The absolute energy of the 0^+ state calculated the configuration mixing is taken as the energy origin.

In order to see the effect of the configuration mixing, the four energy spectra calculated by the projections from one cranked state with the four different cranking frequencies are shown in Fig. 4.12. The result with configuration mixing is also included. The reference rotational energy $I(I+1)/(2\mathcal{J})$ with $\mathcal{J} = 7$ [$\hbar^2$/MeV] is subtracted. The energy origin is chosen to be the 0^+ energy of the projected configuration mixing. The absolute 0^+ energies calculated by the simple projection from one

cranked state become larger when increasing the cranking frequency, which is opposite to the case of ^{164}Er. It is noticed that in the simple projection from one cranked state the projected states with the lowest energy change from the state with lower frequency to the state with higher frequency with increasing the spin. The absolute energies of the projected configuration mixing are larger than those of the simple projection from one intrinsic state. The excited $K^\pi = 0^+$ energy of the projected configuration mixing is about 2.7 MeV higher than the ground-state energy, which indicate that there is only one rotational band associated with the ground state.

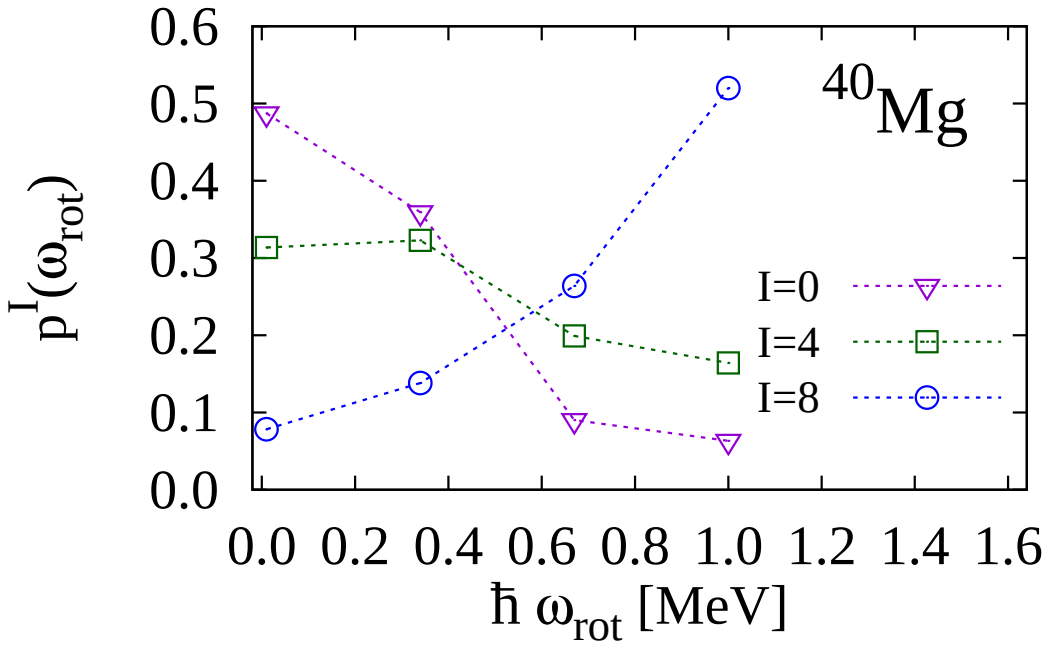

Figure 4.13: Probability distributions over the four HFB configurations for the spin I state of ^{40}Mg obtained by the projected configuration mixing

The probabilities defined in Eq. (4.5) over the four configurations with $\hbar\omega_{\rm rot} = 0.01, 0.34, 0.67, 1.00$ MeV are shown in Fig. 4.13. The behavior of the probability distributions seems to be what is expected; i.e., the peak of the distribution moves from the lower frequencies to the higher frequencies with increasing the spin. Fig. 4.14 shows the angular momenta as functions of the cranking frequency for various calculations. The slope of the result of the simple projection from the non-cranked HFB is smaller than the other three results. On the other hand, three slopes of the results of the projected configuration mixing, of the simple projection from one cranked state with $\hbar\omega_{\rm rot} = 0.01$ MeV and of the cranked HFB are rather similar at lower frequency, $\hbar\omega_{\rm rot} \lesssim 0.9$ MeV. Taking a closer look at the result of the cranked HFB, the gradual change of the slope can be seen at higher spin, $\hbar\omega_{\rm rot} \gtrsim 1.2$ MeV, which is caused by the gradual rotational alignment.

Figs. 4.15 and 4.16 show the moment of inertia $\mathcal{J}^{(1)}$ for various calculations. The calculated inertia by the simple projection from the non-cranked HFB state is smaller than the other results, which indicates that it is important to include the time-odd

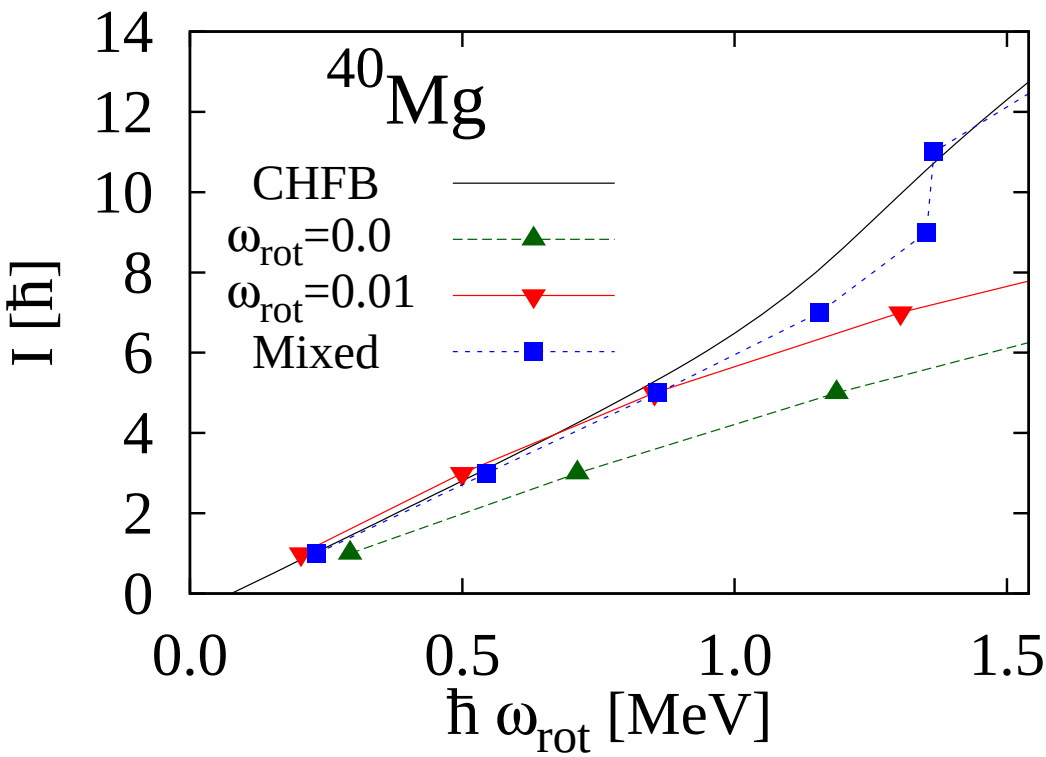

Figure 4.14: Angular momentum versus rotational frequency for ^{40}Mg. The results of the cranked HFB ("CHFB"), of the projection from the non-cranked HFB state ("$\omega_{\rm rot} = 0.0$"), and of the projected configuration mixing ("Mixed") are plotted.

components induced by the cranking procedure. As for the spin-dependence, the calculated inertias by the simple projections from one intrinsic state (including the non-cranked HFB state) decrease as functions of spin. In particular, the inertia with $\hbar\omega_{\rm rot} = 0.01$ MeV reduces about 40% at $I = 11$ compared with the one at $I = 1$. However, if the configuration mixing is performed, the realistic behavior of the moment of inertia are obtained: The calculated inertia by the projected configuration mixing is almost constant at lower spin, and increases at higher spin as a function of spin. It seems that the result of the configuration mixing is more reliable. For this nucleus, calculated inertias by the projected configuration mixing and by the cranked HFB are similar. In order to see the dependence of result of the configuration mixing on the set of the cranking frequencies, the results with the randomly chosen sets of the cranking frequencies are shown in Fig. 4.17. In this calculation we use the smaller model space with $N_{\rm osc}^{\rm max} = 8$ to reduce the numerical task. Various randomly chosen sets of cranking frequencies are generated with the conditions that the frequency satisfies, $0 < \hbar\omega_{\rm rot} < 1.0$ MeV, to avoid the effect of the gradual rotational alignment, and the difference of two nearest frequencies satisfies, $\hbar\Delta\omega_{\rm rot} > 0.1$ MeV, to avoid too large overlap between the two associated HFB states. The values of norm cut-off are adjusted in the range $10^{-8} - 10^{-10}$. The results with two and four configurations for randomly chosen frequencies are shown in the top and bottom panels, respectively, in

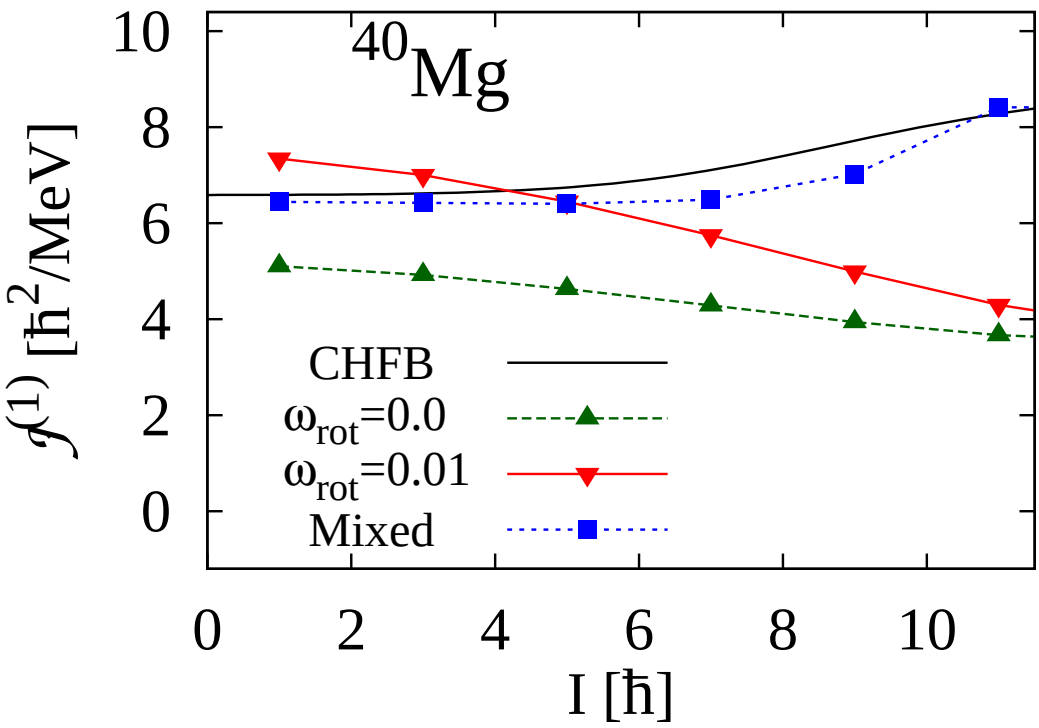

Figure 4.15: Moments of inertia versus spin value for ^{40}Mg obtained by various calculations. The results of the projected configuration mixing ("Mixed"), of the simple projection from the non-cranked HFB state ("$\omega_{\rm rot} = 0.0$") and from the cranked state with $\hbar\omega_{\rm rot} = 0.01$ MeV, and of the cranked HFB ("CHFB") are included.

Fig. 4.17. We have performed eight trial calculations in each case. The left panels show the average values and standard deviations of the calculated moments of inertia for the eight trials, which are represented by points and error bars, respectively. All the inertias calculated with each randomly chosen set of the cranking frequencies are plotted in the middle panels. The randomly chosen sets of cranking frequencies applied in each trial are displayed in the right panels. The standard deviations are smaller with increasing the number of configurations. In fact, the result of the four configuration mixing are rather similar for all the eight trials except for the result at the highest spin. Therefore, the inertia calculated by the projected multi-cranked configuration mixing does not essentially depend on the chosen sets of the cranking frequencies.

4.3.3 Superdeformed band of ^{152}Dy

The projected configuration mixing is applied to the superdeformed band of a nucleus ^{152}Dy. The high-spin superdeformed rotational band was first discovered in this nucleus [7], and the transitions between the superdeformed and the normal deformed states were also measured [40]. We use the oscillator basis with $N_{\rm osc}^{\rm max} = 12$. In the non-cranked HFB calculation, the axially symmetric superdeformed minimum is found

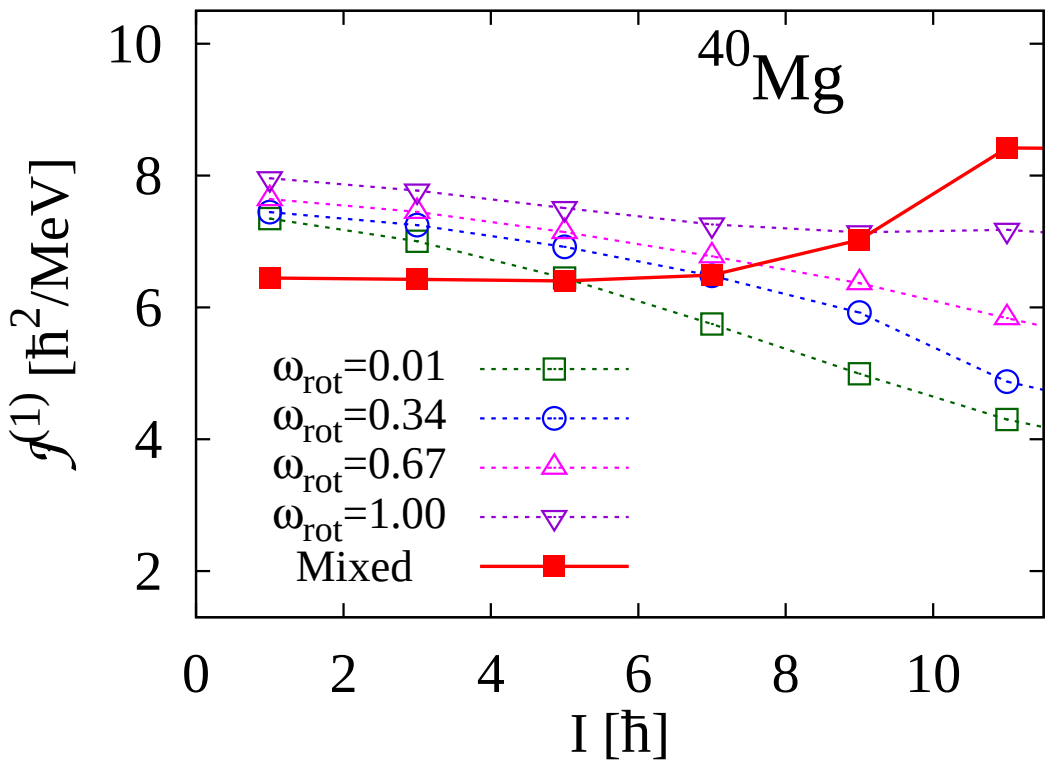

Figure 4.16: Moments of inertia versus spin value for ^{40}Mg obtained by the simple projection calculations from one intrinsic HFB state with four different cranking frequencies. The result of the projected configuration mixing is also included.

at the quadrupole deformation parameter $\beta_2 = 0.715$, where the neutron pairing correlation vanishes, and the proton pairing gap is very small, $\bar{\Delta} \approx 0.4$ MeV. For this nucleus, we perform the projection calculation without the pairing correlation for reducing of the numerical task. We need to obtain the very high-spin states like $I \approx 60$, and the projection calculation with the pairing correlation is much more time consuming [1]. The difference between the binding energies with and without the proton pairing correlation is less than 20 keV in the non-cranked HFB calculations. In the non-cranked HFB calculations, the quadrupole deformation parameter gradually decreases up to $\beta_2 = 0.699$ at $\hbar\omega_{\rm rot} = 0.7$ MeV. The quadrupole deformation parameter of our calculation slightly overestimates those of the Nilsson-Strutinsky and Woods-Saxon-Strutinsky calculation in Refs. [41, 42]. This is because the definition of the deformation parameters of our calculation is different from those of these references. The deformation parameters are defined from the shape of the average potential in these references. On the other hand, we define them from the density distribution, i.e. $\langle Q_{\lambda\mu}\rangle$ and $\langle r^2\rangle$.

In this calculation, a set of four equidistant cranking frequencies, ($\hbar\omega_{\rm rot}^{(n)}$, $n = 1:4$) =(0.01, 0.24, 0.47, 0.70) MeV, is adopted for the configuration mixing calculation. The value of norm cut-off is taken to be 10^{-9}. For the superdeformed state, the energy gain of the 0^+ state by the configuration mixing compared with the simple

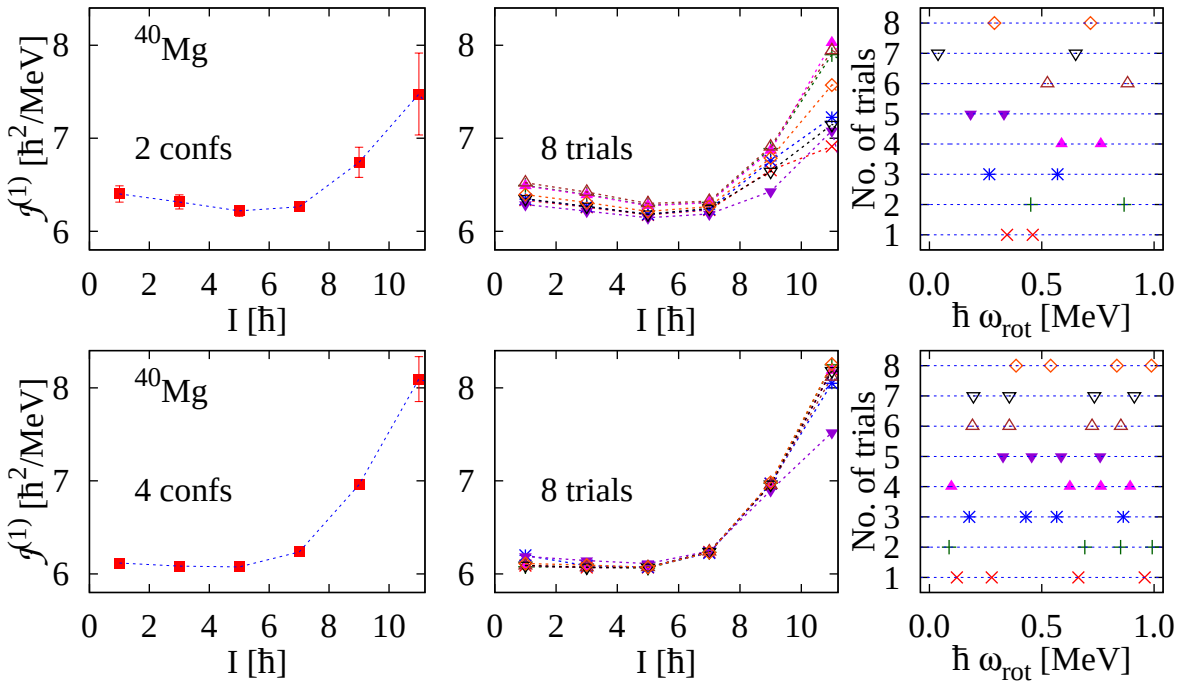

Figure 4.17: Moments of inertia for ^{40}Mg calculated by the projected configuration mixing with randomly chosen sets of the cranking frequencies. The top and bottom panels represent the results with two and four configurations for the projected configuration mixing, respectively. In the left panels, the average values and standard deviation of the calculated inertia for the eight trials are plotted, which are represented by points and error bars, respectively. All the inertias calculated with each randomly chosen set of the cranking frequencies are plotted in the middle panels. The randomly chosen sets of cranking frequencies applied in each trial are displayed in the right panels. The smaller model space $N_{\rm osc}^{\rm max} = 8$ is used in this calculation.

projection from the non-cranked HFB state is very small ($\Delta E \approx 30$ keV). The total energy gain by the projected configuration mixing from the HFB energy is 4.14 MeV. The excitation energy of the superdeformed 24^+ state calculated by the configuration mixing is 9.97 MeV, which well corresponds to the experimental value 10.644 MeV [40].

The first moments of inertia $\mathcal{J}^{(1)}$ are shown in Figs. 4.18, 4.19 and 4.20. The calculated inertias by the simple projections from the non-cranked HFB state in Figs. 4.18 are considerably smaller than the experimental data, which again indicates the importance of the time-odd components induced by the cranking model. The four calculated inertias by the simple projection from one cranked HFB state with four different frequencies in Fig. 4.19 considerably decrease with increasing the spin, which is rather different from the trend of the experimental data. In contrast to the case of ^{40}Mg, the amount of reduction as well as the absolute values of the moments of inertia becomes larger when increasing the cranking frequency. The result of the projected configuration mixing is almost constant, which is consistent with the experimental behavior

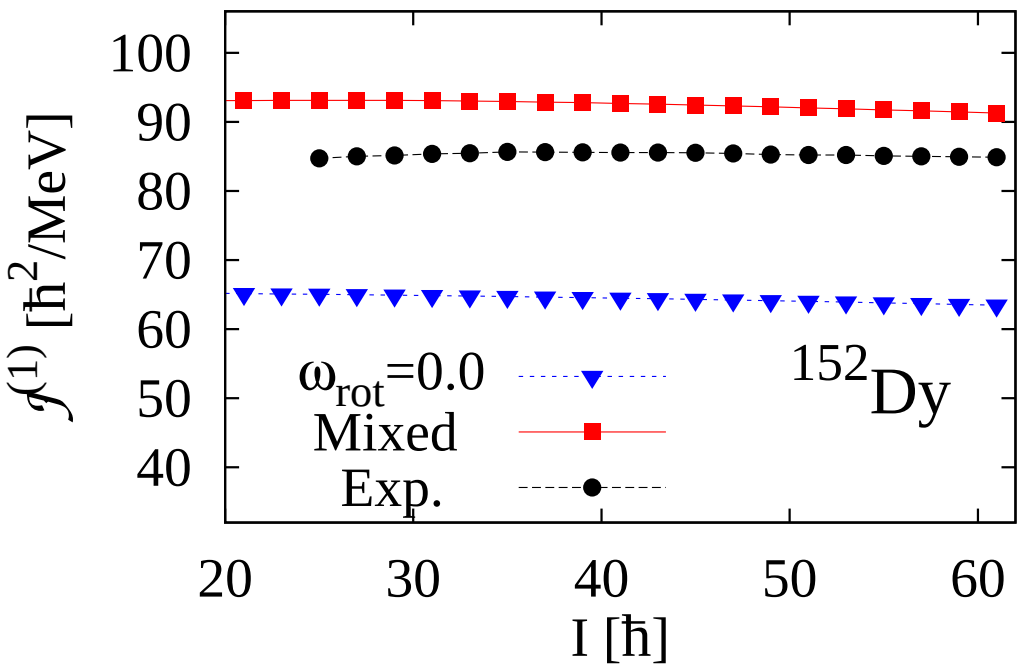

Figure 4.18: Moments of inertia versus spin value for ^{164}Er obtained by the two calculations in comparison with the experimental data. The results of the simple projection calculations from the non-cranked HFB state ("$\omega_{\rm rot} = 0.0$") and of the projected configuration mixing ("Mixed") are included. The experimental data ("Exp.") are also included.

although the absolute values are slightly higher than the experimental data. This fact clearly shows again that the configuration mixing is very important to obtain the correct behavior of the superdeformed rotational band by the angular momentum projection method. Comparing the calculated inertia by the projected configuration mixing with that of the cranked HFB in Fig. 4.20, the very similar results are obtained.

The probabilities defined in Eq. (4.5) over the four configurations with $\hbar\omega_{\rm rot} = 0.01, 0.24, 0.47, 0.70$ MeV are shown in Fig. 4.21. In contrast to the case of ^{164}Er, the sharp peaks of the distribution can be clearly seen. The behavior of the distributions is just what is expected; i.e., the peaks of the distributions appear at the cranking frequencies that give $\langle\Phi_{\rm cr}(\omega_{\rm rot})|J_y|\Phi_{\rm cr}(\omega_{\rm rot})\rangle \approx I\,\hbar$. This indicates that the superdeformed rotational band obtained by the projected configuration mixing can be understood semiclassically by the simple increasing the cranking frequency.

Figure 4.22 shows the so-called second (or dynamic) moment of inertia [43] obtained by the projected configuration mixing in comparison with the experimental data. It is defined by $\mathcal{J}^{(2)}(I) \equiv 4\hbar^2/(E(I+2) + E(I-2) - 2E(I))$. Since the spin-assignment is not necessary for the second moment of inertia, it has been often used for the study of the superdeformed bands. The calculated inertias slightly overestimate the experimental data. However, compared with the first moment of inertia in Fig. 4.18, the agreement with the experimental data is better.

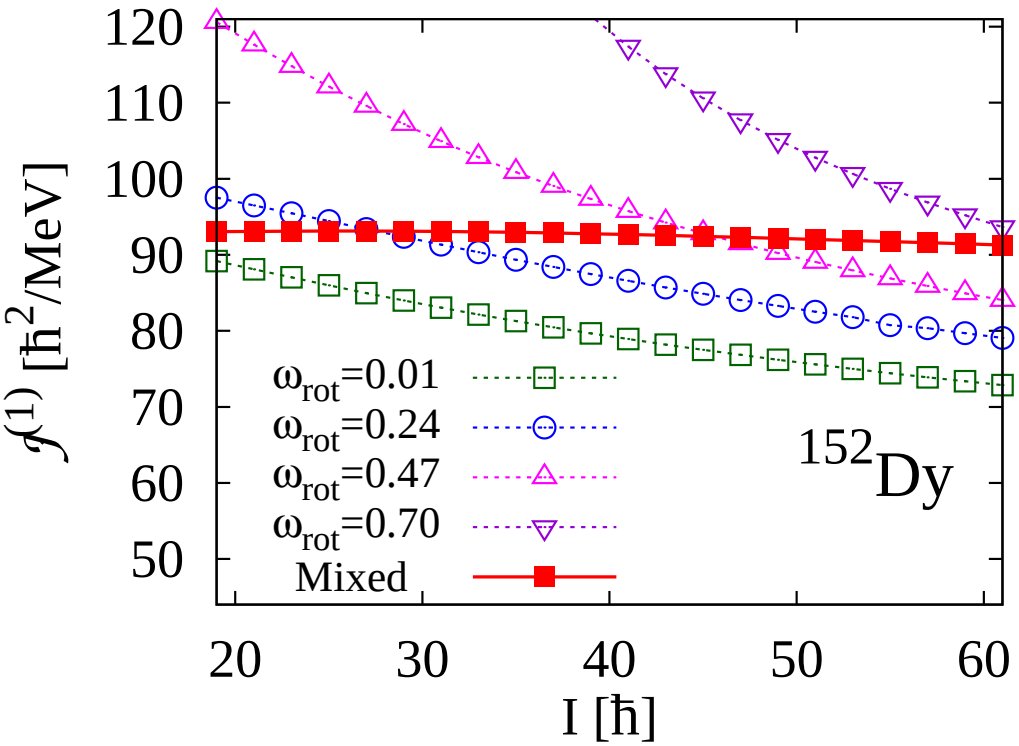

Figure 4.19: Moments of inertia versus spin value for ^{152}Dy obtained by the simple projection from one intrinsic HFB state with four values of the cranking frequencies, $\hbar\omega_{\rm rot}$ = 0.01, 0.24, 0.47, 0.70 MeV, respectively. The result of the projected configuration mixing is also included.

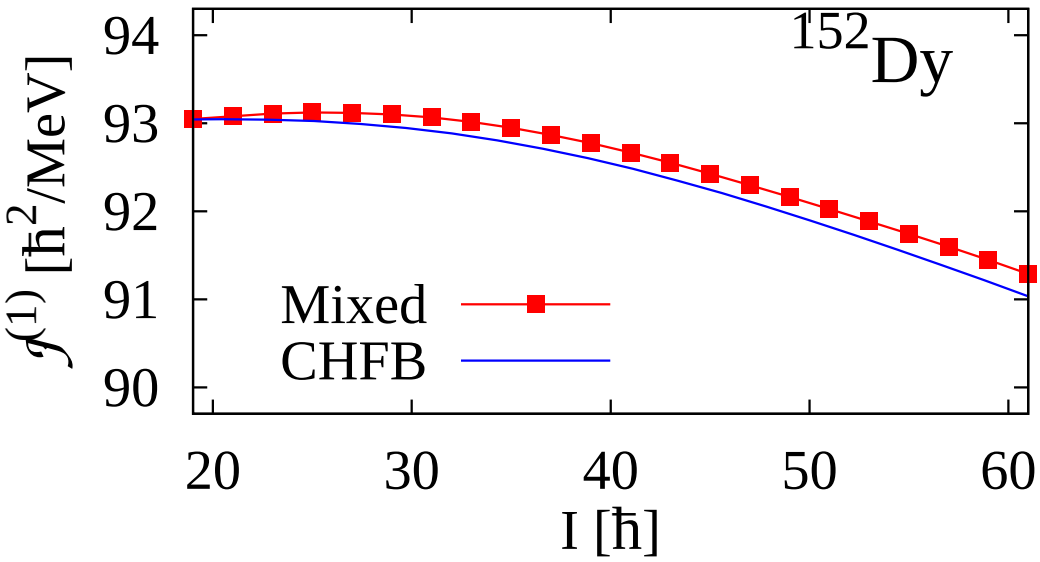

Figure 4.20: Moments of inertia versus spin value for ^{152}Dy obtained by the cranked HFB calculation ("CHFB"). The result of the projected configuration mixing ("Mixed") are also included for comparison.

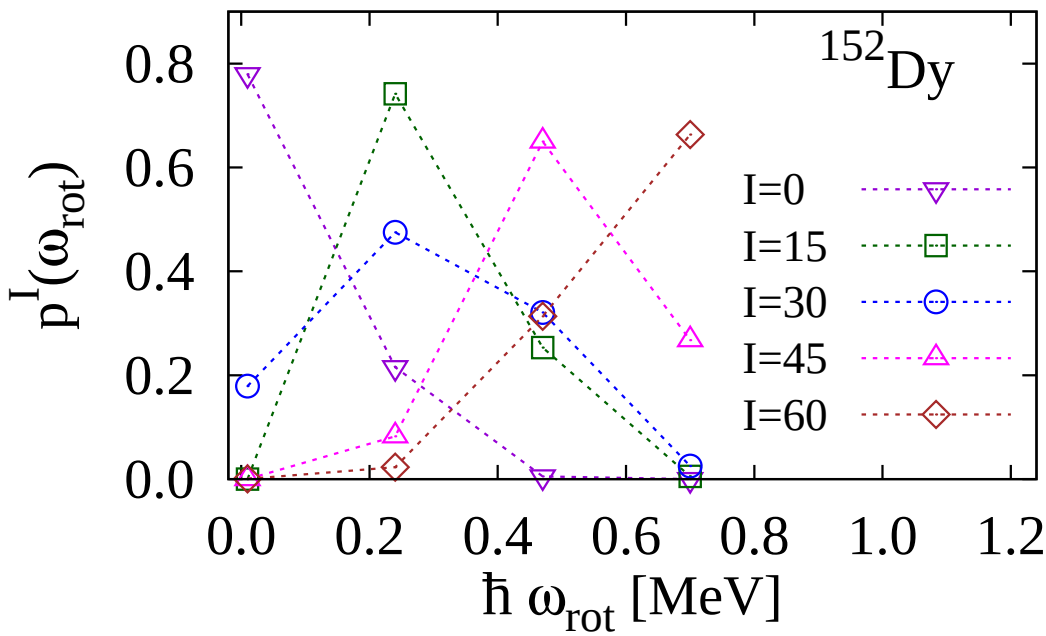

Figure 4.21: Probability distributions over the four HFB configurations for the spin I state of ^{152}Dy obtained by the projected configuration mixing.

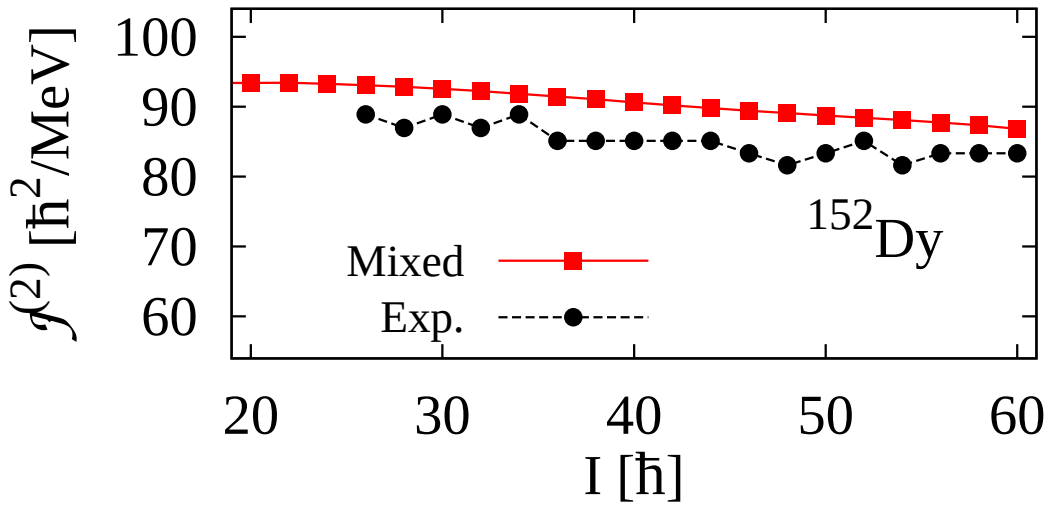

Figure 4.22: The second moment of inertia versus spin value for ^{152}Dy obtained by the projected configuration mixing ("Mixed") in comparison with the experimental data ("Exp.").

In order to see the dependence of result of the configuration mixing on the set of the cranking frequencies, also for this case the results with the randomly chosen sets of the cranking frequencies are shown in Fig. 4.23. In this calculation we use the smaller model space with $N_{\rm osc}^{\rm max} = 10$ to reduce the numerical task. Various randomly chosen sets of cranking frequencies are generated with the conditions that the frequency satisfies, $0 < \hbar\omega_{\rm rot} < 0.7$ MeV, and the difference of two nearest frequencies satisfies, $\hbar\Delta\omega_{\rm rot} > 0.07$ MeV, to avoid too large overlap between the two associated

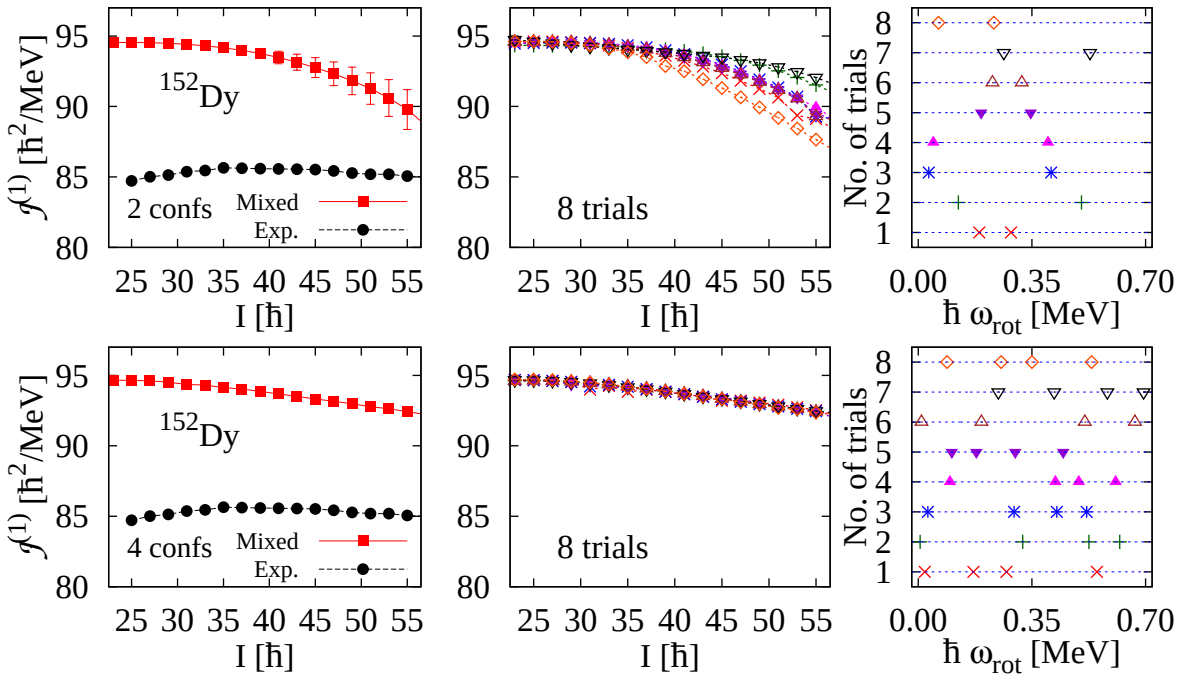

Figure 4.23: Moments of inertia for ^{152}Dy calculated by the projected configuration mixing with randomly chosen sets of the cranking frequencies. The top and bottom panels represent the results with two and four configurations for the projected configuration mixing, respectively. In the left panels, the average values and standard deviation of the calculated inertia for the eight trials are plotted, which are represented by points and error bars, respectively. All the inertias calculated with each randomly chosen set of the cranking frequencies are plotted in the middle panels. The randomly chosen sets of cranking frequencies applied in each trial are displayed in the right panels. The smaller model space $N_{\rm osc}^{\rm max} = 10$ is used in this calculation.

HFB states. The results with two and four configurations for randomly chosen frequencies are shown in the top and bottom panels, respectively, in Fig. 4.23. We have performed eight trial calculations in each case. The left panels show the average values and standard deviations of the calculated moments of inertia for the eight trials, which are represented by points and error bars, respectively. All the inertias calculated with each randomly chosen set of the cranking frequencies are plotted in the middle panels. The randomly chosen sets of cranking frequencies applied in each trial are displayed in the right panels. The standard deviations become smaller with increasing the number of the configurations. Surprisingly the rather converged inertias are already obtained in the mixing calculation with only two configurations. For the mixing with four configurations, converged results are obtained. This fact shows again that the results of the projected configuration mixing do not essentially depend on the chosen sets of the cranking frequencies, and the necessary number is rather small.

The calculated in-band $B(E2)$ transition probabilities by the projected configuration mixing in comparison with the experimental data are shown in Fig. 4.24. The

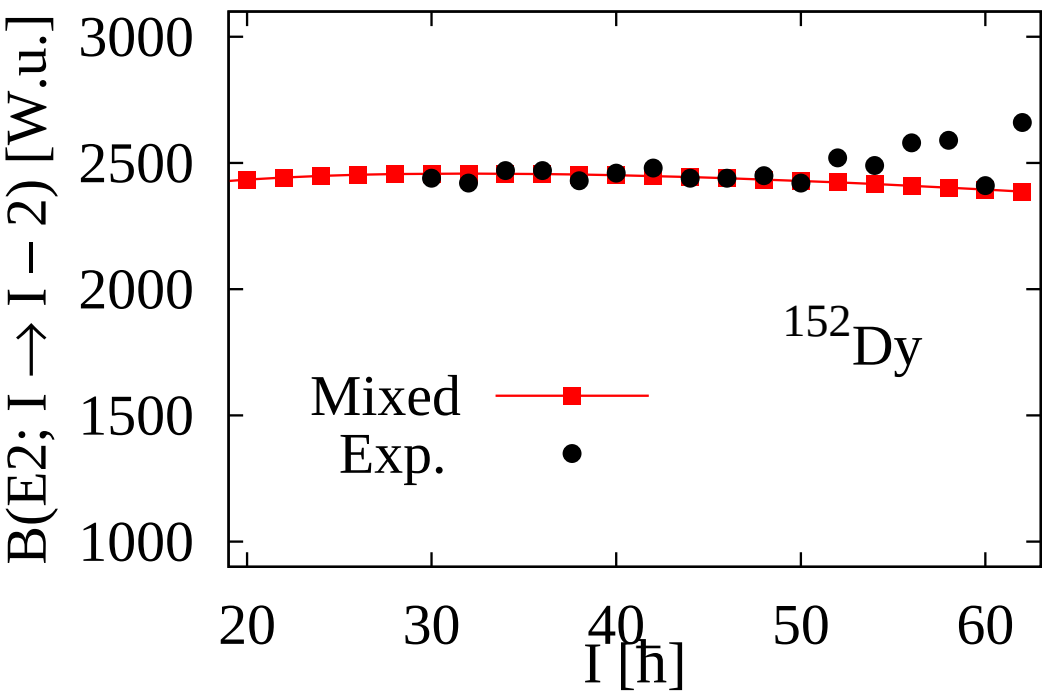

Figure 4.24: In-band $B(E2; I \to I-2)$ values in Weisskopf units (W.u.) for ^{152}Dy calculated by the projected configuration mixing. The experimental data are taken from Ref. [44].

$B(E2)$ transition probabilities for ^{152}Dy are very large reflecting the superdeformed shape. The calculated $B(E2)$ values well reproduce the experimental data except for the region at higher spin, $I > 50$. This indicate that calculated quadrupole moment by the cranked HFB well corresponds the experimentally deduced values at $I \leq 50$. The calculated $B(E2)$ values by the simple projections from one cranked state with five different frequencies in comparison with the result of the configuration mixing are shown in Fig. 4.25. The results of the simple projection from one cranked state well reflect the change of the quadrupole deformation parameter. In fact, in our cranked HFB calculation the quadrupole deformation parameter slightly decreases as a function of the cranking frequency in the region $0 < \hbar\omega_{\rm rot} < 0.7$ MeV, and therefore the $B(E2)$ values become smaller when increasing the cranking frequency. The result of the projected configuration mixing well reflects the change of the projection from one cranked state by the increase of the cranking frequency, as shown in the mixing probabilities in Fig. 4.21; while the calculated $B(E2)$ values by the projected configuration mixing are close to that of the projection from one cranked state with $\hbar\omega_{\rm rot} = 0.01$ or 0.24 MeV at lower spin, they are close to the result of the projection from one cranked state with $\hbar\omega_{\rm rot} = 1.00$ MeV at higher spin. Thus, the result of the projected configuration mixing includes the effect of the change of the deformation parameter with increasing the spin.

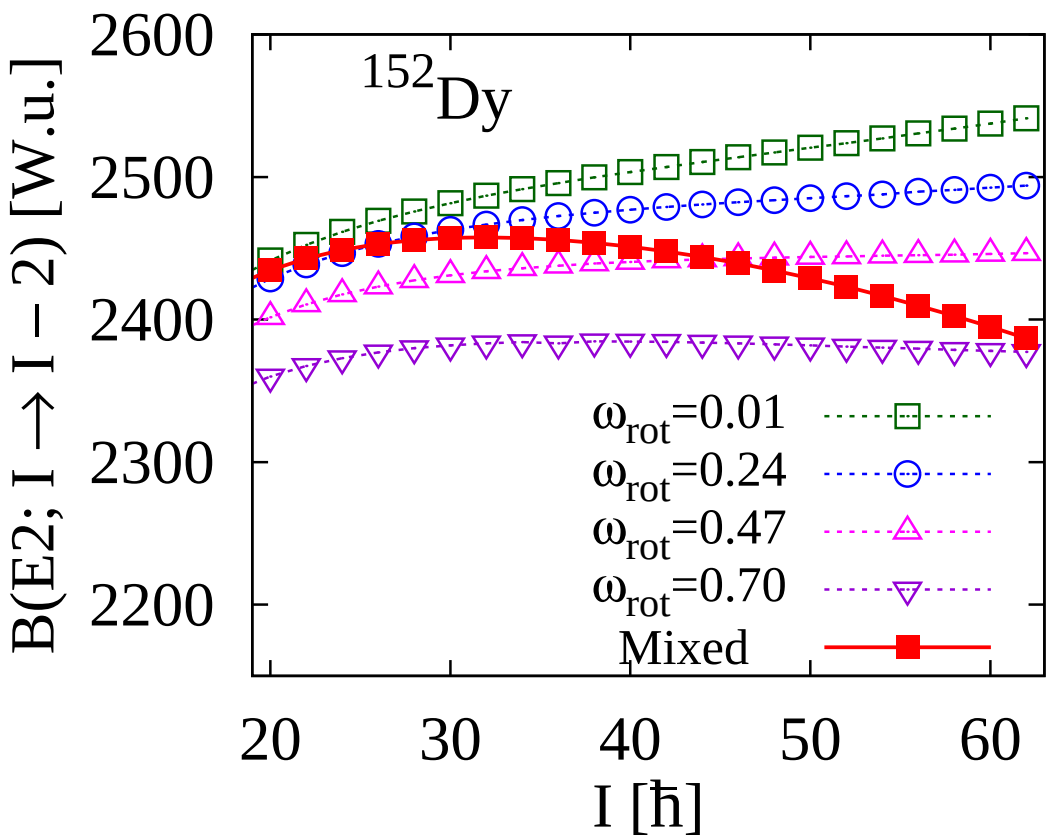

Figure 4.25: In-band $B(E2; I \to I-2)$ values in Weisskopf units (W.u.) for ^{164}Er calculated by the simple projection from one HFB state with four different cranking frequencies. The result of configuration mixing is also included for comparison.

4.4 Rotational bands in the rare-earth region

4.4.1 Ground-state bands in the rare-earth region

In this section, we systematically investigate the ground-state rotational bands of nuclei in the rare-earth region by the angular momentum projected multi-cranked configuration mixing. We use the oscillator basis with $N_{\rm osc}^{\rm max} = 10$. The deformation parameters and the pairing gaps calculated by the non-cranked HFB method for nuclei considered in this section are shown in Table 4.1 in comparison with the even-odd mass-differences. For all nuclei, the deformation parameters roughly correspond to the experimentally deduced values [6]. Most of the calculated pairing gaps underestimate the even-odd mass-differences. The pairing gaps for nuclei ^{156}Gd and ^{170}Yb are especially smaller than the even-odd mass-differences; for the nucleus ^{156}Gd the calculated neutron pairing gap is about 35% smaller, and for the nucleus ^{170}Yb both of the calculated neutron and proton pairing gaps are about 27% smaller. On the other hand, for nuclei ^{160}Gd, ^{162}Dy and ^{164}Dy, the calculated pairing gaps both for the neutrons and the protons relatively well correspond to the even-odd mass-differences, and their differences are less than 14%. The selected values of the norm cut-off and

		$\bar{\Delta}$ [MeV]		$\Delta_{\rm Exp}$ [MeV]	
nuclide	β_2	neutron	proton	neutron	proton
^{156}Gd	0.308	0.649	0.979	1.004	0.968
^{158}Gd	0.319	0.704	0.948	0.884	0.901
^{160}Gd	0.327	0.739	0.922	0.794	0.875
^{158}Dy	0.304	0.778	0.946	1.034	1.081
^{162}Dy	0.323	0.791	0.830	0.873	0.951
^{164}Dy	0.328	0.714	0.799	0.825	0.879
^{160}Er	0.281	0.838	1.027	1.112	1.207
^{162}Er	0.305	0.847	0.934	1.066	1.125
^{164}Yb	0.282	0.877	1.026	1.148	1.203
^{168}Yb	0.321	0.783	0.822	0.993	1.017
^{170}Yb	0.325	0.615	0.682	0.840	0.945

Table 4.1: Quadruple deformation parameters β_2 and pairing gaps $\bar{\Delta}$ calculated by the non-cranked ($\omega_{\rm rot} = 0$) HFB. Experimental even-odd mass differences $\Delta_{\rm Exp}$ are also included.

nuclide	norm cut-off	$\omega_{\rm rot}^{(n)}; n = 1:5$ [MeV]				
^{156}Gd	10^{-11}	0.01	0.05	0.10	0.15	0.20
^{158}Gd	10^{-11}	0.01	0.05	0.10	0.15	0.20
^{160}Gd	10^{-11}	0.01	0.05	0.10	0.15	0.20
^{158}Dy	10^{-12}	0.01	0.05	0.10	0.15	0.20
^{162}Dy	10^{-12}	0.01	0.05	0.10	0.15	0.20
^{164}Dy	10^{-11}	0.01	0.075	0.15	0.225	0.30
^{160}Er	10^{-11}	0.01	0.05	0.10	0.15	0.20
^{162}Er	10^{-12}	0.01	0.05	0.10	0.15	0.20
^{164}Yb	10^{-10}	0.01	0.05	0.10	0.15	0.20
^{168}Yb	10^{-11}	0.01	0.075	0.15	0.225	0.30
^{170}Yb	10^{-11}	0.01	0.05	0.10	0.15	0.20

Table 4.2: Norm cut-off and sets of cranking frequencies for the projection calculations.

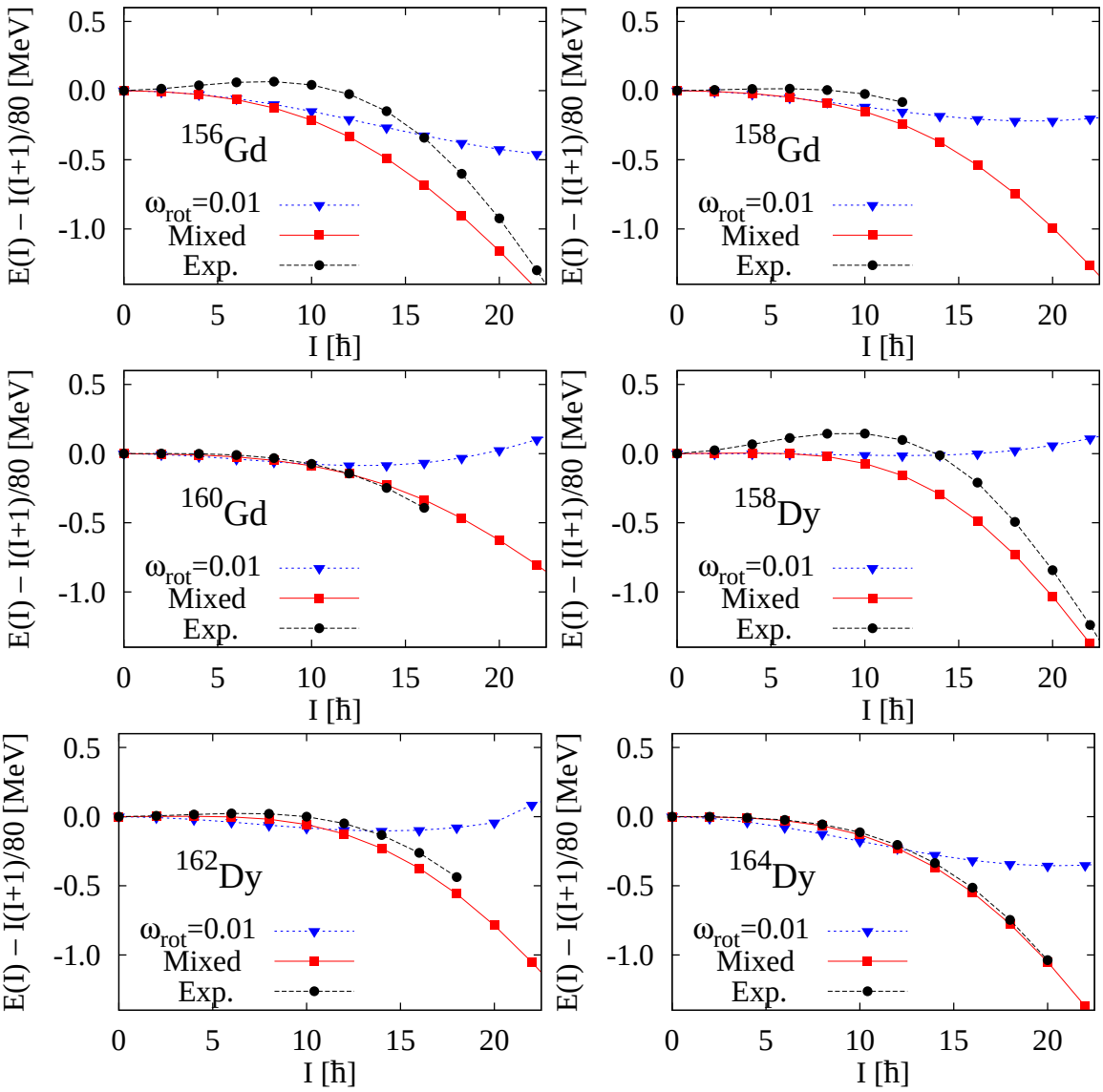

Figure 4.26: Excitation energy spectra subtracting the reference rotational energy, $I(I+1)/80$ MeV for the Gd and Dy isotopes. The results of the projection from one cranked HFB state with $\hbar\omega_{\rm rot} = 0.01$ MeV as well as those of the projected multi-cranked configuration mixing (the label "Mixed") are included in addition to the experimental data.

the chosen sets of the cranking frequencies are shown in Table 4.2. In the same way as the case of ^{164}Er, the sets of the almost equidistant cranking frequencies are chosen not to include the s-band configurations.

The calculated energy spectra by the projected configuration mixing in comparison with the experimental data are shown in Fig. 4.26 and 4.27. The results of the simple projections from one cranked state with the cranking frequency $\hbar\omega_{\rm rot} = 0.01$ MeV are also included. In the same way as in the case of ^{164}Er in Sec. 4.3.1, the reference rotational energy, $I(I+1)/80$ [MeV], is subtracted for each spectrum. For most of the cases, the energy spectra calculated by the projected configuration mixing are in

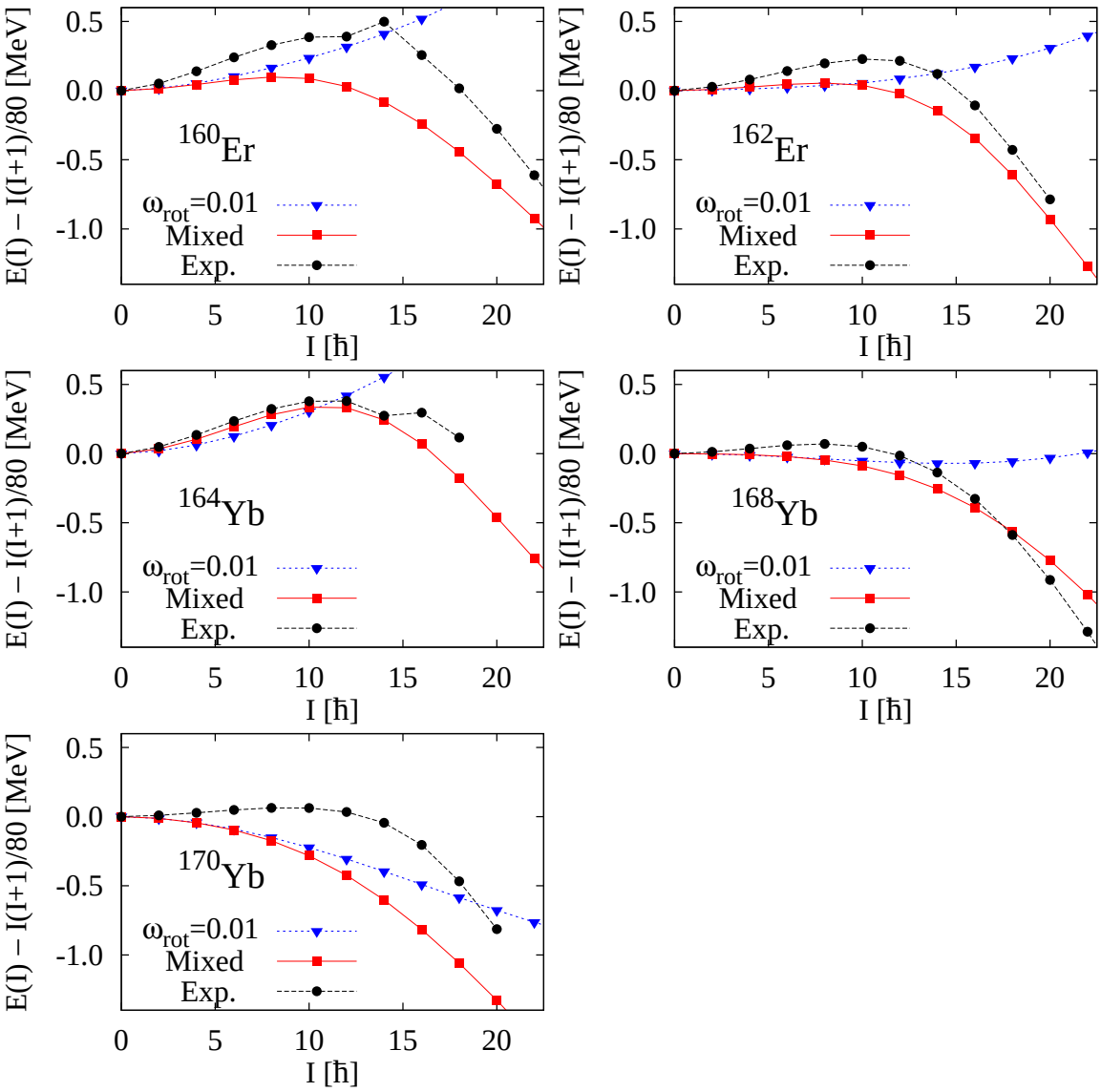

Figure 4.27: Excitation energy spectra subtracting the reference rotational energy, $I(I+1)/80$ MeV, for the Er and Yb isotopes. The results of the projection from one cranked HFB state with $\hbar\omega_{\rm rot} = 0.01$ MeV as well as those of the projected multi-cranked configuration mixing (the label "Mixed") are included in addition to the experimental data.

better agreements with the experimental data than that of the projection from one intrinsic state. At lower spins, some of the calculated energy spectra underestimate the experimental data. This is due to the fact that the calculated pairing gaps composing to these cases are smaller than the even-odd mass-differences. In particular, the results of the projected configuration mixing for the nuclei ^{160}Gd, ^{162}Dy, ^{164}Dy and ^{164}Yb well reproduce the experimental data.

The moments of inertia calculated by the projected configuration mixing and by the cranked HFB in comparison with the experimental data are shown in Fig. 4.28 and 4.29. The calculated inertias by the simple projections from one cranked state

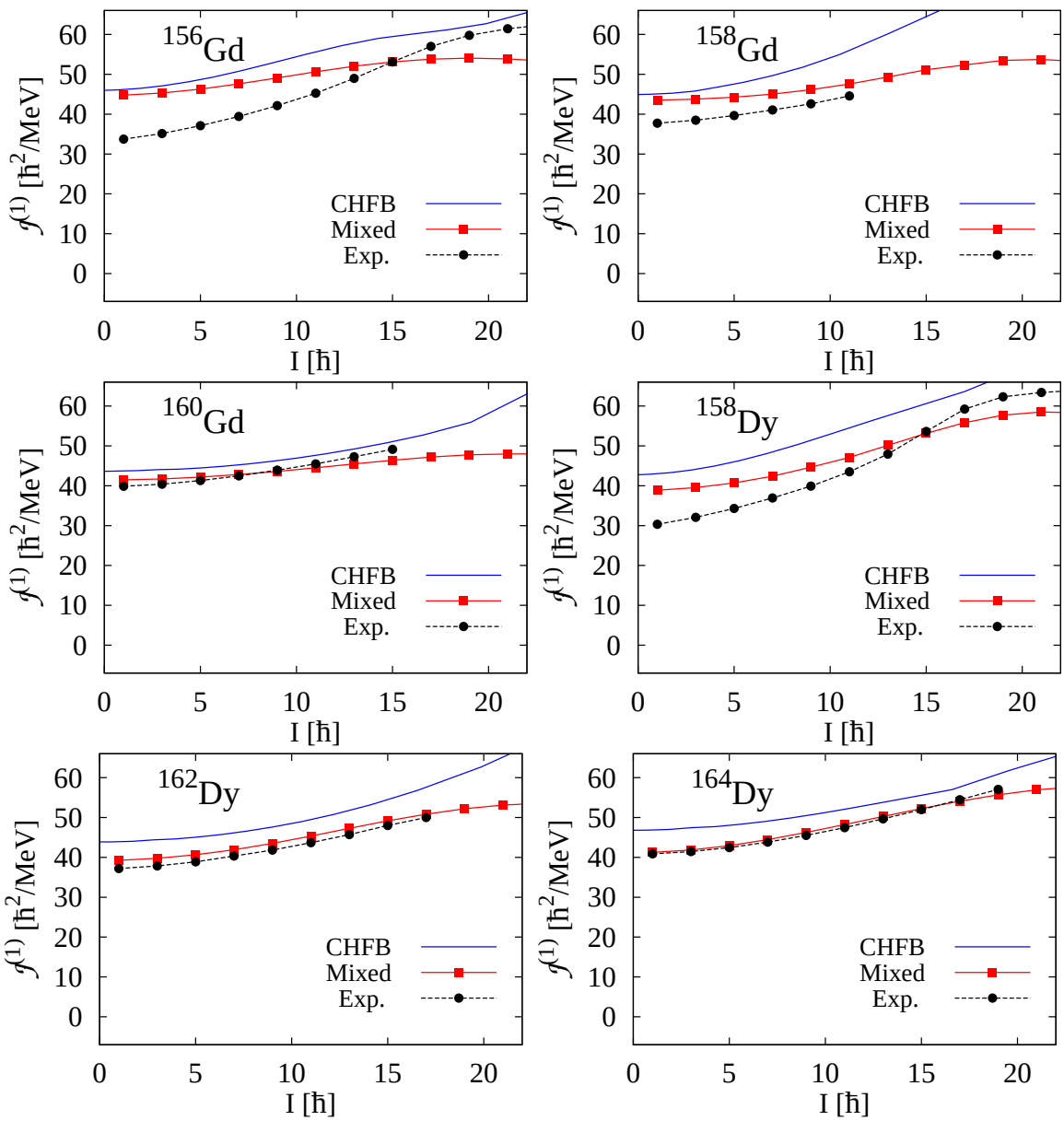

Figure 4.28: Moments of inertia versus spin value for the Gd and Dy isotopes obtained by various calculations in comparison with the experimental data.

with different frequencies are shown in Fig. 4.30 and 4.31. For some cases in the experimental data, see e.g. the inertia for ^{158}Dy in Fig. 4.28, increasing trend of the inertia as a function of spin stops at higher spin, which is caused by the strong interaction between the g-band and s-band. In order to obtain more reliable results for these rotational bands, the configuration mixing including the g-band and the s-band may be necessary. The irregularities of the rotational bands in the experimental data around $I \approx 15$ for ^{160}Er and ^{164}Yb in Fig. 4.29 are caused by the effect of g-s band crossing. The calculated inertias by the projected configuration mixing at the lowest spin overestimate the experimental data, which may be due to the fact that the calculated pairing gaps by the non-cranked HFB for nuclei considered underestimate the

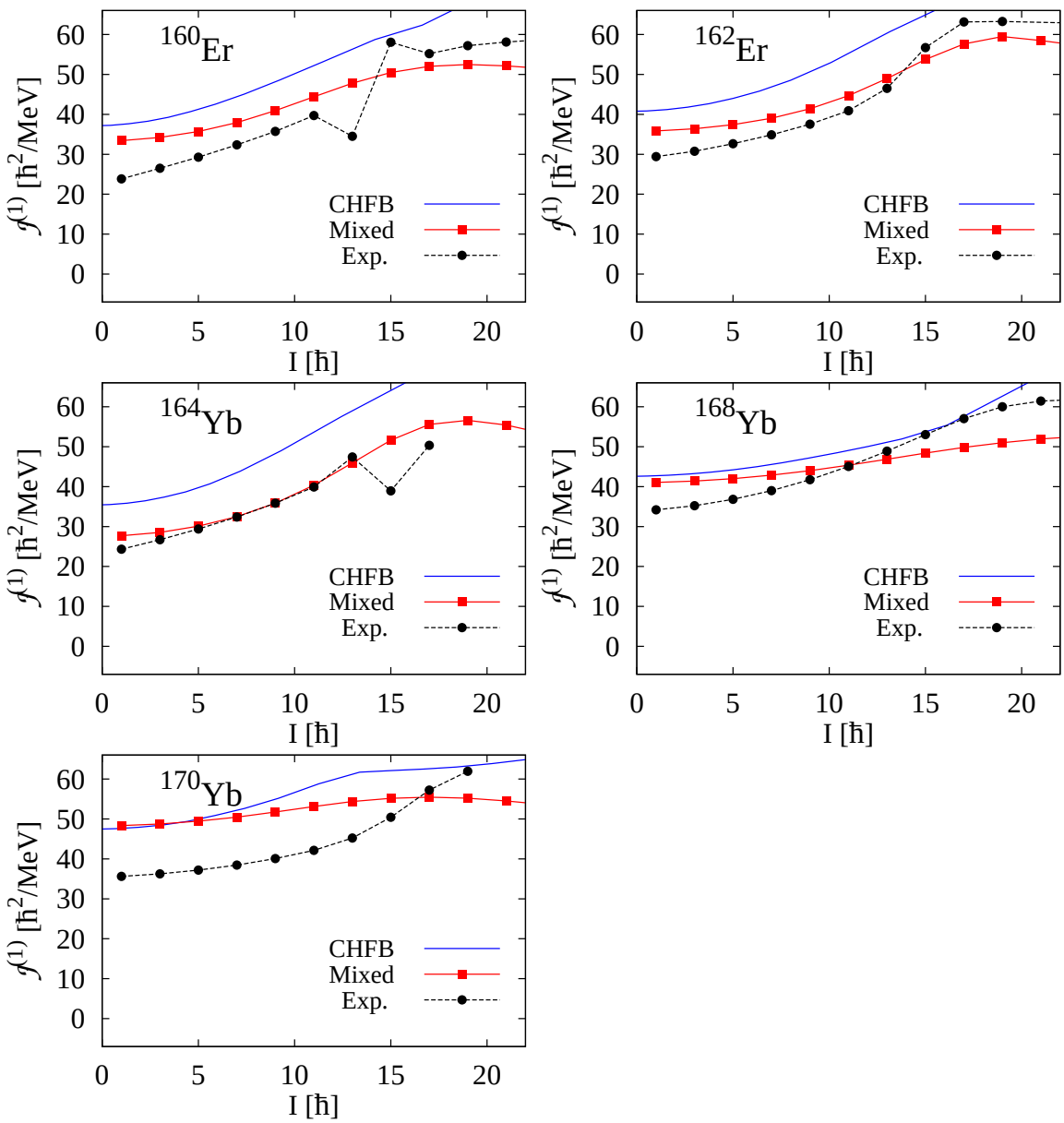

Figure 4.29: Moments of inertia versus spin value for the Er and Yb obtained by various calculations in comparison with the experimental data.

even-odd mass-differences. In particular, the calculated inertias for nuclei ^{156}Gd and ^{170}Yb considerably overestimate the experimental data since their calculated pairing gaps underestimate the even-odd mass-differences. Compared to the results of the cranked HFB method, better agreements with the experimental data are obtained except for the case of ^{170}Yb. Especially for nuclei ^{160}Gd, ^{162}Dy and ^{164}Dy, the calculated inertias by the projected configuration mixing at the lowest spin well reproduce the experimental data. As for the spin-dependence, the calculated inertias by the simple projections from one intrinsic state in Fig. 4.30 and 4.31 are almost constant or decrease as functions of spin. However, the moments of inertia increase as functions of spin by performing the configuration mixing, which are consistent with the exper-

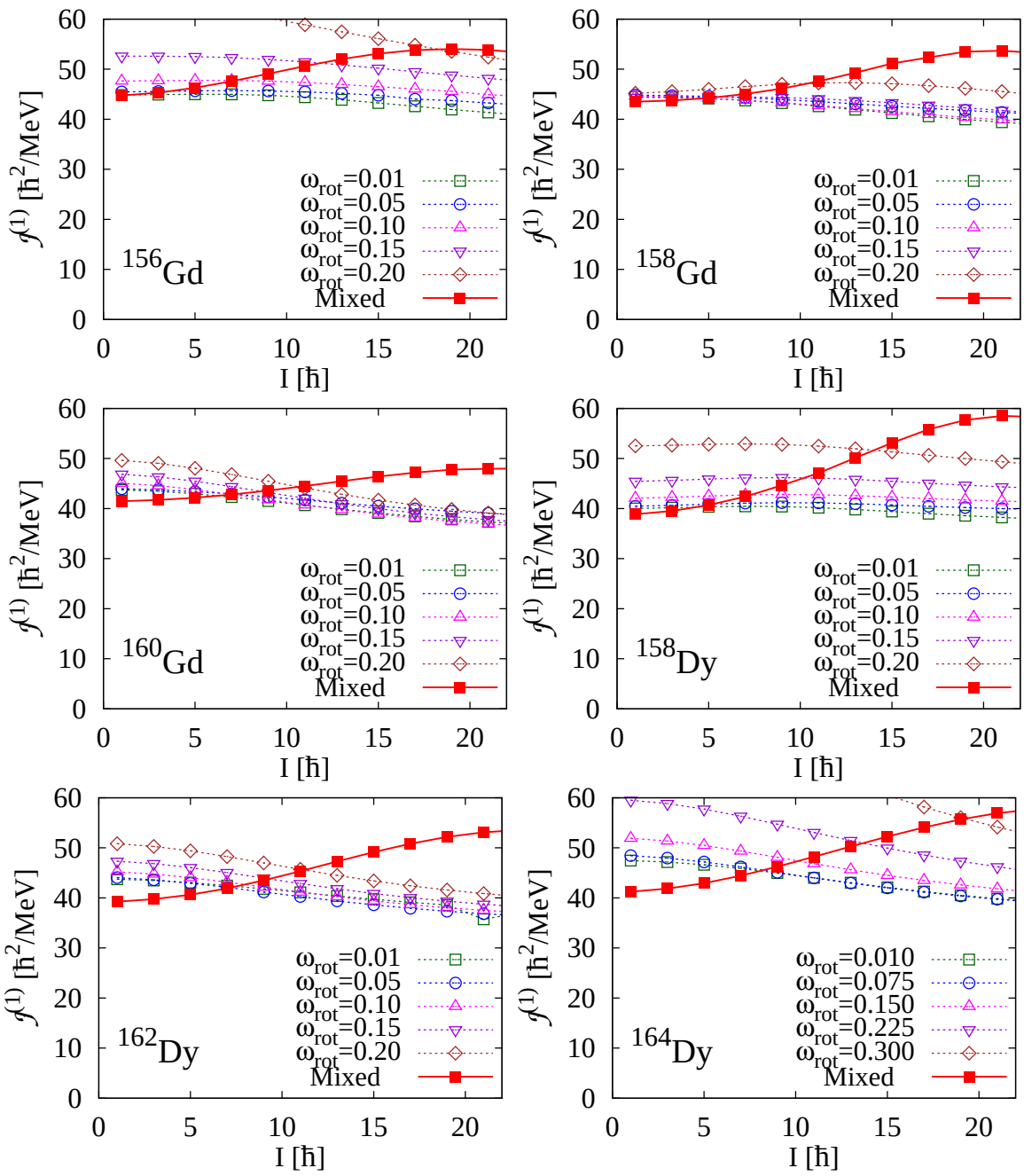

Figure 4.30: Moments of inertia versus spin value for the Gd and Dy obtained by the simple projection from one intrinsic HFB state with five values of the cranking frequency in Table 4.1 The results of the projected configuration mixing are also included.

imental data. In particular, the calculated inertias by the projected configuration mixing for nuclei ^{160}Gd, ^{162}Dy, ^{164}Dy and ^{164}Yb very well reproduce the experimental data. Thus, it is important to perform the projected configuration mixing in order to reliably calculate the high-spin rotational states.

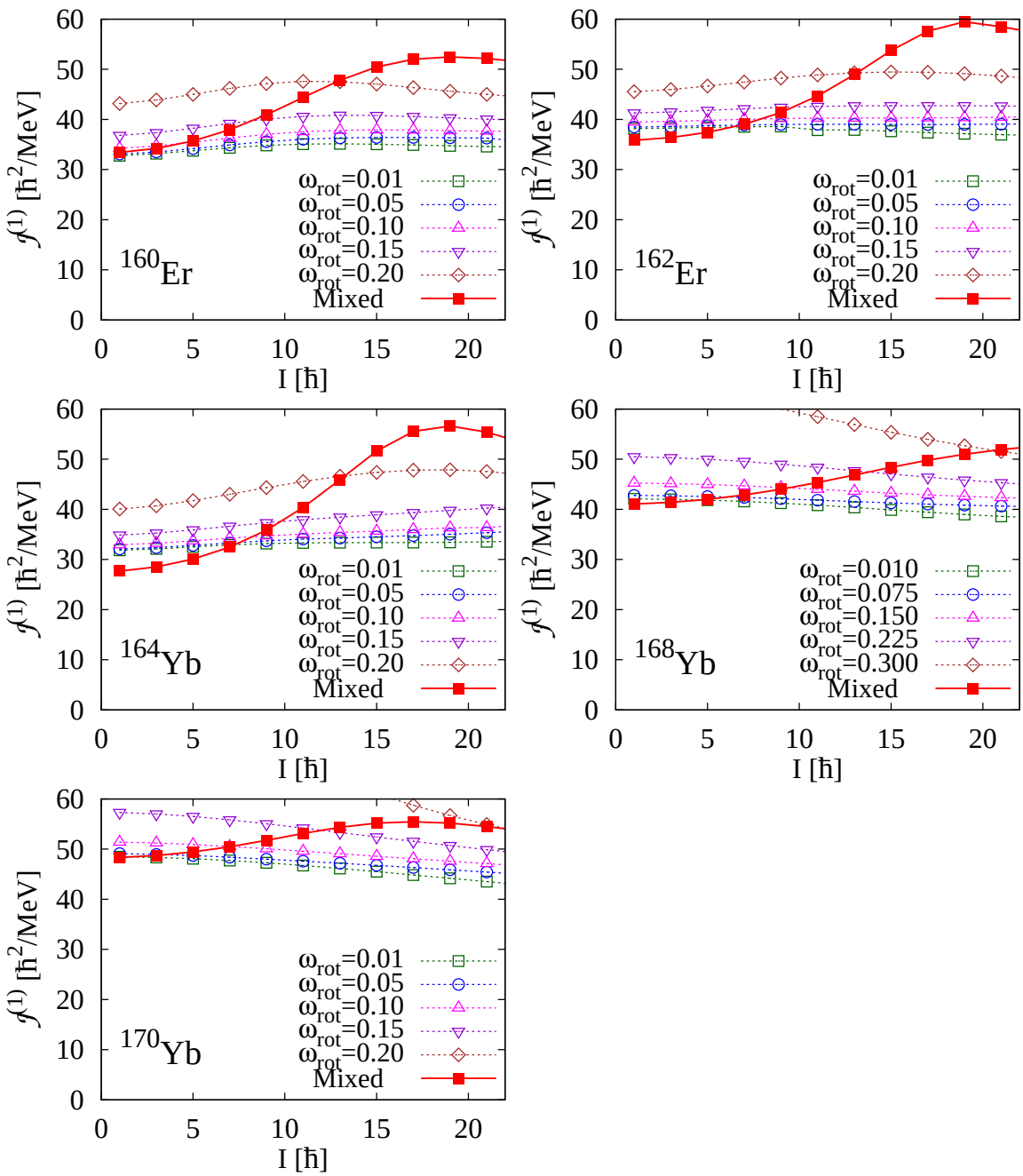

Figure 4.31: Moments of inertia versus spin value for the Er and Yb isotopes obtained by the simple projection from one intrinsic HFB state with five values of the cranking frequency in Table 4.1 The results of the projected configuration mixing are also included.

4.4.2 S-band for ^{164}Er

One of the interesting phenomena at the high-spin states is the band-crossing between the g-band and the s-band. The s-band is interpreted as the rotational band where the lowest two quasineutrons align their angular momenta along the axis of the collective rotation. This is caused by the cranking term $-\omega_{\rm rot}\hat{J}_y$ because the alignment of qusiparticles gains energy at high rotational frequency. This band crossing has been

known for many years as the origin of the backbending phenomenon first observed in Ref. [45], see e.g. discussions in Refs. [19, 20].

In this section, we show the results for the s-band of the nucleus ^{164}Er. We use the oscillator basis with $N_{\rm osc}^{\rm max} = 12$. As shown in Fig. 4.5, the alignment of the lowest two quasineutrons occurs at $\hbar\omega_{\rm rot} \approx 0.25$ MeV in the cranked HFB calculation, in which the neutron pairing correlation vanishes. The proton pairing gap gradually decrease from $\bar{\Delta} = 0.83$ MeV at $\hbar\omega_{\rm rot} = 0.25$ MeV to $\bar{\Delta} = 0.45$ MeV at $\hbar\omega_{\rm rot} = 0.40$ MeV. The set of four almost equidistant cranking frequencies, $(\hbar\omega_{\rm rot}^{(n)}, n = 1:4) = (0.25, 0.30, 0.35, 0.40)$ MeV, is adopted for the configuration mixing calculation of the s-band. The value of norm cut-off is taken to be 10^{-8}.

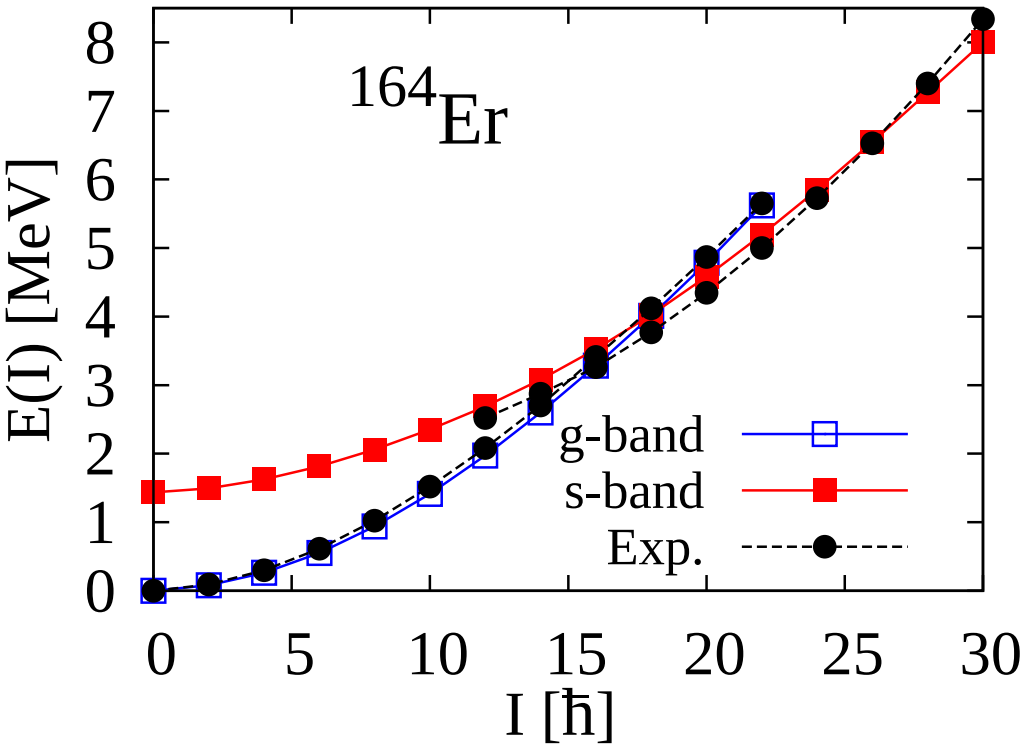

Figure 4.32: Excitation energy spectra of the g-band and s-band for ^{164}Er. Experimentally measured spectra are also included. The 0^+ energy of g-band is taken as the the energy origin in each spectrum.

The calculated s-band in comparison with the experimental data is shown in Fig. 4.32. The calculated g-band, which is already discussed in the previous section, is also included for comparison. The 12^+ excitation energy of the s-band calculated by the projected configuration mixing is 2.69 MeV, which is slightly higher than the experimental data 2.5192 MeV. To see the detailed behavior, the excitation energies subtracting the reference rotational energy $I(I+1)/80$ are shown in Fig. 4.33. The calculated s-band slightly overestimates the experimental data. The g-s band crossing is observed at $I \approx 18$ in our calculation although it appears at higher spin compared with the experimental data.

The first moments of inertia by various calculations are shown in Fig. 4.34 and 4.35

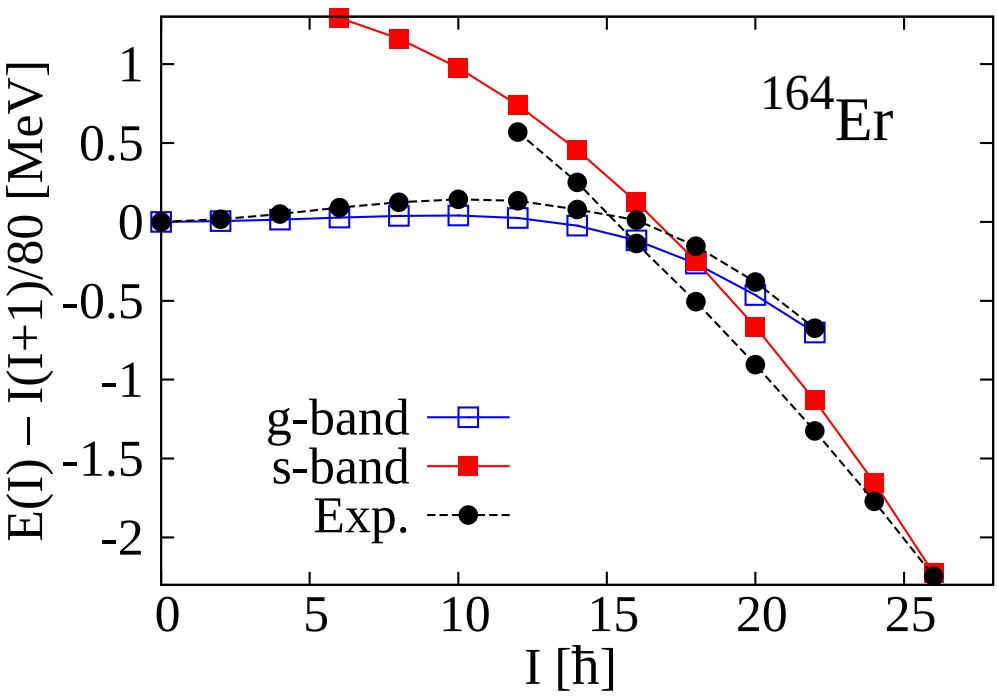

Figure 4.33: Excitation energy spectra subtracting the reference rotational energy, $I(I+1)/80$ MeV for the g-band and s-band of ^{164}Er. Experimentally measured spectra are also included. The 0^+ energy of g-band is taken as the the energy origin in each spectrum.

in comparison with the experimental data. The calculated inertia by the projected configuration mixing for the s-band overestimate the experimental data at $I \geq 19$, which may be due to the fact that the calculated neutron pairing gap vanishes by the cranked HFB for the cranking frequencies $\hbar\omega_{\rm rot} \geq 0.25$ MeV. Compared to the inertia by the cranked HFB, the slightly better agreement with the experimental data is obtained. The calculated inertias by the simple projections from one cranked HFB state with frequencies $\hbar\omega_{\rm rot} \gtrsim 0.25$ MeV drastically decrease as functions of spin. Compared to these results, a better agreement with the experimental data is obtained by performing the configuration mixing although the spin-dependence of the moment of inertia is opposite to that of the experimental data.

4.5 Short summary

In this chapter, we studied the "angular momentum projected multi-cranked configuration" as a method to reliably calculate the high-spin states by the angular momentum projection technique. In this method, the rotational states are described by superposing the several projected states obtained by the projection from the cranked states with different frequencies. Thus, we can compromise between the angular momentum projection method and the cranking model. In this work, the method has been applied to a lot of ground-state bands of nuclei in the rare-earth region, the ground-state

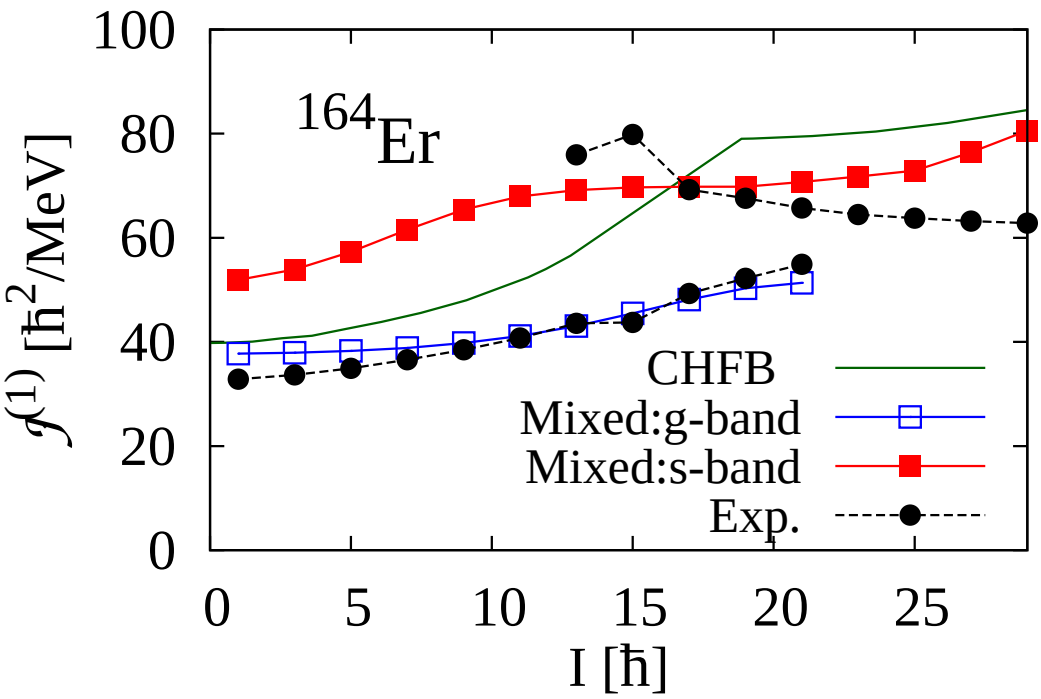

Figure 4.34: Moments of inertia versus spin value for the g-band and the s-band of ^{164}Er. The calculated inertias by the projected configuration mixing and by the cranked HFB in comparison with the experimental data are plotted. The result for the g-band is also included.

band of a unstable nucleus ^{40}Mg, the superdeformed band of ^{152}Dy and the s-band of ^{164}Er employing the Gogny-D1S effective interaction. It has been confirmed that the realistic rotational band can be calculated by the configuration mixing calculation.

One of the examples of application is the ground state rotational band of a typical rare-earth nucleus ^{164}Er. A good agreement with the experimental data has been obtained for the energy spectrum, the moments of inertia and the $B(E2)$ values in the range $0 \leq I \leq 22$. In particular, the calculated inertias by the projected configuration mixing increase as a function of spin although those of the simple projection from one cranked state are almost constant. As for the ground-state band of ^{40}Mg, the calculated inertias by the simple projections from one intrinsic state decrease as a function of spin. However, if the configuration mixing is performed, the reasonable results are obtained: the inertias are constant at lower spin and increase at higher spin. As for the superdeformed band of ^{152}Dy, almost constant inertia as a function of spin is obtained over the wide range of spin while the calculated inertias by the simple projections from one cranked state considerably decrease with increasing the spin. The calculated inertias by the projected configuration mixing have been compared with the semiclassical inertias by the cranked HFB calculations. While the inertias for ^{40}Mg and ^{152}Dy agree quite well, a much better agreement with the experimental data is obtained for ^{164}Er compared with the semiclassical inertias. In these three examples, we have also investigated the dependence on the chosen set of the cranking

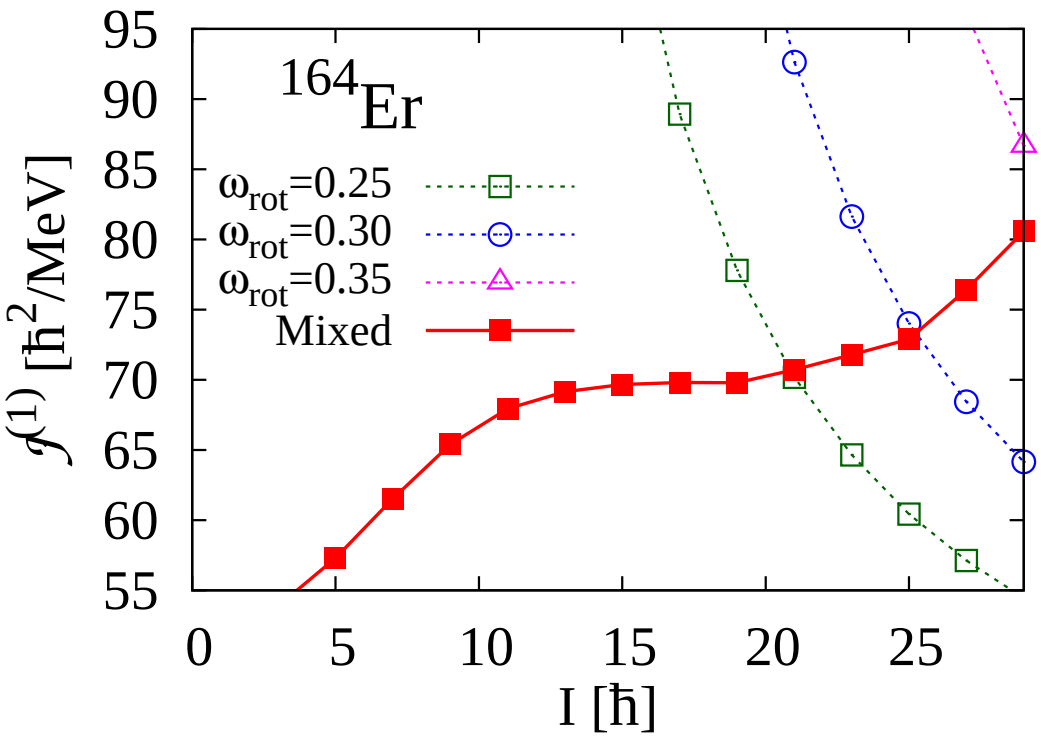

Figure 4.35: Moments of inertia versus spin value for the s-band of ^{164}Er obtained by the simple projections from one intrinsic HFB state. The results of the projected configuration mixing are also included.

frequencies. The converged results are obtained if the number of the configurations is sufficient, and the necessary number is four or five.

We have systematically investigated the ground-state bands of nuclei in the rare-earth region. For all cases, the improvement of the moments of inertia has been confirmed: The calculated inertias by the projected configuration mixing increase as functions of spin. In particular, for nuclei ^{160}Gd, ^{162,164}Dy and ^{164}Yb, very nice agreements with the experimental data have been obtained. Compared to the semiclassical inertias calculated by the cranked HFB, better agreements with the experimental data has been obtained. The application to the s-band of ^{164}Er has been also done. The appearance of the band crossing between the g-band and the s-band has confirmed at $I \approx 18$ in the projected configuration mixing calculation although it occurs at about $3\hbar$ higher spin compared with the experimental data. The calculated inertias of the s-band by the projected configuration mixing slightly overestimate the experimental data. However, compared to the results of the simple projections from one cranked state, much better spin-dependence of the inertias has been obtained.

Thus, it is important to perform the projected configuration mixing in order to reliably calculate the high-spin states by the angular momentum projection technique. In addition, it has been found that the results of the projected configuration mixing are essentially independent of the chosen sets of the cranking frequencies, and the necessary number of the configurations is rather small, something like four to five.

Chapter 5

Rotational motions of the triaxially deformed nuclei at the high-spin states

5.1 Introduction

Although various nuclear rotational motions are predicted by the macroscopic model, they should be studied from the microscopic view points. Recent development of accelerators and detectors enables us to explore high-spin states, where nucleus has large angular momentum, and the study of high-spin states is one of the interesting topics. While the well-known deformation in nuclei is the axially symmetric ellipsoidal deformation, the existence of triaxial deformation is suggested theoretically and experimentally. High-spin states of the triaxially deformed nuclei are especially interesting. Since the nuclear rotational motion is a motion based on restoring the rotational invariance, for the axially symmetric nuclei, only the rotational motion around one axis perpendicular to the symmetry axis occurs. On the other hand, the triaxially deformed nuclei can rotate around all three principal axes and this provides us various interesting rotational motions.

A lot of studies of high-spin states are based on the macroscopic models, e.g., the rotor model. They have many adjustable parameters and their predictive power is restricted. Since the nuclear rotational motion is a coherent motion of constituent particles, the microscopic understanding is necessary. At high-spin states, there exist exotic rotational bands such as the wobbling band and the chiral doublet band, where the presence of the triaxial deformation is crucial. The wobbling rotation is based on the vibrational motion of the rotational axis on top of the rotation around a principal axis, which generates the phonon-like multiple rotational bands. In the odd-odd nuclei with a particle and a hole nucleons, the three angular-momentum vectors, those of the core, the particle and the hole, align along the three mutually perpendicular directions. These angular-momentum vectors give rise to a right- or left-handed chiral geometry, which leads to the degenerate pair of bands called the chiral doublet band.

In this chapter, we study microscopically these two bands by the angular momentum projection method.

5.2 Microscopic model

It is important to study the dependence on the mean-field parameters like the deformation parameters and the pairing gaps for analyzing the wobbling band and the chiral doublet band. However, since it takes a lot of computing time for the calculations using the Gogny effective interaction, it is not convenient to employ it for investigating these rotational bands. In this chapter, as for the Hamiltonian we employ the Woods-Saxon single-particle potential and the schematic separable-type residual interactions. In this way we are able to rather arbitrarily change the mean-field parameters and to systematically study the dependence on them.

The symmetry broken intrinsic state is obtained by diagonalizing the following mean-field Hamiltonian,

$$\hat{h}_{\rm mf} = \hat{h}_{\rm def} - \sum_{\tau=n,p} \Delta_0^\tau (\hat{P}_\tau^\dagger + \hat{P}_\tau) - \sum_\tau \lambda_\tau \hat{N}^\tau - \boldsymbol{\omega}_{\rm rot} \hat{\boldsymbol{J}}, \tag{5.1}$$

where $\tau(=n,p)$ distinguishes the proton or neutron part. The first term $\hat{h}_{\rm def}$ is the deformed mean-field Hamiltonian given by

$$\hat{h}_{\rm def} = \sum_\tau (\hat{t}_\tau + \hat{V}_{\rm WS}^\tau), \tag{5.2}$$

where $\hat{t}$ and $\hat{V}_{\rm WS}$ are kinematic energy term and Woods-Saxon potential, respectively. The second term in Eq. (5.1) is the pairing part of the mean-field Hamiltonian and $\hat{P}_\tau^\dagger = \hat{G}_{00}^{\tau\dagger}$ is the monopole pair creation operator defined by

$$\hat{G}_{\lambda\mu}^{\tau\dagger} \equiv \frac{1}{2} \sum_{ij} \langle i | G_{\lambda\mu}^\tau | j \rangle \hat{c}_i^\dagger \hat{c}_{\tilde{j}}^\dagger, \tag{5.3}$$

which include the cut-off by single-particle energies,

$$G_{\lambda\mu}^\tau = P_{\rm c} \tilde{G}_{\lambda\mu}^\tau P_{\rm c}^T. \tag{5.4}$$

The cut-off matrix $P_{\rm c}$ is given by

$$(P_{\rm c}^\tau)_{ij} = \sum_k w_{ik}^\tau w_{jk}^\tau \sqrt{f_{\rm c}(\epsilon_k^\tau)}, \tag{5.5}$$

where w_{ik}^τ and ϵ_k are the eigenvector and the energy eigenvalue of the deformed mean-field Hamiltonian and the cut-off function is given by

$$f_{\rm c}(\epsilon) = \frac{1}{2} \left[1 + {\rm erf} \left(\frac{\epsilon - \lambda + \Lambda}{d_{\rm cut}} \right) \right]^{1/2} \left[1 + {\rm erf} \left(\frac{-\epsilon + \lambda + \Lambda}{d_{\rm cut}} \right) \right]^{1/2}, \tag{5.6}$$

with the error function defined as

$$\mathrm{erf}(x) = \frac{2}{\sqrt{\pi}} \int_0^x dt\ e^{-t^2}. \tag{5.7}$$

The parameters of the cut-off function are chosen to be $\Lambda = 1.2\hbar\omega$ and $d_{\mathrm{cut}} = 0.2\hbar\omega$ with $\hbar\omega = 41/A^{1/3}$. The mean pairing gap is defined by

$$\Delta_\tau \equiv \Delta_0^\tau \frac{\mathrm{Tr}\ G_{00}^\tau \kappa^\tau}{\mathrm{Tr}\ \kappa^\tau}, \tag{5.8}$$

with the pairing tensor κ^τ. The third term in Eq. (5.1) is included to constrain the expectation value of the particle number, and the forth term is the cranking term.

The triaxially deformed Woods-Saxon potential is composed of the central part $V_{\mathrm{C}}(\boldsymbol{r})$ and spin-orbit part $V_{\mathrm{SO}}(\boldsymbol{r})$,

$$V_{\mathrm{WS}}(\boldsymbol{r}) = V_{\mathrm{C}}(\boldsymbol{r}) + V_{\mathrm{SO}}(\boldsymbol{r}), \tag{5.9}$$

$$V_{\mathrm{SO}}(\boldsymbol{r}) = \lambda_{\mathrm{SO}} \left(\frac{\hbar}{2M_{\mathrm{red}}c}\right)^2 (\nabla V_{\mathrm{C}}(\boldsymbol{r})) \cdot \left(\boldsymbol{\sigma} \times \frac{1}{i}\nabla\right), \tag{5.10}$$

where $M_{\mathrm{red}} = M(A-1)/A$ with mass number A and nucleon mass M, and $\boldsymbol{\sigma}$ is the Pauli spin matrix. The central part of the potential $V_{\mathrm{C}}(\boldsymbol{r})$ is given by

$$V_{\mathrm{C}}(\boldsymbol{r}) = \frac{V}{1 + \exp[\mathrm{dist}_\Sigma(\boldsymbol{r})/a)]},\ V = -V_0 \left(1 + (-)^{M_I} \kappa \frac{N-Z}{A}\right), \tag{5.11}$$

where $M_I = 0$ for the proton part and $M_I = 1$ for the neutron part. $\mathrm{dist}_\Sigma(\boldsymbol{r})$ represents a distance between a given point $\boldsymbol{r}$ and the deformed surface Σ specified by the radius,

$$R(\theta,\phi) = R_0 c_v(\alpha_{2\mu}, \alpha_{4\mu}) \left[1 + \sum_\mu \alpha_{2\mu} Y_{2\mu}(\theta,\phi) + \sum_\mu \alpha_{4\mu} Y_{4\mu}(\theta,\phi)\right], \tag{5.12}$$

where $c_v(\alpha_{2\mu}, \alpha_{4\mu})$ is determined to satisfy the volume conservation of the nucleus. The set of deformation parameters used in this work $(\beta_2, \gamma, \beta_4)$ is related to $(\alpha_{2\mu}, \alpha_{4\mu})$ by

$$\begin{cases} \alpha_{20} = \beta_2 \cos\gamma \\ \alpha_{22} = \alpha_{2-2} = -\frac{1}{\sqrt{2}}\beta_2 \sin\gamma \\ \alpha_{40} = \frac{1}{6}\beta_4(5\cos^2\gamma + 1) \\ \alpha_{42} = \alpha_{4-2} = -\sqrt{\frac{5}{6}}\beta_4 \cos\gamma \sin\gamma \\ \alpha_{44} = \alpha_{4-4} = \sqrt{\frac{35}{72}}\beta_4 \sin^2\gamma \end{cases}, \tag{5.13}$$

which are defined in the range $\beta_2 \geq 0$ and $-120^\circ \leq \gamma \leq 60^\circ$. The other $\alpha_{\lambda\mu}$ are taken to be zero. γ represents the tiraxiality of the nuclear deformation, and for $\gamma = -120^\circ, -60^\circ, 0^\circ$ and 60°, nuclei have the axially symmetric shapes. For proton, the Coulomb potential is added by considering the nucleus to be a uniformly charged body with the surface Σ. Therefore, the deformed mean-field Hamiltonian $\hat{h}_{\mathrm{def}}$ is written as

$$\hat{h}_{\mathrm{def}} = \sum_\tau (\hat{t}_\tau + \hat{V}_{\mathrm{C}}^\tau + \hat{V}_{\mathrm{SO}}^\tau + \hat{V}_{\mathrm{Coul}}). \tag{5.14}$$

The set of parameters $(V_0, \kappa, R_0, a, \lambda_{\rm SO})$ used in this work is recently proposed by R. Wyss [46], and their actual values are listed in Ref. [47]. The depth V_0 and the diffuseness a are same in the central and spin-orbit potential. This parameter set is determined to reproduce systematically the moments of inertia and the quadrupole moments for the medium and heavy nuclei.

To perform the angular momentum projection, we need the spherically invariant Hamiltonian. We employ the following Hamiltonian composed of the spherical Woods-Saxon potential and of the schematic separable-type residual interactions:

$$\hat{H} = \hat{h}_{\rm sph} - \frac{1}{2}\chi \sum_{\lambda} \sum_{\tau,\tau'} : \hat{F}^{\tau}_{\lambda} \cdot \hat{F}^{\tau'}_{\lambda} : - \sum_{\lambda=0,2} \sum_{\tau} g^{\tau}_{\lambda} \hat{G}^{\tau\dagger}_{\lambda} \cdot \hat{G}^{\tau}_{\lambda}, \tag{5.15}$$

The spherical mean-field Hamiltonian $\hat{h}_0$ given by

$$\hat{h}_{\rm sph} = \sum_{\tau} (\hat{t}_{\tau} + \hat{V}^{({\rm sph})\tau}_{\rm WS}), \tag{5.16}$$

where $\hat{t}$ and $\hat{V}^{({\rm sph})\tau}_{\rm WS}$ are the kinetic energy and the spherical Woods-Saxon potential, respectively. The multipole interactions consist of the particle-hole channel and the particle-particle pairing channel. For the particle-hole channel (F-type) interaction, the operator $\hat{F}_{\lambda\mu}$ is defined as

$$\hat{F}^{\tau}_{\lambda\mu} \equiv \sum_{ij} \langle i|\hat{F}^{\tau}_{\lambda\mu}|j\rangle \hat{c}^{\dagger}_{i}\hat{c}_{j}, \tag{5.17}$$

and, in this calculations we take $\lambda = 2, 3$ and 4. For the pairing channel (G-type) interaction, we include $\lambda = 0$ and 2 components. As for the form factor of F-type and G-type interactions, the following same surface-type one, which is the derivative of spherical Woods-Saxon potential, is used,

$$F^{\tau}_{\lambda\mu}(\boldsymbol{r}) = \tilde{G}^{\tau}_{\lambda\mu}(\boldsymbol{r}) = R^{\tau}_{0} \frac{dV^{\tau}_{\rm C}(r)}{dr} Y_{\lambda\mu}(\theta, \phi). \tag{5.18}$$

The strength of the particle-hole channel interaction, χ, is taken to be the so-called selfconsistent value [9],

$$\chi = (\kappa_n + \kappa_p)^{-1}, \quad \kappa_{\tau} = (R^{\tau}_{0})^2 \int dr \rho^{\tau}_{0}(r) \frac{d}{dr}\left(r^2 \frac{dV^{\tau}_{\rm C}(r)}{dr}\right), \tag{5.19}$$

where $\rho^{\tau}_{0}(r)$ is the spherical density obtained by calculation with the spherical Woods-Saxon potential. This factor is independent of the multipolarity λ. For the pairing channel, the monopole strength g^{τ}_{0} is adjusted by the requirement that the mean pairing gap Δ_{τ} in Eq. (5.8) reproduces the even-odd mass-difference. In this work, this microscopic model is applied to the odd and odd-odd nuclei, and the monopole strength is taken to be a average value of the strengths for the two neighboring even-even nuclei. The quadrupole pairing strength g^{τ}_{2} is assumed to be proportional to the monopole pairing strength g^{τ}_{0}, $g^{\tau}_{2}/g^{\tau}_{0} = 1.98$, which is the same for both the proton and neutron; this ratio is determined to reproduce the 2^+ excitation energy for the nucleus ^{164}Er.

5.3 Triaxial deformation

In this thesis, the triaxially deformed shape is defined as follows: The body-fixed frame is defined by diagonalizing the quadrupole tensor, i.e., the (x, y, z) coordinate axes refer to the principal axes for the triaxially deformed shape. The set of deformation parameters (β, γ) is related to $\langle \hat{Q}_{2\mu} \rangle$ and $\langle r^2 \rangle$ by

$$\beta = \frac{4\pi}{5}\frac{Q^2}{\langle r^2 \rangle}, \quad \langle \hat{Q}_{20} \rangle = Q\cos\gamma, \quad \langle \hat{Q}_{22} \rangle = -\frac{1}{\sqrt{2}} Q \sin\gamma,$$
$$\langle \hat{Q}_{21} \rangle = \langle \hat{Q}_{2-1} \rangle = 0, \quad \langle \hat{Q}_{22} \rangle = \langle \hat{Q}_{2-2} \rangle. \tag{5.20}$$

Namely, the parameter γ represents the triaxiality of the nuclear deformation. Although the nuclear shapes can be represented only in the range $\beta_2 \geq 0$ and $0° \leq \gamma \leq 60°$, the set of the deformation parameters (β, γ) should be extended in to the range $\beta_2 \geq 0$ and $-120° \leq \gamma \leq 60°$ for the rotating triaxially deformed nuclei since it is necessary to consider the relation between the rotation axis and the principal axes, as shown in Fig. 5.1. Nuclei have the axially symmetric deformation in the case of $\gamma = -120°, -60°, 0°$ and $60°$, and the deformation with $\gamma = -120°$ and $0°$ ($-60°$ and $60°$) represents the prolate (oblate) deformed shape.

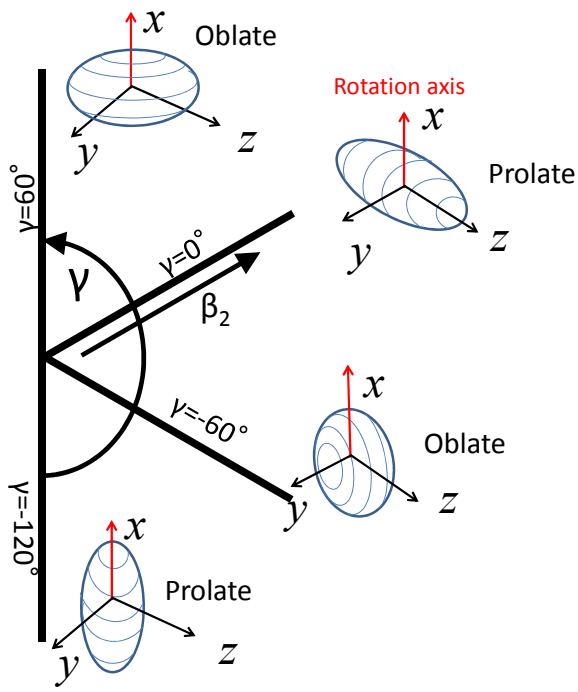

Figure 5.1: Schematic picture of the relation between the rotation axis and the γ deformation. The main rotation axis is chosen to be the x-axis. γ deformations are classified into the three regions, $0° < \gamma < 60°$, $-60° < \gamma < 0°$ and $-120° < \gamma < -60°$.

5.4 Tilted-axis cranking

For the axially symmetric deformed nuclei, only the rotation around one axis, which is perpendicular to the symmetry axis, occurs. In such case, it is sufficient to consider the cranked state with the cranking frequency around one axis. However, for the triaxially deformed nuclei, it is necessary to take into account the rotation around the other two axes. In the three dimensional version of the cranking model, the so-called tilted axis cranking [48], the Hamiltonian is transformed as

$$H' = H - \boldsymbol{\omega}_{\rm rot} \cdot \hat{\boldsymbol{J}}. \tag{5.21}$$

The intrinsic frame is defined by diagonalizing the quadrupole tensor; i.e., the vector $\boldsymbol{\omega}_{\rm rot} = (\omega_x, \omega_y, \omega_z)$ refers to the principal axes for the triaxially deformed shape. Recently, the titted-axis cranking was also successfully applied for the nuclear rotational motion at the high-spin state [49, 50].

Nuclei considered in the previous chapter have axially symmetric shape in the non-cranked ($\omega_{\rm rot} = 0$) HFB calculation. Therefore, the mean-field states for the multi-cranked configuration mixing calculations are obtained by the one dimensional cranking model.

5.5 Wobbling band

5.5.1 Introduction

The wobbling rotational band was first predicted by Bohr and Mottelson for even-even nuclei by the macroscopic triaxial rotor model [9], and is composed of the phonon-like multiple rotational sequences. The wobbling excitations are vibrational motions of the rotation axis, which are built on the uniformly rotated (yrast) state. For the nuclear wobbling band, the presence of triaxial deformation is crucial, and its identification is regard as a proof of the triaxial deformation. Its characteristic feature is strong out-of-band ($\Delta I = 1$) $E2$ transitions between each sequences. Such band has been first observed experimentally in the so-called triaxial superdeformed (TSD) band for the odd nucleus ^{163}Lu [10], and nowadays several other examples are known in neighboring nuclei [51].

The nuclear wobbling motion is described as phonon-like multiple rotational bands by the triaxial rotor model. The Hamiltonian of the triaxial rotor for the even-even nuclei is given by

$$\hat{H}_{\rm rot} = \frac{\hbar^2 \hat{I}_x^2}{2\mathcal{J}_x} + \frac{\hbar^2 \hat{I}_y^2}{2\mathcal{J}_y} + \frac{\hbar^2 \hat{I}_z^2}{2\mathcal{J}_z}, \tag{5.22}$$

where $\hat{I}_i (i = x, y, z)$ is the angular momentum operator along the principal axis in the body-fixed frame, and $\mathcal{J}_i$ is their moment of inertia. Here, $\mathcal{J}_x$ is chosen to be the largest moment of inertia. For $I \sim \langle \hat{I}_x \rangle$ near the high-spin yrast states, the excitation

energies of this Hamiltonian can be solved approximately and is given by

$$E(I,n) \sim \frac{I(I+1)}{2\mathcal{J}_x} + \omega_{\rm wob}(I)\left(n+\frac{1}{2}\right), \quad n = 0,1,2,\cdots, \tag{5.23}$$

where the wobbling frequency $\omega_{\rm wob}(I)$ is given by

$$\omega_{\rm wob} = \frac{\hbar I}{\mathcal{J}_x}\left[\left(\frac{\mathcal{J}_x}{\mathcal{J}_y}-1\right)\left(\frac{\mathcal{J}_x}{\mathcal{J}_z}-1\right)\right]^{1/2}, \tag{5.24}$$

which is related to all three moments of inertia and proportional to the spin I. The first term in Eq. (5.23) represents the energy of the uniform rotation around the x-axis, and the second term represents the contribution coming from rotations around the other two axes. Wobbling excitations are the phonon-like excitations and correspond to the tilting of the collective angular momentum vector. Therefore, the nuclear wobbling motion is interpreted as the quantized vibrational motions of the total angular momentum vector around the main rotation axis and has the multiple band structure as shown in Fig.5.2.

For the high-spin, $I \gg 1$, the in-band and out-of-band $E2$ transition probabilities are approximately given by

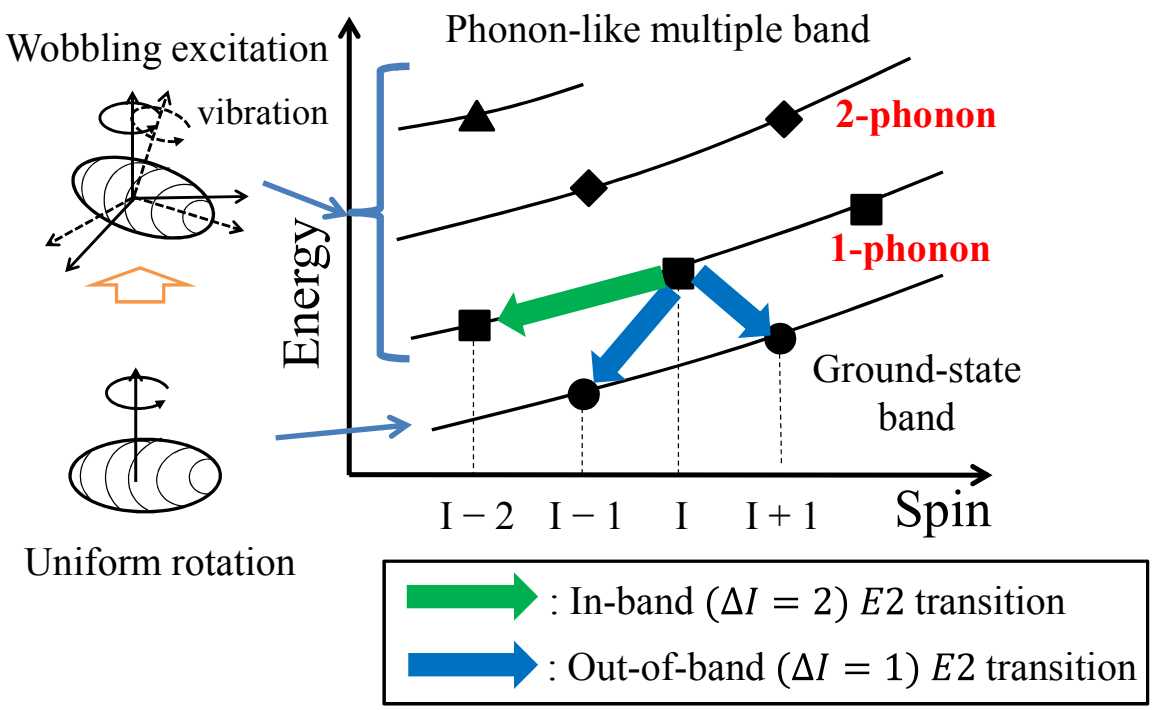

Figure 5.2: Schematic picture of the wobbling motion and their band structure. The nuclear wobbling motion is composed of the phonon-like multiple bands, which are connected with the in-band ($\Delta I = 2$) $E2$ transitions (green arrow) and the out-of-band ($\Delta I = 1$) $E2$ transitions (blue arrow).

$$B(E2; I\ n \to I-2\ n) \sim Q^2 \cos^2(\gamma + 30^\circ), \tag{5.25}$$

$$B(E2; I\ n \to I \pm 1\ n-1) \sim Q^2 \frac{n}{I} \beta^2 \left[\left(\frac{W_z}{W_y} \right)^{1/4} \sin(\gamma + 60^\circ) \mp \left(\frac{W_z}{W_y} \right)^{1/4} \sin\gamma \right]^2, \tag{5.26}$$

where

$$W_y \equiv \frac{1}{\mathcal{J}_z} - \frac{1}{\mathcal{J}_x}, W_z \equiv \frac{1}{\mathcal{J}_y} - \frac{1}{\mathcal{J}_x}, \tag{5.27}$$

$$Q^2 \equiv \frac{9}{16\pi^2} e^2 Z^2 R^4 \beta^2, \tag{5.28}$$

with $R \approx 1.2A^{1/3}$. Comparing Eq. (5.25) and (5.26), the out-of-band $E2$ transition probability is smaller than the in-band one by the factor $1/I$. Moreover, from Eq. (5.26), depending the range of γ deformation, we obtain the selection rule [52],

$$\begin{cases} B(E2; I\ n \to I+1\ n-1) < B(E2; I\ n \to I-1\ n-1) \\ \qquad\qquad (0^\circ < \gamma < 60^\circ, -120^\circ < \gamma < -60^\circ) \\ B(E2; I\ n \to I+1\ n-1) > B(E2; I\ n \to I \pm 1\ n-1) \\ \qquad\qquad (-60^\circ < \gamma < 0^\circ) \end{cases}, \tag{5.29}$$

which produces the staggering of the out-of-band $E2$ transition probabilities between $I \to I+1$ and $I-1$.

The wobbling rotational band appears not only in even-even nuclei but also in odd nuclei. For odd nuclei, the collective rotation as well as the single-particle rotation should be considered, and instead of the rotor model, the particle-plus-rotor model is used. Recently, for odd nuclei two types of the wobbling motions, so-called the "transverse" and "longitudinal" wobbler, are proposed by Frauendorf and Dönau [53]: The spin-dependence of the one-phonon excitation energy in different for these two; the energy increases as spin in the longitudinal wobbler and decreases in the transverse wobbler. They are classified by the direction of the single-particle angular momentum vector and of the axis with the largest moment of inertia. In the transverse wobbler, the single-particle angular momentum vector is perpendicular to the axis with the largest moment of inertia, and in the longitudinal wobbler the single-particle angular momentum vector is aligned with the axis with the largest moment of inertia. The wobbling motion has been studied mainly by the macroscopic model, and its microscopic understanding is necessary. In this work, we study the wobbling band for the nucleus ^{163}Lu by the angular momentum projection method.

5.5.2 Results for $\gamma = 18^\circ$

The intrinsic mean-field states, from which the projection calculation is performed, should be calculated first. It is necessary to choose the parameters of the mean-field

Hamiltonian; the deformation parameters $(\beta_2, \gamma, \beta_4)$, the pairing gaps Δ_n and Δ_p, and the cranking frequency $\omega_{\rm rot}$. The deformation parameters are $\beta_2 = 0.42$ for the quadrupole deformation, $\beta_4 = 0.02$ for the hexadecapole deformation, and the triaxial deformations are chosen as $\gamma = 18°$. These parameters are chosen to minimize the total energy $E_{\rm total} = E_{\rm LDM} + \delta E_{\rm shell}$ by the Nilsson Strutinsky method, where the bulk part of the binding energies $E_{\rm LDM}$ is calculated by the liquid drop model and the their shell correction part $\delta E_{\rm shell}$, which is obtained from the single-paricle energies, is calculated using the Nilson potential. At high-spin state, the single-particle angular momentum vectors aligned along the rotation axis are favored. In addition, for odd nuclei the odd particle does not contribute to the pairing correlation. Then the pairing gap is reduced (so-called the blocking effect). Therefore, the pairing gaps are chosen to be $\Delta_n = \Delta_p = 0.5$ MeV for both neutrons and protons, are smaller than the phenomenological value for the even-even nuclei, $\Delta = 12/\sqrt{A} \sim 0.9$ MeV. The cranking frequency is chosen to be $\hbar\boldsymbol{\omega}_{\rm rot} = (0.2, 0, 0.01)$ MeV. The nucleus ^{163}Lu is proton-odd nucleus and the odd proton occupies the quasiparticle state coming from the $i_{13/2}$ particle-like orbit. The oscillator basis with $N_{\rm osc}^{\rm max} = 12$ is used.

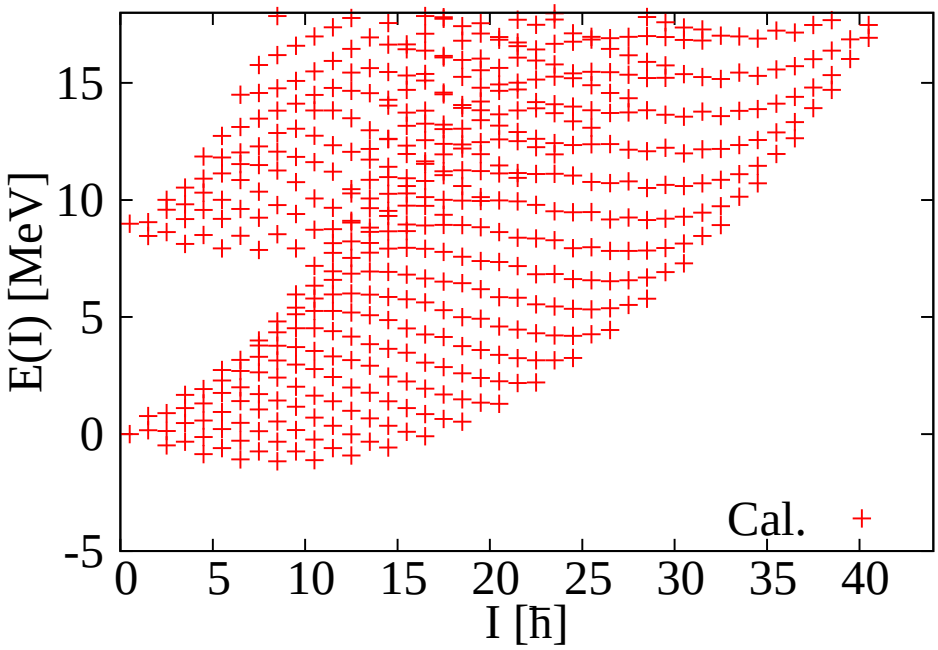

Figure 5.3: Energy spectrum for $\gamma = 18°$. Excitation energies by the angular momentum projection calculation for the nucleus ^{163}Lu are plotted as a function of spin I. In the experimental data, yrast, 1-phonon excitation and 2-phonon excitation bands are labeled by "TSD1", "TSD2" and "TSD3", respectively.

The resultant energy spectrum of the angular momentum projection, namely excitation energy $E(I)$ versus spin I, is shown in Fig. 5.3. It is found that the multiple band structure appears by the microscopic projection calculation. There is a minimum around $I \approx 10$ by the effect of rotation alignment. The multiple band structure can be more clearly recognized in Fig. 5.4, where the excitation energies from the yrast line

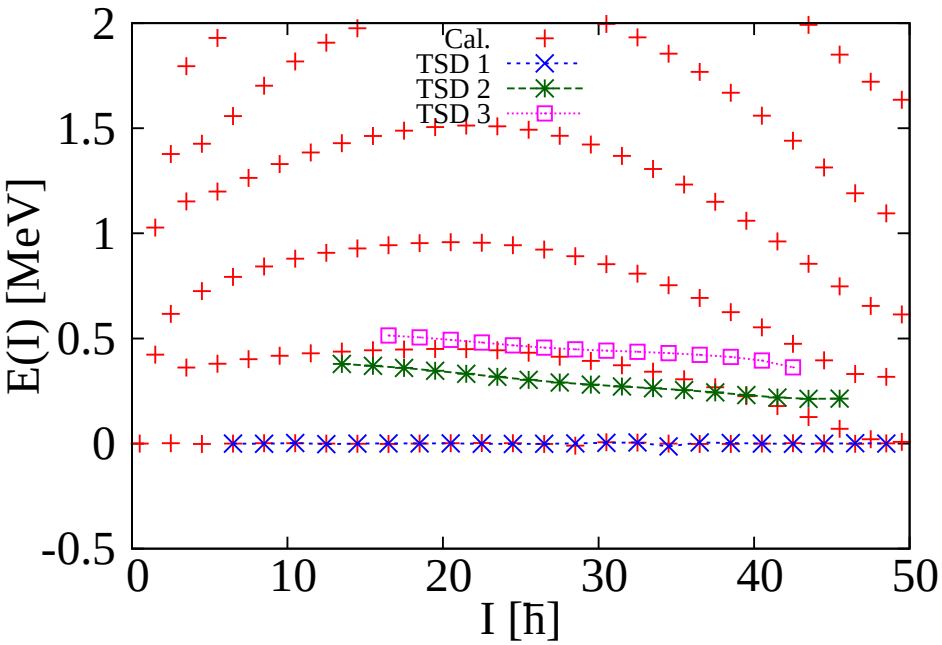

Figure 5.4: Excitation energies for $\gamma = 18°$. Excitation energies from the yrast line calculated by the angular momentum projection ("Cal.") for the nucleus ^{163}Lu are plotted as a function of spin I in comparison with the experimental data [54]. In the experimental data, yrast, 1-phonon excitation and 2-phonon excitation bands are labeled by "TSD1", "TSD2" and "TSD3", respectively.

are shown. The experimental data is also included with the lines, where TSD1, 2 and 3 are the yrast, 1-phonon excitation and 2-phonon excitation bands, respectively, and these three bands compose the multiple sequences. It is even more interesting that the calculated phonon excitation energies decrease as a function of spin I. The decrease of the excitation energies corresponds to the behavior of the transverse wobbler, and its trend is in agreement with the experimental data. In our calculation, the 2-phonon excitation energies are about twice of the 1-phonon excitation energies, which is one of the phonon-like properties. On the other hand, experimental data does not show this behavior. This indicates that other effects that cannot be described by the simple phonon-like picture should be included. Thus, the phonon-like multiple structure for odd nucleus ^{163}Lu appears in our microscopic calculation although the excitation energies are not very well reproduced.

The in-band $E2$ transition probabilities of yrast (TSD1) and 1-phonon excitation (TSD2) bands are shown in Fig. 5.5. Since the deformation parameters of the mean-field Hamiltonian are fixed, the calculated $B(E2)$ both of TSD1 and TSD2 bands are almost constant. On the other hand, the experimental $B(E2)$ decrease as a function of spin I, which suggest that the nuclear deformation changes with increasing the spin I. In order to include the effect of the change of the deformation, the projected configuration mixing calculation is necessary. For the wobbling motion, the in-band $B(E2)$ as well as the out-of-band $B(E2)$ are important.

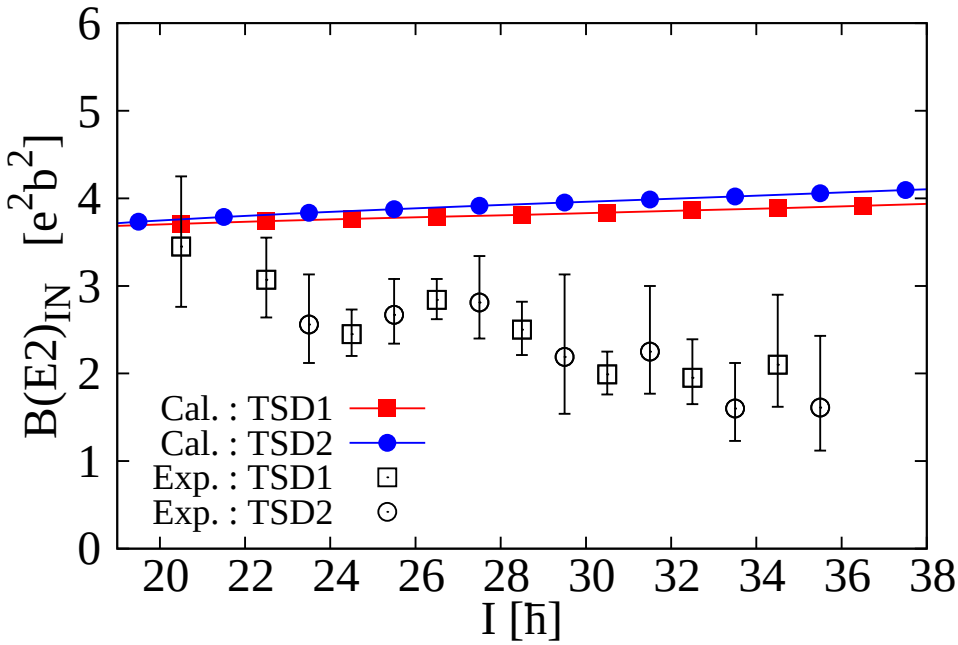

Figure 5.5: In-band $B(E2)$ for $\gamma = 18°$. The in-band $E2$ transition probabilities both of TSD1 and TSD2 band for ^{163}Lu are plotted as a function of spin I. The experimental data are taken from Ref. [55].

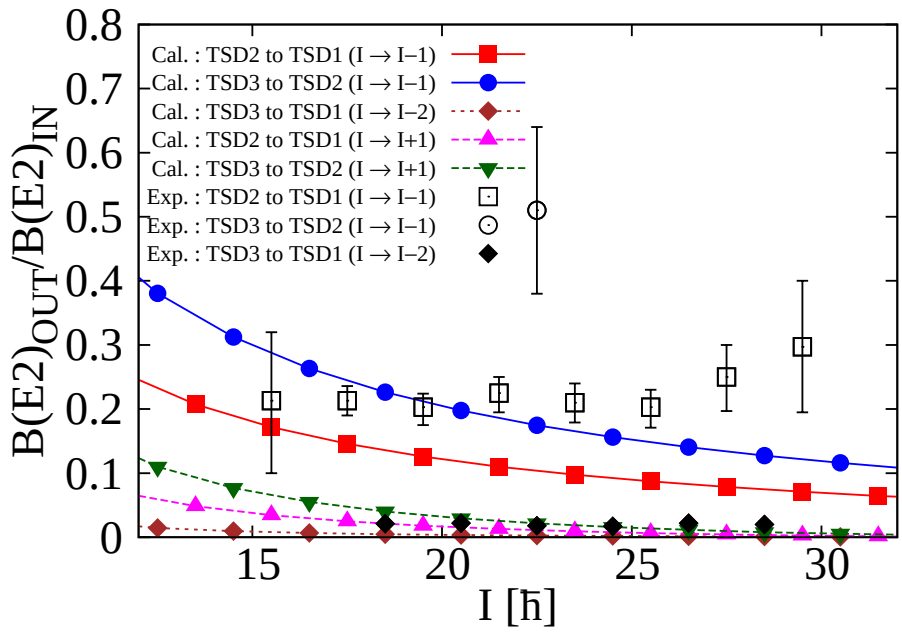

Figure 5.6: Ratios of the out-of-band $B(E2)$ to in-band $B(E2)$ for $\gamma = 18°$. The $\Delta n = 1$ and 2 $E2$ transition probabilities are plotted as a function of the spin I. For the $\Delta n = 1$ transitions, the $I \to I-1$ $(I+1)$ $E2$ transition probabilities are represented by the solid (dashed) lines. The experimental data is taken from Ref. [54, 55], where only the $I \to I-1$ transition probabilities are measured.

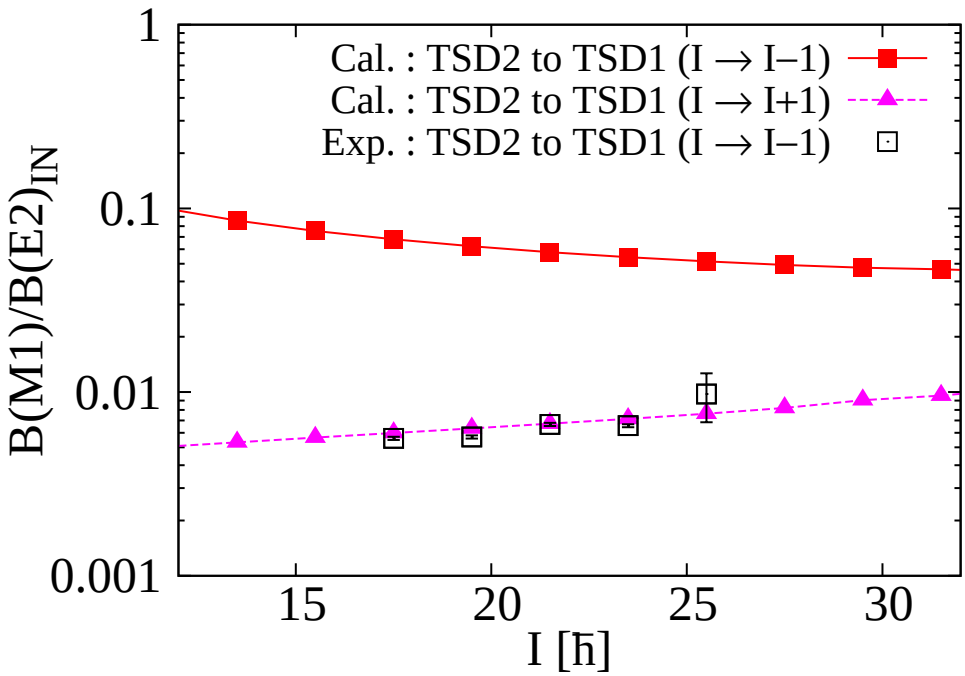

Figure 5.7: Ratios of the out-of-band $B(M1)$ to in-band $B(E2)$ for $\gamma = 18°$. Calculated $I \to I-1$ $(I+1)$ $B(M1)$ are represented by the solid (dashed) lines. The experimental data is taken from Ref. [56], where only the $I \to I-1$ transition probabilities are measured.

Fig. 5.6 shows the ratios of the out-of-band to in-band $E2$ transition probabilities, $B(E2)_{\rm OUT}/B(E2)_{\rm IN}$. Although calculated ratios are about half of the experimental values, the large values of the out-of-band $B(E2)$ indicate the strong collectivity between these bands. This strong collectivity of the out-of-band $E2$ transitions is the key for the identification of the wobbling band. The $B(E2)_{\rm OUT}$ well reproduce the following phonon-like properties:

$$\begin{cases} B(E2; I\ n=1 \to I\pm 1\ n=0) = 2B(E2; I\ n=2 \to I\pm 1\ n=1) \\ B(E2; I\ n=2 \to I\pm 1\ n=0) = 0 \end{cases} . \tag{5.30}$$

In the experimental data, only the out-of-band $I \to I-1$ $B(E2)$ are measured, which suggest that the $I \to I+1$ $B(E2)$ are very small values. The calculated $I \to I-1$ transition probabilities are larger than $I \to I+1$ transition probabilities. This fact suggests that in the wobbling band the nucleus ^{163}Lu has the positive-γ shape, see Eq. (5.29). The ratios of the out of band $B(M1)$ to the in-band $B(E2)$ are shown in Fig. 5.7. As in the case of the out-of-band $B(E2)$, since in the experimental data only the $I \to I-1$ B(M1) are measured, the $I \to I+1$ $B(M1)$ are very small values. The calculated $I \to I-1$ $B(M1)$ is always larger than the $I \to I+1$ $B(M1)$. However, the calculated ratios overestimate the experimental values by about the factor 10.

Therefore, it is found that the phonon-like multiple band structure appears by the angular momentum projection calculation and their sequences are connected by the

strong $E2$ transitions. The occurrence of the wobbling motion in odd nucleus ^{163}Lu is confirmed by our fully microscopic calculation, although the quantitative agreement with the experimental data is not satisfactory.

5.5.3 Negative-gamma deformation

For understanding the mechanism of the wobbling motion, it is important to consider not only the positive-γ but also negative-γ shapes. For the rotating triaxially deformed nuclei, γ deformations are classified into the three regions, $0° < \gamma < 60°$, $-60° < \gamma < 0°$ and $-120° < \gamma < -60°$, in relation to the main rotation axis, as shown in Fig. 5.1. As mentioned before, for the wobbling band there are the selection rule (5.29) for out-of-band $E2$ transition probabilities depending on these γ range [52], and the relation between the odd-particle angular momentum vector and the axis with the largest moment of inertia is crucial for the wobbling motion of the odd nuclei [53].

Also in the cranking calculation, which is performed to obtain the intrinsic states of the projection calculations, there are these three types of the triaxial deformation related to the cranking axis. In this section, we show the results of projection calculations for four typical cases of the triaxial deformations; we choose $\gamma = 0°$, $30°$, $-30°$ and $-90°$ as the deformation parameters of the intrinsic states.

Fig. 5.8 shows the resultant spectra of the angular momentum projections for different γ values, $0°, 30°, -30°$ and $-90°$, respectively. In the case of $\gamma = 0°$, which

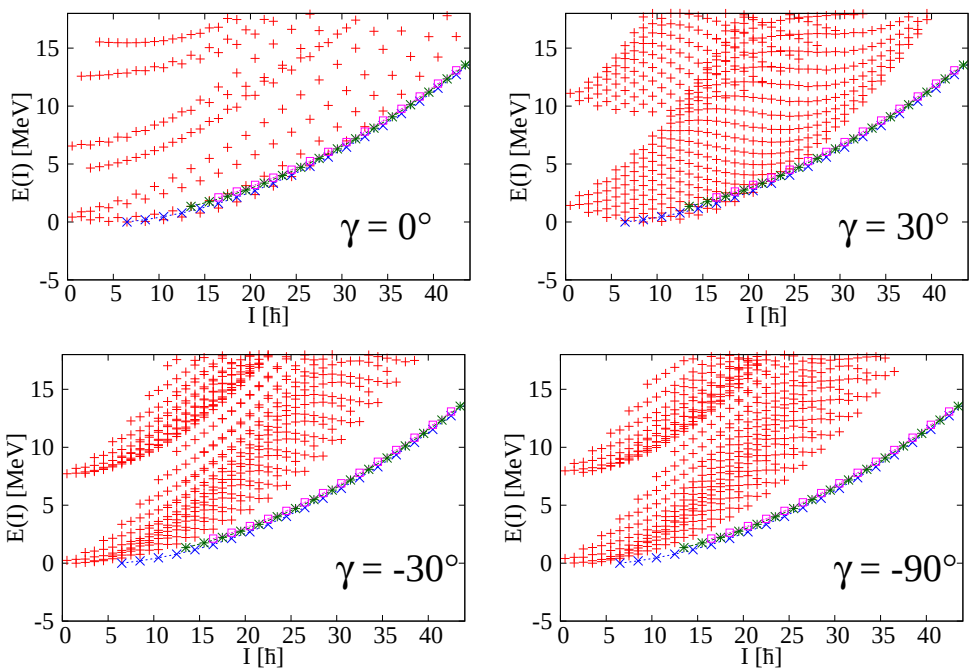

Figure 5.8: Energy spectrum for $\gamma = 0°, 30°, -30°$ and $-90°$. Excitation energies by the angular momentum projection calculation for the nucleus ^{163}Lu are plotted as a function of spin I. In the experimental data, yrast, 1-phonon excitation and 2-phonon excitation bands are labeled by "TSD1", "TSD2" and "TSD3", respectively.

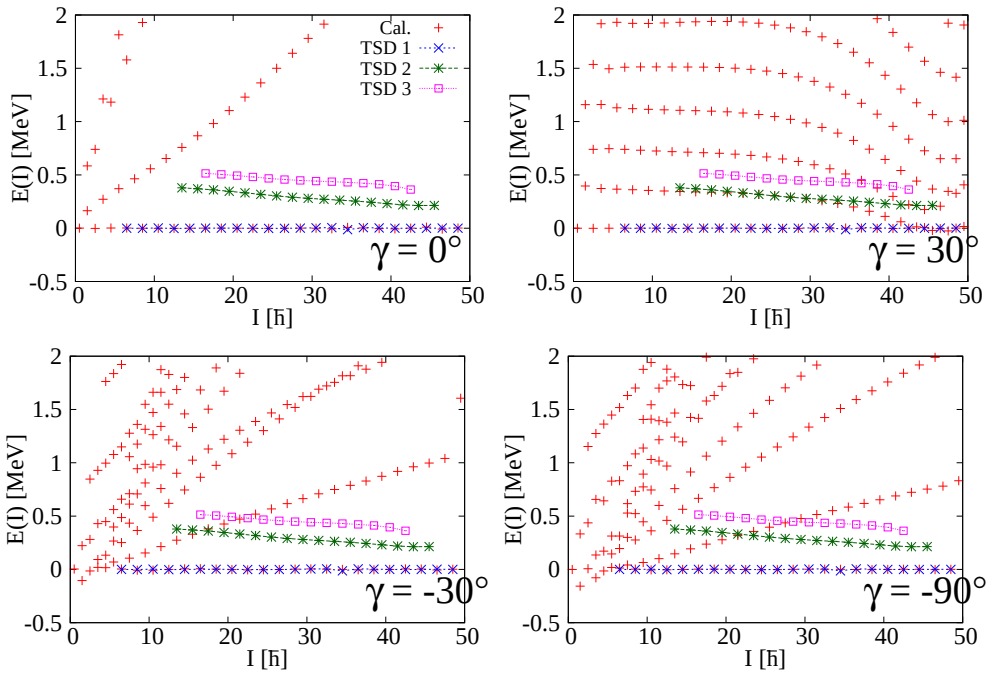

Figure 5.9: Excitation energies for $\gamma = 0°, 30°, -30°$ and $-90°$. Excitation energies from the yrast line by the angular momentum projection calculation ("Cal.") for the nucleus ^{163}Lu are plotted as functions of spin I in comparison with the experimental data [54].

corresponds to axially symmetric deformation, the band structure is a relatively simple and no phonon-like multiple band structure appears. In contrast, in the cases of finite γ values, the multiple band structures appear. The excitation energies from the yrast line are shown in Fig. 5.9. It is apparent that the phonon-like multiple band structure appears only in triaxially deformed cases. The calculated phonon excitation energies decrease as a function of spin for $\gamma = 30°$, while they increase for $\gamma = -30°$ or $-90°$. The former trend, namely the decreasing excitation energy, corresponds to the transverse wobbler. Our calculation suggests that this transverse wobbler appears for positive shape. On the other hand, the behaviors of the results of $\gamma = -30°$ or $-90°$, where excitation energy increases, are those of the longitudinal wobbler.

The in-band $E2$ transition probabilities of yrast (TSD1) and 1-phonon excitation (TSD2) bands are shown in Fig. 5.10. All the calculated $B(E2)$ both of TSD1 and TSD2 bands are almost constant as a function of the spin I. Comparing with the in-band $B(E2)$ for the $\gamma = 18°$ in Fig. 5.5, the effect of the increase of γ deformation as a function of spin I would explain the observed decrease of in-band $B(E2)$ values. Such an effect can be included by the projected configuration mixing calculation of deformations.

The ratios $B(E2)_{\rm OUT}/B(E2)_{\rm IN}$ are shown in Fig. 5.11. In the case of $\gamma = 0°$, all the out-of-band $E2$ transition probabilities are very small value, which indicates that for the axially symmetric deformed nuclei there are no wobbling bands. The strong

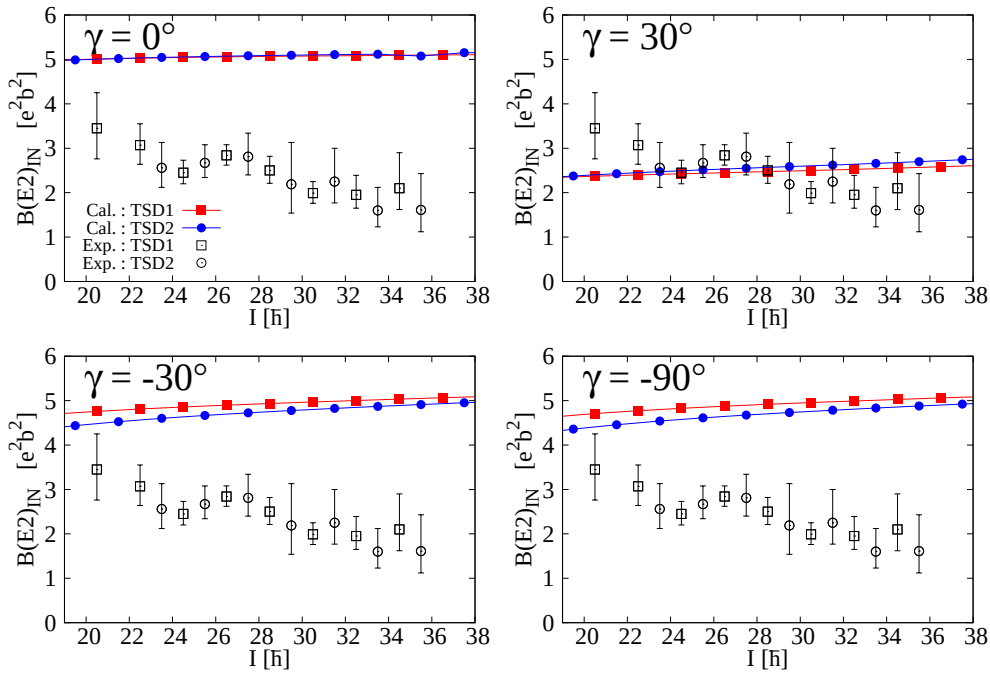

Figure 5.10: In-band $B(E2)$ for $\gamma = 0°, 30°, -30°$ and $-90°$. The in-band $E2$ transition probabilities both of TSD1 and TSD2 band for ^{163} Lu are plotted as functions of spin I. The experimental data is taken from Ref. [55].

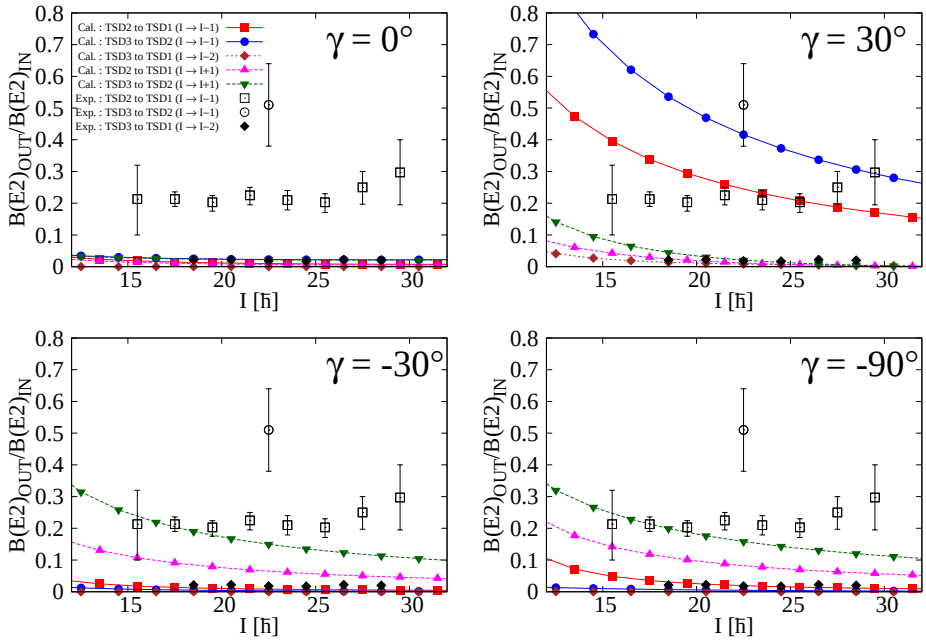

Figure 5.11: Ratios of the out-of-band $B(E2)$ to in-band $B(E2)$ for $\gamma = 0°, 30°, -30°$ and $-90°$. The $\Delta n = 1$ and 2 $E2$ transition probabilities are plotted as a function of the spin I. For the $\Delta n = 1$ transitions, the $I \to I - 1$ $(I + 1)$ $E2$ transition probabilities are represented by the solid (dashed) lines. The experimental data is taken from Ref. [54], where only the $I \to I - 1$ transition probabilities are measured.

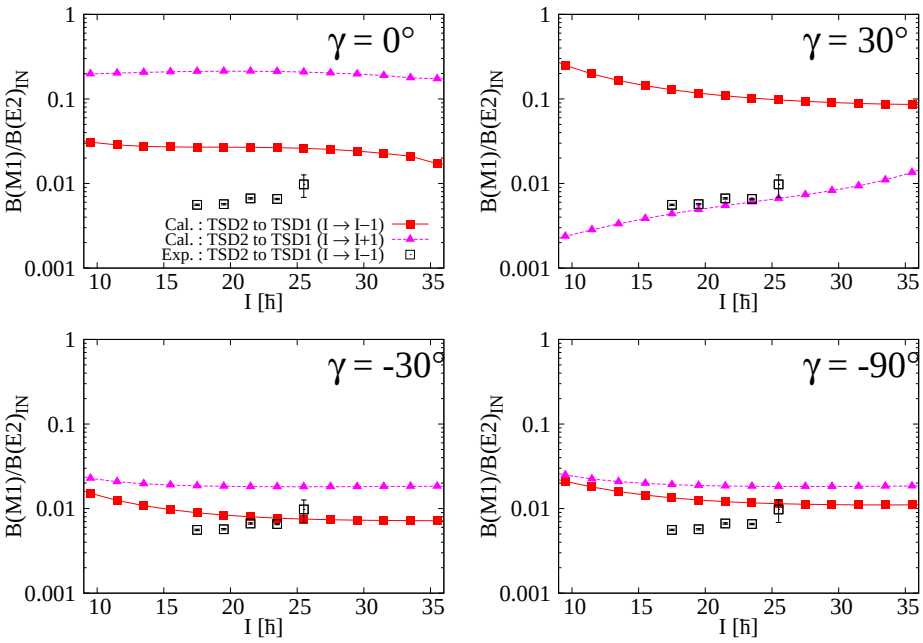

Figure 5.12: Ratios of the out-of-band $B(M1)$ to in-band $B(E2)$ for $\gamma = 0°, 30°, -30°$ and $-90°$. Calculated $I \to I-1$ $(I+1)$ $B(M1)$ are represented by the solid (dashed) lines. The experimental data is taken from Ref. [56], where only the $I \to I-1$ transition probabilities are measured.

out-of-band $E2$ transitions are seen only in triaxially deformed cases. The $I \to I-1$ $B(E2)$ values are larger than the $I \to I+1$ $B(E2)$ values for $\gamma = 30°$, while The $I \to I-1$ $B(E2)$ values are smaller than the $I \to I+1$ $B(E2)$ values for $\gamma = -30°$ or $-90°$. The behavior of the positive γ case agrees with the trend of the experimental data. The ratios $B(E2)_{\rm OUT}/B(E2)_{\rm IN}$ for the $\gamma = 30°$ decrease as a function of spin, and are larger than the values for the $\gamma = 18°$ (see, Fig. 5.6). On the other hand, the experimental data is almost constant as a function of spin. This also indicates that in the wobbling band for the ^{163}Lu, the increase of the triaxial deformation may occur, and to obtain the more quantitative agreement with the experimental data, the configuration mixing of the triaxial deformation may be necessary. The ratios $B(M1)_{\rm OUT}/B(E2)_{\rm IN}$ are shown in Fig. 5.12. In the case of $\gamma = -30°$ and $-90°$, the $I \to I+1$ $B(M1)$ are almost as much as the $I \to I-1$ values, which is not consistent the trend of experimental data. On the other hand, in the case of $\gamma = 30°$, $I \to I-1$ $B(M1)$ are much larger than the $I \to I+1$ values. Comparing with the result for $\gamma = 18°$ in Fig. 5.7, the γ-dependence of $B(M1)$ is not so large.

Thus the mechanism of occurrence of the wobbling motion in the odd nucleus seems to be confirmed by our fully microscopic calculation. For the wobbling band, the presence of the triaxial deformation is crucial. In the axially symmetric deformed nuclei, the wobbling motion does not occur. For the behavior of the excitation energies from the yrast line, the sign of the triaxial deformation parameter γ can be determined, and in order to obtain the transverse wobbler in nucleus ^{163}Lu positive

values are found to be necessary. Also both for the $B(E2)$ and $B(M1)$ values, the positive-γ shape is necessary to reproduce the trend of the experimental data.

5.5.4 Results with the Gogny effective interaction

We also perform the angular momentum projection calculation employing the Gogny-D1S effective interaction. We use the oscillator basis with $N_{\rm osc}^{\rm max} = 12$. The triaxially deformed minimum for ^{163}Lu is found by the HFB calculation. The deformation parameters are $\beta_2 = 0.442$ for the quadrupole deformation and $\gamma = 11.2^\circ$ for the triaxially deformed shape. The calculated pairing gap for the neutrons is $\Delta = 0.677$ MeV, and the proton pairing gap vanishes. The cranking frequency is chosen to be $\hbar\boldsymbol{\omega}_{\rm rot} = (0.2, 0, 0)$ MeV. In the previous section, we used $\gamma = 18^\circ$ for the Woods-Saxon potential, and it is obtained by the Nilsson-Strutinsky calculation. The triaxial deformation parameter obtained by the HFB calculation with the Gogny interaction seems to be smaller than that of the Nilsson-Strutinsky calculation. This is mainly due to the difference of the definition for the deformation parameters. The deformation parameter $\gamma = 18^\circ$ of the Woods-Saxon calculation is defined from the shape of the average potential, see Eq. (5.13), while the one here from the density distribution, see Eq. (5.20), i.e. $\gamma = \tan^{-1}(\sqrt{2}\langle\hat{Q}_{22}\rangle/\langle\hat{Q}_{20}\rangle)$. The triaxially deformed shape with $\gamma = 11.2^\circ$ in our calculation nicely agrees with that of the Nilsson-Strutinsky calculation, see Ref. [57]. The value of the norm cut-off is chosen to be 10^{-8}.

The resultant energy spectrum of the angular momentum projection calculation is shown in Fig. 5.13. It is found that the multiple band structure also appears by the projection calculation with the Gogny interaction. Fig. 5.14 shows the excitation energies from the yrast line. The phonon-like multiple band structure can be clearly seen although the calculated excitation energies overestimate the experimental data. In order to obtain more reliable excitation energies, it is necessary to consider the small cranking around the z-axis in the same way as the previous case of the Woods-Saxon potential and the schematic interaction. This small cranking reduces the phonon excitation energies. It is also found that the calculated excitation energies decrease as functions of spin, which corresponds to the behavior of the experimental data. The occurrence of the nuclear wobbling motion for odd nucleus ^{163}Lu is also confirmed in the calculation with the Gogny effective interaction although the agreement with the experimental data is not satisfactory.

5.6 Chiral doublet band

5.6.1 Introduction

The chiral doublet band is predicted to appear in the triaxially deformed odd-odd nuclei with a high-j particle and a high-j hole. The angular-momentum vector of the particle (hole) tends to align along the short (long) axis to maximize the overlap

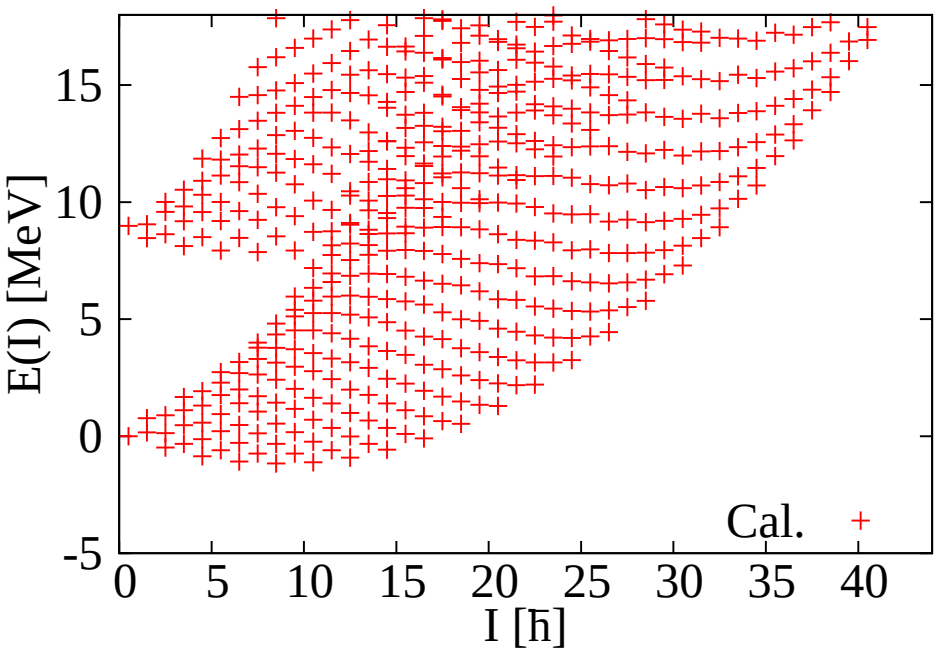

Figure 5.13: Energy spectrum with the Gogny-D1S effective interaction. Excitation energies by the angular momentum projection calculation for the nucleus ^{163}Lu are plotted as a function of spin I. In the experimental data, yrast, 1-phonon excitation and 2-phonon excitation bands are labeled by "TSD1", "TSD2" and "TSD3", respectively.

of density distributions between the particle (hole) and core. When the nucleus is considered as a body with irrotational flow, the angular-momentum vector of the core aligns along the intermediate axis since it has the largest moment of inertia. Thus, three angular-momentum vectors, those of the core, the high-j particle and the high-j hole, align along the three mutually perpendicular directions. These three angular momentum vectors give rise to a right-handed $|r\rangle$ or left-handed $|l\rangle$ chiral geometry (see, Fig. 5.15), which are interchanged by the combination of the time-reversal operation, $\mathcal{T}$, and the rotation by an angle of π, $R(\pi)$,

$$|l\rangle = \mathcal{T}R(\pi)|l\rangle. \tag{5.31}$$

In the laboratory frame, it is necessary to restore the chiral symmetry broken in the intrinsic frame. This chiral geometry leads to two degenerate states given by

$$|+\rangle = \frac{1}{\sqrt{2}}(|r\rangle + |l\rangle) \tag{5.32}$$

$$|-\rangle = \frac{1}{\sqrt{2}}(|r\rangle - |l\rangle). \tag{5.33}$$

At low spin, the angular-momentum vector of the core aligns along the total angular-momentum vector of the particle and hole due to the cranking term $-\boldsymbol{\omega}_{\rm rot}\cdot\boldsymbol{J}$. This breaks the symmetry of the rotation around the main axis of the ellipsoid by

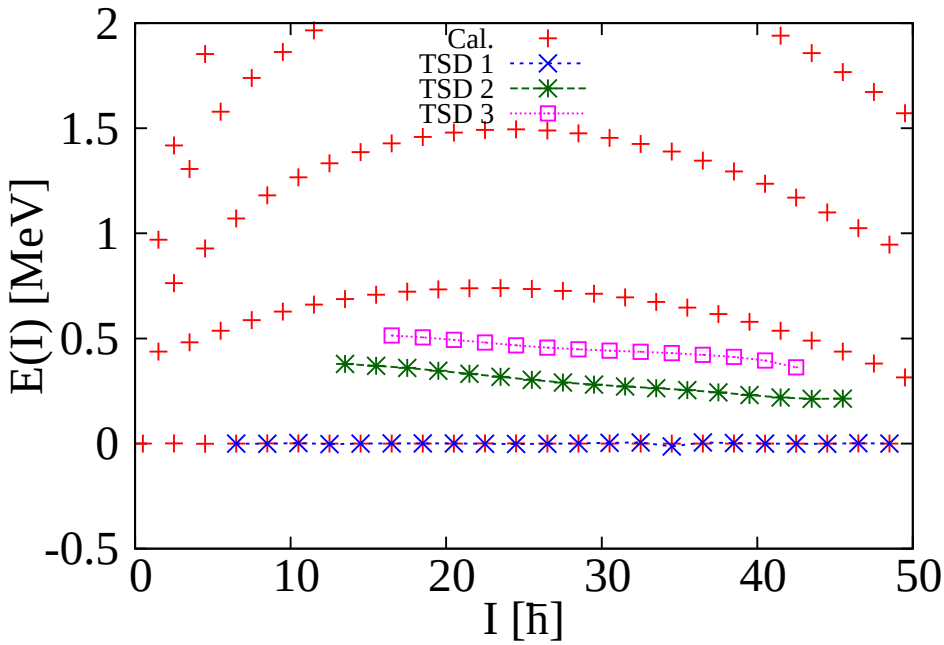

Figure 5.14: Excitation energies with the Gogny-D1S effective interaction. Excitation energies from the yrast line calculated by the angular momentum projection ("Cal.") for the nucleus ^{163}Lu are plotted as a function of spin I in comparison with the experimental data [54]. In the experimental data, yrast, 1-phonon excitation and 2-phonon excitation bands are labeled by "TSD1", "TSD2" and "TSD3", respectively.

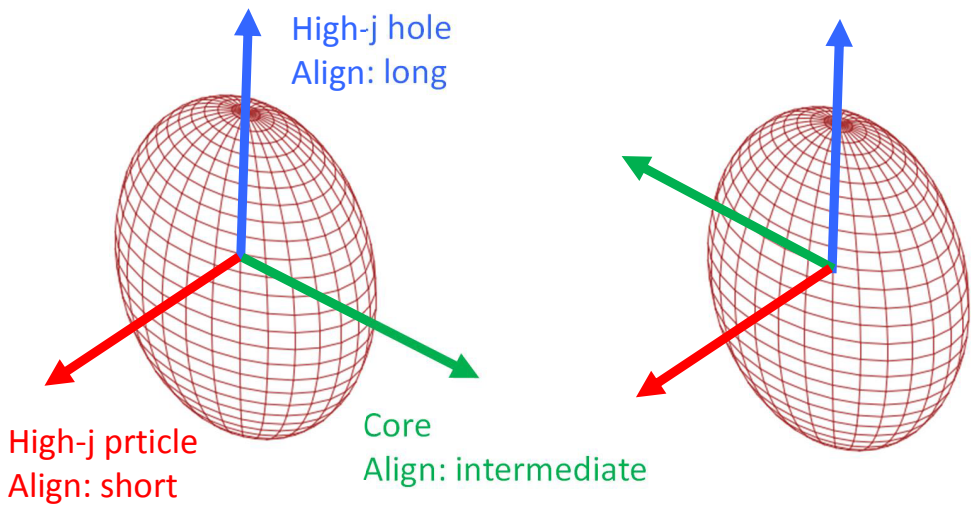

Figure 5.15: Schematic picture of the chiral geometry. The angular-momentum vectors of the core, high-j particle and high-j hole align along the intermediate, long and short axis of the triaxial ellipsoid, respectively. These three angular momentum vectors give rise to a right-handed or a left-handed chiral geometry.

the angle of π, which produces the degeneracy of two $\Delta I = 2$ bands and the $\Delta I = 1$ band is obtained. At high spin, it is favorable that the angular-momentum vector of the core aligns along the axis with the largest moment of inertia. Therefore, with

increasing the spin the angular-momentum vector of the core moves from the plane formed by the short and long axis to the intermediate axis, which produces the chiral geometry. As a result, at high spin the degenerate pair of $\Delta I = 1$ bands are obtained.

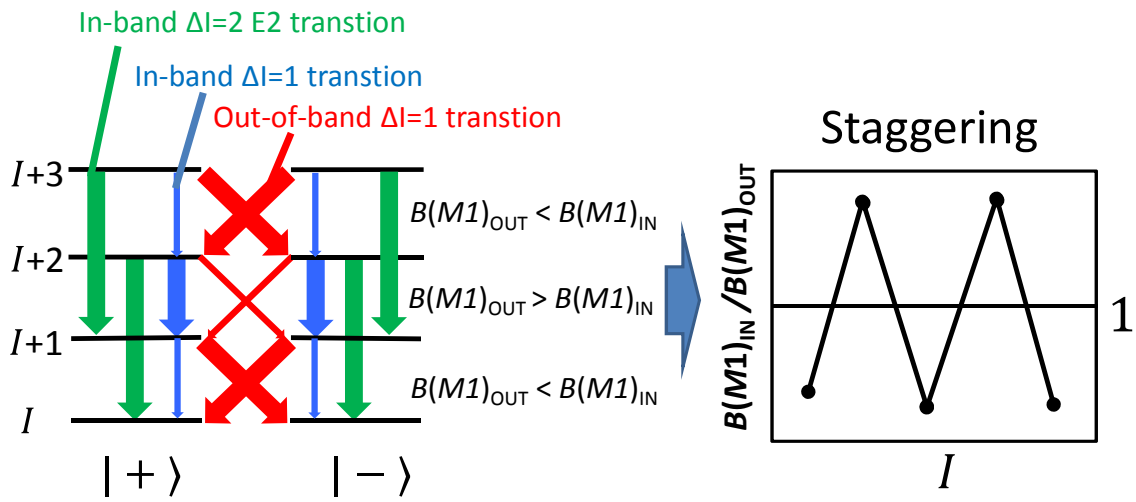

Figure 5.16: Selection rules for electromagnetic transitions in the chiral doublet band studied by the particle-rotor model [58], and the staggering of the ratios $B(M1)_{\rm OUT}/B(M1)_{\rm IN}$. The thick arrows represent the $\Delta I = 1$ and 2 $E2$ transitions and stronger $\Delta I = 1$ $M1$ transitions. The thin arrows represent the weaker $\Delta I = 1$ $M1$ transitions. By these selection rules, the characteristic staggering of the ratios $B(M1)_{\rm OUT}/B(M1)_{\rm IN}$ appears for the chiral doublet band.

One of the most striking features of the chiral doublet band is the pattern of M1-transitions, which was discussed by Koike et al. by using the macroscopic particle-hole-rotor coupling model [58]. The selection rule of the electromagnetic transitions for the chiral doublet bands are shown in Fig 5.16. While the out-of-band $E2$ transitions suppressed, the out-of-band $M1$ transitions are allowed. The strong in-band and out-of-band $M1$ transitions appear alternately as functions of spin. This characteristic feature can be most clearly seen in the ratio of $B(M1)_{\rm IN}$ over $B(M1)_{\rm OUT}$, which produce the staggering of the ratios. In the ideal case, where the weak transitions are prohibited, this ratio takes the values of zero and infinity alternately.

The approximate degeneracy of two bands have been observed experimentally for nuclei in several regions in the nuclear chart. The chiral doublet bands are investigated and identified in odd-odd and odd-mass nuclei in $A \sim 100$ and 130 regions [11, 12, 13]. For odd-odd nuclei in $A \sim 100$ region, an odd-proton occupies a qusiparticle state coming from the hole-like $g_{9/2}$ orbit and an odd-neutron occupies a qusiparticle state coming from the particle-like $h_{11/2}$ orbit. On the other hand, in $A \sim 130$ region, an odd-proton and an odd-neutron occupy $h_{11/2}$ particle-like and hole-like quasiparticle orbits, respectively. In this thesis, we investigate the chiral doublet band for the odd-odd nuclei ^{104}Rh and ^{128}Cs by applying the angular momentum projection method.

5.6.2 Results for ^{128}Cs

The parameters of the mean-field Hamiltonian are chosen to be the following values: The deformation parameters (β_2, γ) are searched to find the degenerate bands. We found them for $\beta_2 = 0.3$ and $\gamma = -30°$ in ^{128}Cs. The hexadecapole deformation parameter β_4 is chosen to be zero. The mean pairing gaps are $\Delta_n = 0.85$ and $\Delta_p = 1.07$ MeV, which are calculated selfconsistently from the monopole pairing strength g_0. As mentioned in Sec. 5.2, g_0 is taken to be a average value of the strengths for the two neighboring even-even nuclei. For this calculation of the chiral doublet band, no cranking is performed.

The energy spectra are shown in Fig. 5.17. For a lot of bands, the degenerations of even-I (solid lines) and odd-I (dashed lines) band are seen, which produce the $\Delta I = 1$ bands, since the symmetry of the rotation around the main axis of the ellipsoid by the angle of π are broken. This condition is important for the appearance of the chiral doublet band. At low spin, two lowest bands are clearly separated, but with increasing the spin they are getting close to each other. The degeneration of lowest two bands can be seen around $I = 17\hbar$. The calculated lowest two bands in comparison with the experimental are shown in Fig. 5.18. In our calculation, the degeneration of lowest two bands appears at higher spin compared with the experimental data. The calculated energy difference of two bands around $I = 17\hbar$ are about 200 keV, and decrease

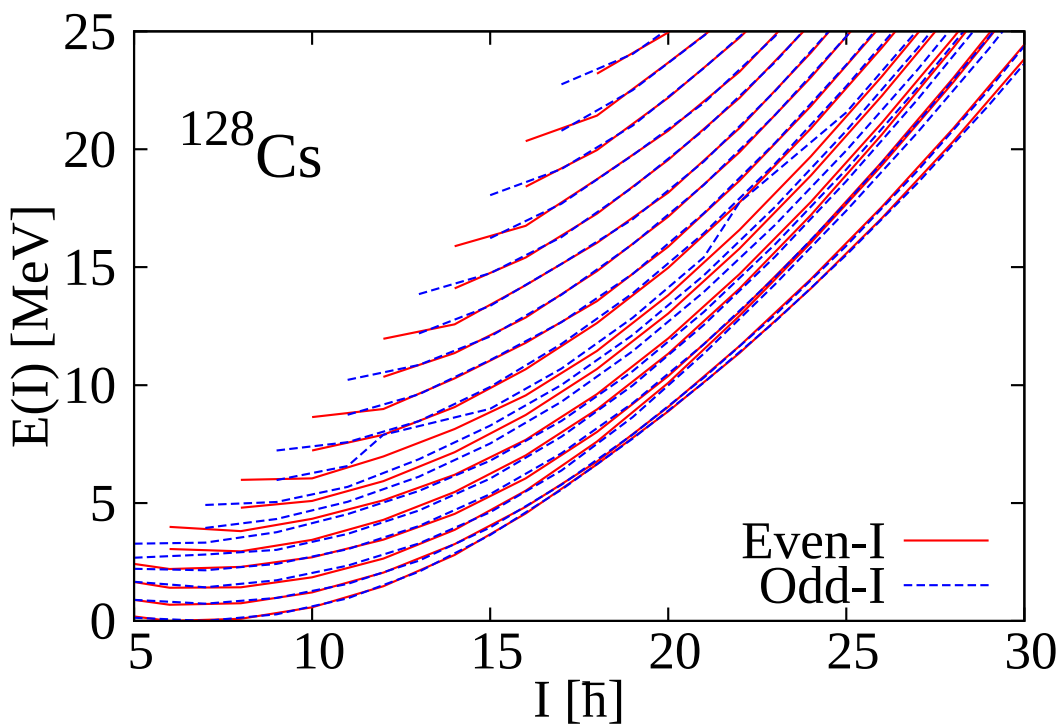

Figure 5.17: Energy spectrum for ^{128}Cs. Excitation energies by the angular momentum projection calculation are plotted as functions of spin I. The solid (dashed) lines represent the even-I (odd-I) excitation energies.

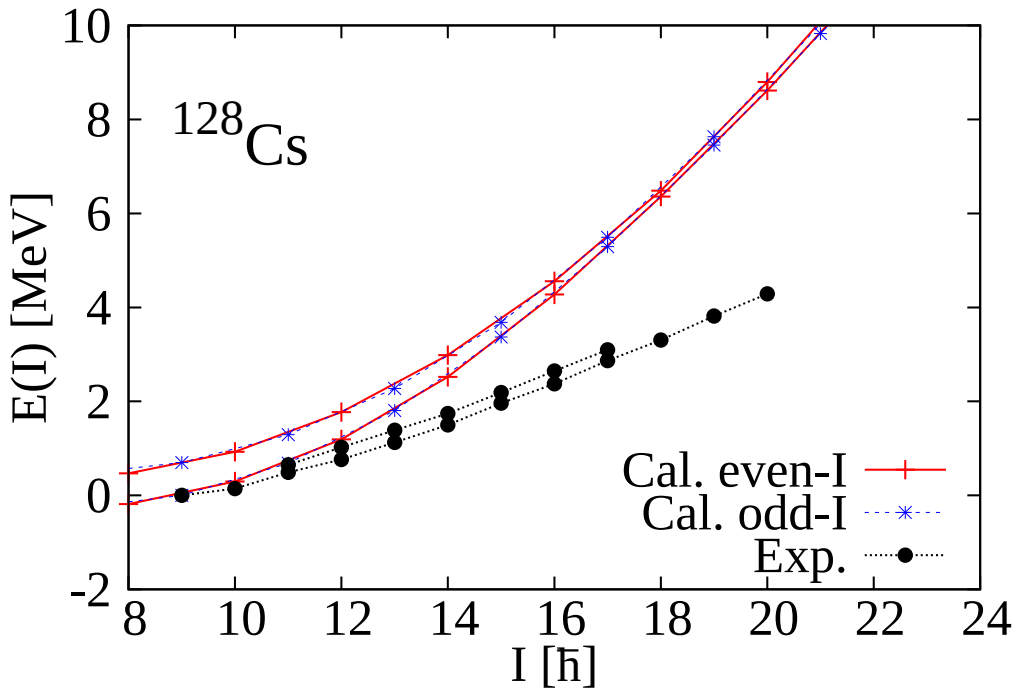

Figure 5.18: Lowest two $\Delta I = 1$ bands for ^{128}Cs. Calculated excitation energies are plotted as a function of spin I in comparison with the experimental data [12]. Each bands are shifted to so that $E(9^+) = 0$ MeV. The solid (dashed) lines represent the even-I (odd-I) excitation energies in the calculated band.

with increasing the spin. On the other hand, the experimental energy differences of two bands are about $\Delta E = 250$keV, and are almost constant as a function of spin. Although the calculated moment of inertias, which corresponds to the slope of the excitation energies, are smaller than the experimental value, the degenerated pair of $\Delta I = 1$ bands appear in our fully microscopic calculation.

The pattern of the $M1$ transition probabilities is the key to identify the chiral doublet band. The calculated ratios of $B(M1)_{\rm IN}$ over $B(M1)_{\rm OUT}$ are shown in Fig. 5.19. At low spin, the in-band $B(M1)$ are larger than the out-of-band $B(M1)$ by about factor 4. However, the staggering of the ratios $B(M1)_{\rm IN}/B(M1)_{\rm OUT}$ can be seen in $I \geq 17\hbar$. This ratio oscillates between the smaller and larger values than one alternately as a function of spin. The calculated values seem to well correspond to the experimental data in Fig. 16 of Ref. [12]. Fig. 5.20 shows the ratios $B(M1)/B(E2)$ for the yrast and side bands. The similar behavior is obtained in the ratios both of the yrast and side bands. The staggering of the in-band $M1$ transition probabilities appear in $I \geq 17\hbar$. The characteristic pattern of in-band and out-of-band $M1$ transition probabilities, which is one of most striking features for the chiral doublet band, appears in our microscopic calculation.

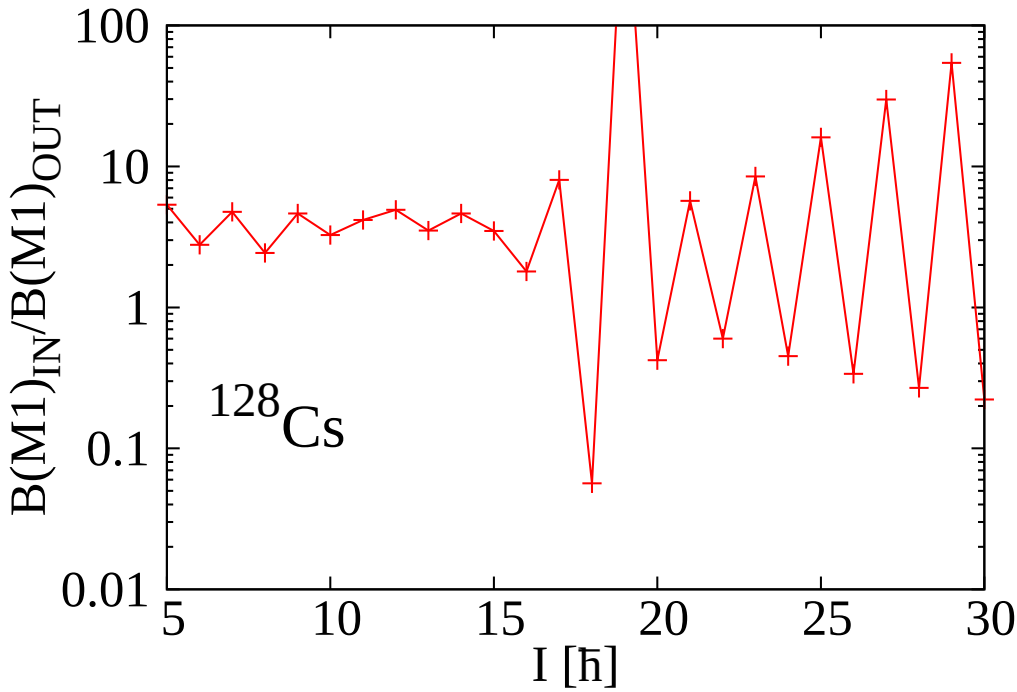

Figure 5.19: The ratio $B(M1)_{\mathrm{IN}}/B(M1)_{\mathrm{OUT}}$ for ^{128}Cs. For the out-of-band $M1$ transitions, only the transition probabilities from the side band to the yrast band are plotted.

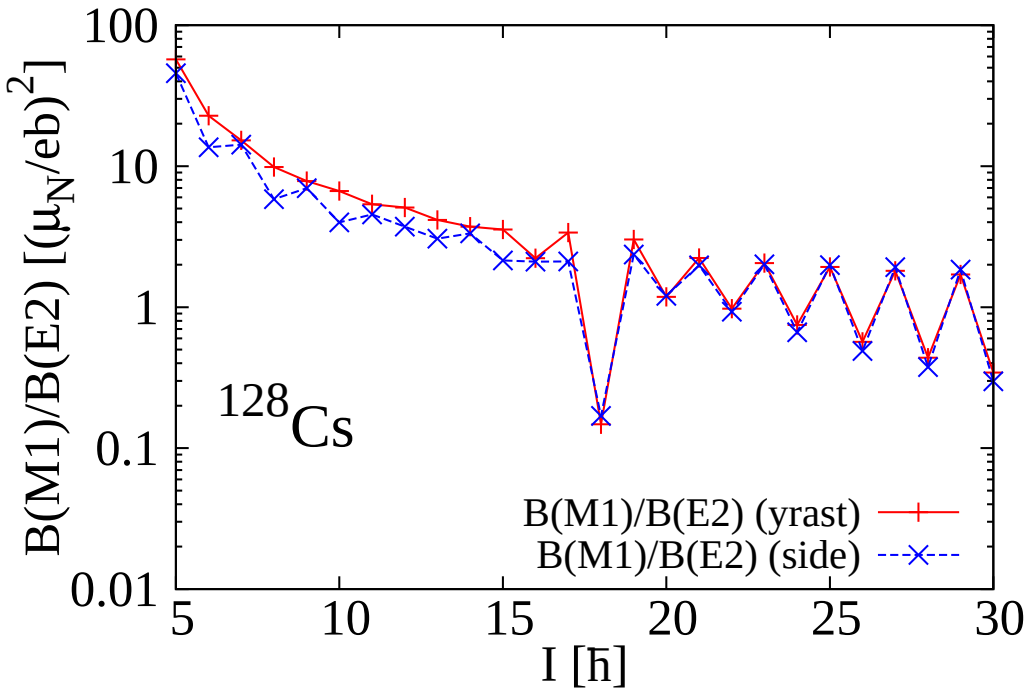

Figure 5.20: The ratios $B(M1)/B(E2)$ for ^{128}Cs. The ratios $B(M1)/B(E2)$ both for the yrast (solid line) and side (dashed line) bands are plotted as a function of spin.

5.6.3 Results for ^{104}Rh

As in the case for ^{128}Cs, the parameters of the mean-field Hamiltonian are chosen to be the followings: The deformation parameters (β_2, γ) are searched to find the degenerate bands. We found them for $\beta_2 = 0.25$ and $\gamma = -30°$ in ^{104}Rh. The hexadecapole deformation parameter β_4 is chosen to be zero. The mean pairing gaps are $\Delta_n = 0.95$ and $\Delta_p = 0.76$ MeV, which are calculated selfconsistently from the monopole pairing strength g_0. As mentioned in Sec. 5.2, g_0 is taken to be an average value of the strengths for the two neighboring even-even nuclei. For this calculation of the chiral doublet band, no cranking is performed.

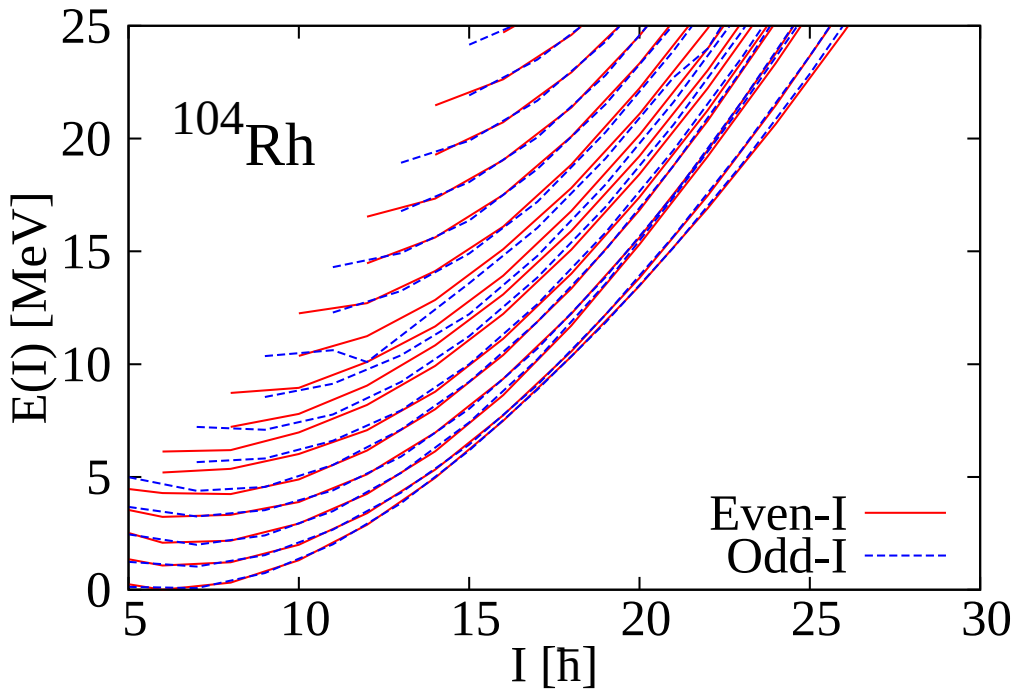

Figure 5.21: Energy spectrum for ^{104}Rh. Excitation energies by the angular momentum projection calculation are plotted as functions of spin I. The solid (dashed) lines represent the even-I (odd-I) excitation energies.

The energy spectra are shown in Fig. 5.21. The degenerations of even-I (solid lines) and odd-I (dashed lines) band can be observed, which produce the $\Delta I = 1$ bands as in the same way as ^{128}Cs. At low spin, two lowest $\Delta I = 1$ bands are clearly separated. The degeneration of lowest two bands can be observed around $I = 16\hbar$. The calculated lowest two bands in comparison with the experimental are shown in Fig. 5.22. In our calculation, the degeneration of lowest two bands appears at higher spin compared with the experimental data. The calculated energy difference of two bands decreases with increasing the spin, which agrees with the experimental behavior. Also for the nucleus ^{104}Rh, the degenerated pair of $\Delta I = 1$ bands, the chiral doublet band, appears in our microscopic calculation.

The calculated ratios of $B(M1)_{\rm IN}$ over $B(M1)_{\rm OUT}$ are shown in Fig. 5.23. The characteristic staggering of the ratios $B(M1)_{\rm IN}/B(M1)_{\rm OUT}$ can be seen in $I \geq 16\hbar$.

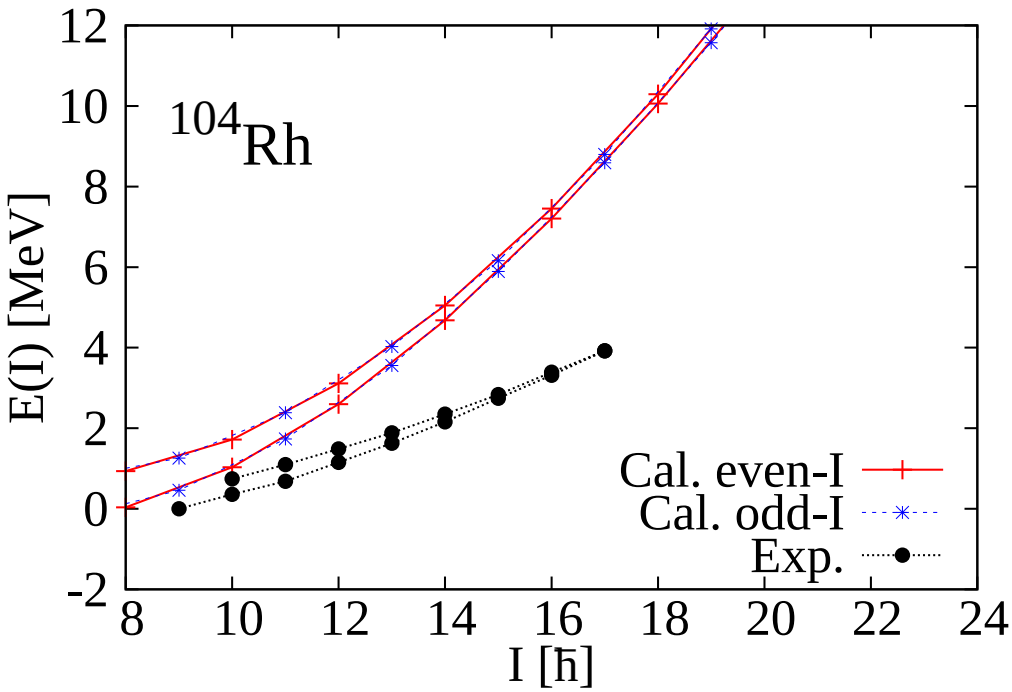

Figure 5.22: Lowest two $\Delta I = 1$ bands for ^{104}Rh. Calculated excitation energies are plotted as a function of spin I in comparison with the experimental data [13]. Each bands are shifted to so that $E(9^+) = 0$ MeV. The solid (dashed) lines represent the even-I (odd-I) excitation energies in the calculated bands.

This ratio oscillates between the smaller and larger values than one alternately as a function of spin. Fig. 5.24 shows the ratios $B(M1)/B(E2)$ for the yrast and side band. The staggering of the in-band $M1$ transition probabilities appear in $I \geq 16\hbar$. The characteristic pattern of in-band and out-of-band $M1$ transition probabilities appears in our microscopic calculation. Thus, for ^{104}Rh, the similar results to ^{128}Cs are obtained; the staggering behavior is even more enhanced in ^{104}Rh. Therefore, the chiral doublet band is not specific only for the nucleus ^{128}Cs, but is characteristic for the odd-odd triaxially deformed nuclei with a high-j particle and a high-j hole.

5.7 Short summary

In this chapter we have studied the high-spin states of triaxially deformed nuclei by using the fully microscopic framework, the angular momentum projection method. As interesting examples, we have applied the method to the wobbling band and the chiral doublet band. In this calculation, as for the Hamiltonian we employ the Woods-Saxon potential and the schematic separable-type residual interaction.

As for the wobbling band, the phonon-like multiple band structure is obtained in the triaxially deformed nuclei. In the axially symmetric deformed nuclei, the wobbling band does not appear. For the excitation energies, in the case of the positive-γ value, the "transverse" wobbler is obtained. On the other hand, in the case of the negative-γ

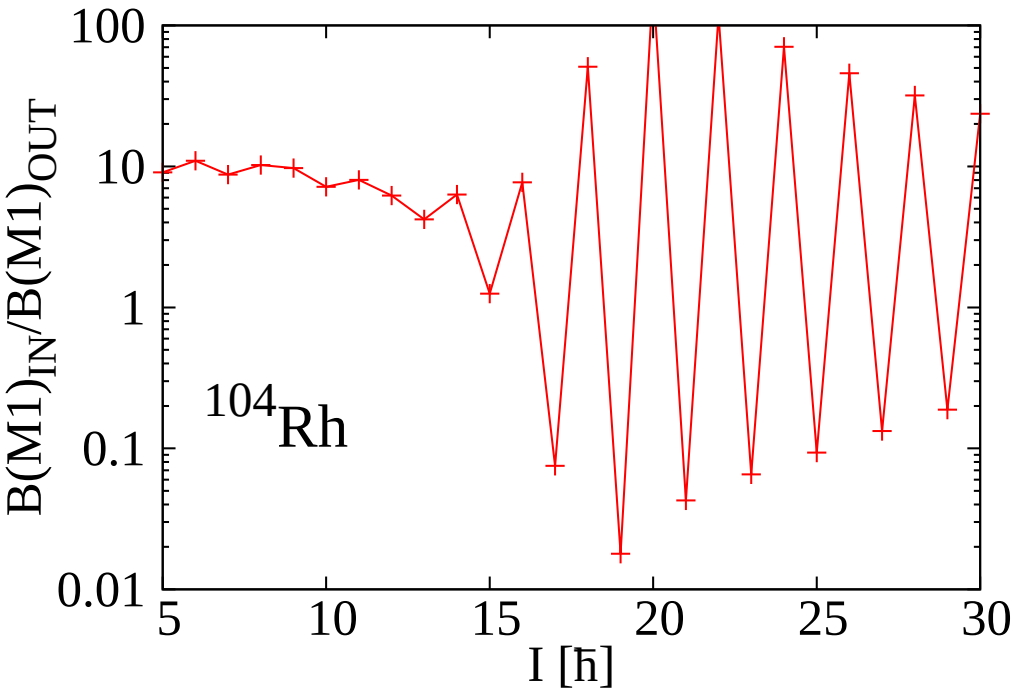

Figure 5.23: The ratio $B(M1)_{\mathrm{IN}}/B(M1)_{\mathrm{OUT}}$ for ^{104}Rh. For the out-of-band $M1$ transitions, only the transition probabilities from the side band to the yrast band are plotted.

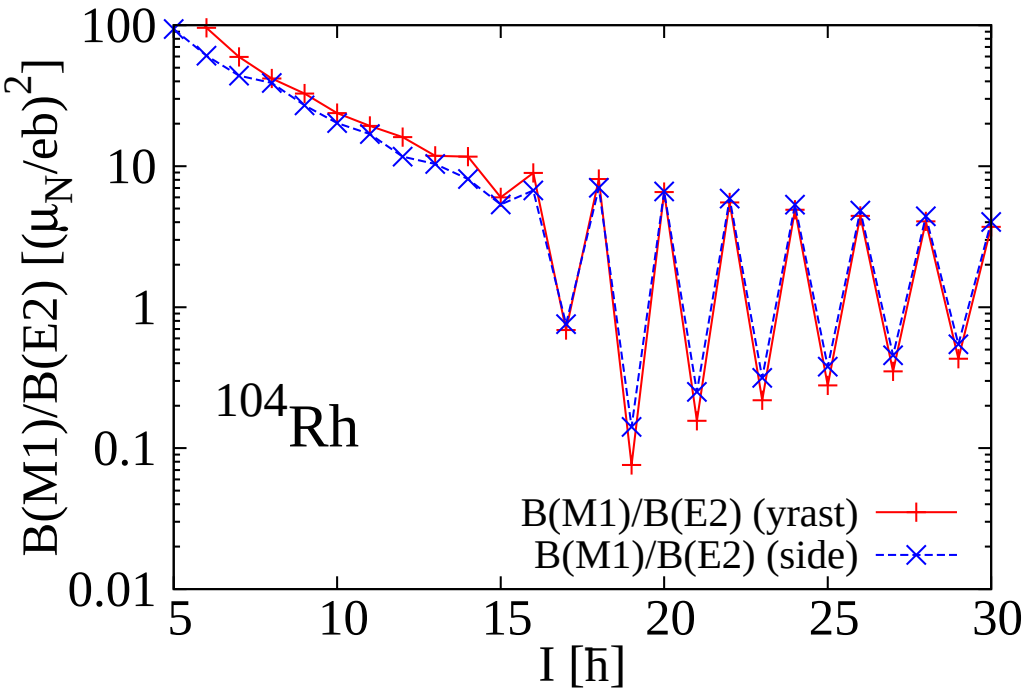

Figure 5.24: The ratios $B(M1)/B(E2)$ for ^{104}Rh. The ratios $B(M1)/B(E2)$ both for the yrast (solid line) and side (dashed line) bands are plotted as a function of spin.

value, the "longitudinal" wobbler appears as it is predicted in Ref. [53]. In order to explain the experimental trend in odd nucleus ^{163}Lu, positive-γ shape is found to be necessary. The calculated out-of-band $B(E2)$ well follows the phonon-like properties. Also from the properties of the transition probabilities, our calculation suggests the positive-γ shape. The occurrence of the nuclear wobbling motion is confirmed by our fully microscopic calculation, although the experimental data are not very well reproduced.

As for the chiral doublet band, we have confirmed that the degenerate bands can be obtained in ^{128}Cs and ^{104}Rh by properly choosing the deformation parameters, although they appear at higher spin comparing with the experimental data. At low spin, the lowest two $\Delta I = 1$ bands are clearly separated, but at high spin the degeneration of them occurs. For the nucleus ^{128}Cs, this degeneration appears around $I = 17$, and for the nucleus ^{104}Rh it appears around $I = 16$. The staggering of the ratios $B(M1)_{\rm IN}/B(M1)_{\rm OUT}$ is obtained in the spin region where the degenerate pair of $\Delta I = 1$ bands exists, which is a key to identify the chiral doublet band. The appearance of the chiral doublet band for the odd-odd nuclei is also confirmed by the angular momentum projection method.

We stress that our fully microscopic results come out very naturally without no fine tuning, although the agreement with the experimental data are not satisfactory. In order to obtain more reliable results, the calculations with the configuration mixing of deformation parameters and the multi-cranked configuration mixing may be necessary. Thus it is clear that the angular momentum projection method is a very useful and powerful tool to study the high-spin states from the microscopic viewpoint.

Chapter 6

Summary

The study of nuclear collective motion is one of the interesting topics in nuclear physics. At high-spin states, various rotational motions are predicted by the macroscopic models, e.g., the rotor model, and their microscopic understanding is necessary. The angular momentum projection method is one of the microscopic approaches to the nuclear rotational motions. In this thesis, we have studied microscopically the various rotational bands by the angular momentum projection method.

First, we have studied the low-spin states of the even-even Mg isotopes by the angular momentum projection method with the quadrupole configuration mixing employing the Gogny-D1S effective interaction. While in the mean-field calculation, the ground state of ^{32}Mg is predicted to have the spherical shape, the experimental data suggest the deformed ground state. On the other hand, in the projection calculation the deformed minimum is found. For the ^{30,32}Mg, the large changes of deformation parameters from the mean-field values have been found in our calculations. In order to obtain the correct deformation parameters, it is important to perform the angular momentum projection. The excitation energies $E(2^+)$ and $E(4^+)$, the ratios $E(4^+)/E(2^+)$, the rms radii and the $B(E2)$ transition probabilities have been investigated. Our calculated results have systematically well reproduced the experimental data although our calculations have no adjustable parameters. The effects of the quadrupole mixing and the time-odd components induced by the cranking procedure on these quantities have been investigated. Both the configuration mixing and time-odd components have the large influence on the excitation energies. For the ratios, it is important to include the configuration mixing. Both the configuration mixing and time-odd components have considerable effect on the $B(E2)$ values. On the other hand, both effect have the small influence on the rms radii. In order to reproduce the rms radii, it is necessary to obtain the correct deformation parameters, which have been obtained for the Mg isotopes by performing the angular momentum projection calculation.

Next, we have proposed a method to reliably calculate the rotational band by using the angular momentum projection technique. In this method, the rotational states are obtained by the superposition of the several states obtained by the projection

from several cranked states with different cranking frequencies. We call this method the "angular momentum projected multi-cranked configuration mixing", which can compromise the angular momentum projection method and the cranking model. We have applied to the ground state band of ^{164}Er, the ground state band of ^{40}Mg and the superdeformed band of ^{152}Dy. It has been shown that the resultant spectrum is essentially independent of the chosen set of the cranking frequencies, and the necessary number of these frequencies is rather small. While the moment of inertia calculated by the simple projection from one intrinsic state is constant (or decrease) as a function of spin, the inertia calculated by the multi-cranked configuration mixing increases as a function of spin, which is consistent with the experimental behavior. The crossing of the g-band and the s-band for ^{164}Er has been investigated. This crossing has been obtained by the multi-cranked configuration mixing calculation although the crossing occurs at higher spin compared with experimental data. The calculated inertia for the s-band overestimates the experimental value since the neutron pairing gap vanishes in our calculation. Systematic applications to the ground state band of nuclei in the rare-earth region have been done. Comparing with the result of the simple projection from one intrinsic state, the improvement of the inertia has been seen for all cases. For the rare-earth nuclei, the better agreements with the experimental data have been also obtained compared with the cranking inertia.

Finally we have studied the high-spin states of the triaxially deformed nuclei by the angular simple angular momentum projection method. As examples, the wobbling band and the chiral doublet band have been investigated. In this calculation, as for the Hamiltonian, the Woods-Saxon potential and the schematic separable-type residual interaction have been employed. As for the wobbling band, the phonon-like multiple band structure appears in the triaxially deformed nuclei in our fully microscopic calculation although the agreement with the experimental data is not satisfactory. The calculated out-of-band $B(E2)$ values well follows the phonon-like properties. It has been shown that for the odd nucleus ^{163}Lu, the positive-γ shape is necessary in order to explain the experimental data. As for the chiral doublet band, for the odd-odd nuclei ^{128}Cs and ^{104}Rh, the degenerate pairs of the $\Delta I = 1$ bands have been obtained in our microscopic calculation although it appear at higher spin compared with the experimental data. The characteristic pattern of $B(M1)$ transition probabilities for the chiral doublet band has been also confirmed. The appearance of the chiral doublet band has been confirmed by the angular momentum projection. To obtain more reliable results, the configuration mixing of the deformation parameters and multi-cranked configuration mixing may be necessary.

Acknowledgments

I am deeply grateful to the supervisor, Associate Prof. Yoshifumi R. Shimizu. He gives me a lot of valuable comments and insightful suggestions through many discussions. Without his guidance and persistent help this thesis would not have been possible.

I would like to express my deep appreciation to Prof. Masanobu Yahiro, Associate Professor Kazuyuki Ogata, and Assistant Prof. Takuma Matsumoto. I was able to obtain much important knowledge of nuclear physics through the seminars and discussions.

I would like to thank all the members in the Nuclear Theory Group in Kyushu University. I would particularly like to thank Shingo Tagami who gave me a lot of useful comments and helpful discussions on this thesis. He gives me much beneficial knowledge through many discussions. I also wish to express my appreciation to Yudai Fujioka. This work is helped by his Master thesis as a starting point of the study for the wobbling band and the chiral doublet band.

I am indebt to Prof. Kosuke Morita for helpful discussions on this doctoral dissertation.

I would also like to express my gratitude to Yuki Yamaji, Yuko Megumi, Saori Shigematsu, Hiromi Tsuchijima, Megumi Ieda, Noriko Taguchi, and Mayumi Takaki for their practical supports.

Finally, I thank my family for their continuous supports and encouragements.

Bibliography

[1] S. Tagami and Y. R. Shimizu, Prog. Theor. Phys. **127**, 79 (2012).

[2] S. Tagami, Y. R. Shimizu, and J. Dudek, J. Phys. G **42**, 015106 (2015).

[3] T.Motobayashi et al., Phys. Lett. B **346**, 9 (1995).

[4] B.V. Pritychenko et al., Phys. Lett. B **461**, 322 (1999).

[5] V. Chisté et al., Phys. Lett. B **514**, 233 (2001).

[6] Brookhaven database, http://www.nndc.bnl.gov.

[7] P. J. Twin et al., Phys. Rev. Lett. **57**, 811 (1986).

[8] B. Singh, R. Zywina, R. B. Firestone, Nuclear Data Sheets **97**, 241 (2002)

[9] A. Bohr and B. R. Mottelson, *Nuclear Structure*, Vol. II Benjamin, New York (1975).

[10] S. W. Ødegård et al., Phys. Rev. Lett. **86**, 5866 (2001).

[11] K. Starosta et al., Phys. Rev. Lett. **86**, 971 (2001).

[12] T. Koike et al., Phys. Rev. C **67**, 044319 (2003).

[13] C. Vaman et al., Phys. Rev. Lett. **92**, 032501 (2004).

[14] P. Ring and P. Schuck, *The Nuclear Many-Body Problem*, Springer, New York (1980).

[15] A. Staszczak, M.Stoitsov, A. Baran, and W. Nazarewicz, Eur. Phys. J. A **46**, 85 (2010).

[16] D. R. Inglis, Phys. Rev. **96**, 1059 (1954).

[17] B. Banerjee, H. J. Mang, and P. Ring, Nucl. Phys. A **215**, 366 (1973).

[18] R. Bengtsson and S. Frauendorf, Nucl. Phys. A **327**, 139 (1979).

[19] M. J. A. de Voigt, J. Dudek, and Z. Szymanski, Rev. Mod. Phys. **55**, 949 (1983).

[20] J. D. Garrett, G. B. Hagemann, and B. Herskind, Ann. Rev. Nucl. Part. Sci. **36**, 419 (1986).

[21] W. Satuła and R. A. Wyss, Rep. Prog. Phys. **68**, 131 (2005).

[22] T.H.R. Skyrme, Phil. Mag. 1, 1043 (1956).

[23] J. Dechargé and D. Gogny, Phys. Rev. C **21**, 1568 (1980).

[24] J. F. Berger, M. Girod, and D. Gogny, Comput. Phys. Commun. **63**, 365 (1991).

[25] P. Doornenbal et al., Phys. Rev. Lett. **111**, 212502 (2013).

[26] S. Watanabe et al., Phys. Rev. C **89**, 044610 (2014).

[27] S. Raman, C.W. Nestor, JR. and P. Tikkanen, At. Data Nucl. Data Tables **78**, 1 (2001).

[28] O. Niedermaier et al., Phys. Rev. Lett. **94**, 172501 (2005).

[29] H.Iwasaki et al., Phys. Lett. B **522**, 227 (2001).

[30] K. Hara and Y. Sun, Int. J. Mod. Phys. E **4**, 637 (1995).

[31] H. Zduńczuk, W. Satuła, J. Dobaczewski, and M. Kosmulski, Phys. Rev. C **76**, 044304 (2007).

[32] R. E. Peierls and D. J. Thouless, Nucl. Phys. **38**, 154 (1962).

[33] M. Anguiano, J. L. Egido, and L. M. Robledo, Nucl. Phys. A **683**, 227 (2001).

[34] M. Anguiano, J. L. Egido, and L. M. Robledo, Phys. Lett. B **545**, 62 (2002).

[35] M. Bender, K. Rutz, P.-G. Reihard, and J. A. Maruhn, Eur. Phys. J. A **8**, 59 (2000).

[36] S. W. Yates et al., Phys. Rev. C **21**, 2366 (1980).

[37] K. E. G. Löbner, M. Vetter, and V. Hönig, Nucl. Data Tables A **7**, 495 (1970).

[38] Balraj Singh, Nuclear Data Sheets **93**, 243 (2001).

[39] J. Terasaki, H. Flocard, P.-H. Heenen, and P. Bonche, Nucl. Phys. A **621**, 706 (1997).

[40] T. Lauritsen et al., Phys. Rev. Lett. **88**, 042501 (2002).

[41] W. Nazarewicz, R. Wyss, and A. Johnson, Nucl. Phys. A **503**, 285 (1989).

[42] Y. R. Shimizu, E. Vigezzi, and R. A. Broglia, Nucl. Phys. A **509**, 80 (1990).

[43] A. Bohr and B. R. Mottelson, Phys. Script. **24**, 71 (1981).

[44] M. J. Martin, Nuclear Data Sheets **114**, 1497 (2013).

[45] A. Johnson, H. Ryde, and S. Hjorth, Nucl. Phys. A **179**, 753 (1972).

[46] R. Wyss, private communication (2005).

[47] T. Shoji and Y. R. Shimizu, Prog. Theor. Phys. **121**, 319 (2009).

[48] S. Frauendorf, Nucl. Phys. A **557**, 259c (1993).

[49] S. Frauendorf, Nucl. Phys. A **677**, 115 (2000).

[50] S. Frauendorf, Rev. Mod. Phys. **73**, 463 (2001).

[51] G. B. Hagemann, Eur. Phys. J. A **20**, 183 (2004).

[52] Y. R. Shimizu and M. Matsuzaki, Nucl. Phys. A **588**, 559 (1995).

[53] S. Frauendorf and F. Dönau, Phys. Rev. C **89**, 014322 (2014).

[54] D. R. Jensen et al., Phys. Rev. Lett. **89**, 142503 (2002).

[55] A. Görgen et al., Phys. Rev. C **69**, 031301 (2004).

[56] I. Hamamoto et al., Acta Phys. Pol. B **32**, 2545 (2001).

[57] Y. R. Shimizu, T. Shoji and M. Matsuzaki, Phys. Rev. C **77**, 024319 (2008).

[58] I. Hamamoto et al., Phys. Rev. Lett. **93**, 172502 (2004).